DEVELOPMENT OF ULTRAFAST COHERENT ANTI-STOKES RAMAN SCATTERING (CARS) SPECTROSCOPY FOR HIGH PRESSURE SYSTEMS

by

Mingming Gu

A Dissertation

Submitted to the Faculty of Purdue University

In Partial Fulfillment of the Requirements for the degree of

Doctor of Philosophy

School of Mechanical Engineering

West Lafayette, Indiana

December 2020

THE PURDUE UNIVERSITY GRADUATE SCHOOL
STATEMENT OF COMMITTEE APPROVAL

Dr. Robert P. Lucht, Chair

School of Mechanical Engineering

Dr. Andrew Weiner

School of Electrical and Computer Engineering

Dr. Christopher S. Goldenstein

School of Mechanical Engineering

Dr. Carson Slabaugh

School of Aeronautics and Astronautics

Approved by:

Dr. Nicole L. Key

For my family.

ACKNOWLEDGMENTS

I would like to first acknowledge my major advisor, Dr. Robert P. Lucht, for offering me the precious opportunity in this exciting research field. He is always patient, friendly, and insightful. I am grateful that he has invested so many energies and resources in me, I am also appreciative of all the Thanksgiving dinners he has had me. After all, I feel fortunate to have had the chance to work with him during the past five years. Also, I want to thank my co-advisor, Dr. Christopher Goldenstein for showing me different aspects of laser spectroscopy, for inspiring me with his great enthusiasm in scientific research, and for having me as a part of many intriguing projects.

I would also like to thank my committee members Dr. Andrew Weiner, and Dr. Carson Slabaugh for their insightful advice to my PhD work and for all the knowledges I have learnt from their classes.

To all my colleagues and friends in the Applied Laser Spectroscopy Laboratory at B102, I would like to thank you all for your help and kindness during my PhD study. Especially, I would like to thank Dr. Aman Satija and Dr. Dong Han for their free "counseling services", delicate jokes, and all the inspiring days discussing about research as well as the best food around Lafayette. In addition, I want to thank my fellow PhD student Ziqiao Chang for always listening to my complaints, for bringing me lunches and dinners, and for assisting me with all the lab work, which, of course, includes moving the compressed gas tanks from time to time.

I would also want to acknowledge my family for the love and patience that they have devoted to me. My mom has raised me to become an independent and inquisitee person, and I know I have her support in all my endeavors.

Finally, I want to thank my girlfriend for her endless support and encourages. Especially during this year, many bad things have had happened, but we made them through. And I am really looking forward to the future adventures we are going to experience together.

TABLE OF CONTENTS

LIST OF TABLES

LIST OF FIGURES

ABSTRACT

Chirped-probe pulse femtosecond coherent anti-Stokes Raman scattering (CPP fs CARS) was used to study high pressure gas-phase thermometry. The experimental measurements were mostly performed in a static gas cell and in a canonical flat flame burner. The purpose of this study is to provide insights for the future rocket relevant combustion measurements.

The fundamental physics related to high pressure fs CARS were studied by formulating and solving a full set of time dependent density matrix equations (TDDM). In this work, TDDM was found useful in calculating the Raman excitation efficiency and in simulating the collision induced population and coherence transfer.

The optical effects associated with ultrashort pulse propagation in the high-pressure system were investigated. For example, the femtosecond pulse can receive large amount of frequency chirp when transmitting through thick glass windows of the optical section in the high-pressure system. The effects of pump and Stokes frequency chirp were investigated both experimentally, by inserting disks of SF11 glass into the pump and Stokes beam paths to study the flame thermometry, and theoretically by incorporating pulse chirp into the TDDM simulations to calculate the Raman excitation efficiency. Meanwhile, the ultrashort pulses can experience self-phase modulation in the high-pressure gas medium. The effects of self-phase modulation (SPM) on the power spectra of femtosecond pulses will have significant impact on the fs CARS profile. On the other hand, the extend and the behavior of SPM reply on the laser intensity and are also species-specific. The optimal laser intensities in high-pressure gas mediums like N_2, O_2, CO_2 and CH_4 were investigated.

To prepare for future rocket relevant combustion studies, CPP fs CARS thermometry was developed for CO_2, O_2 and H_2. Especially for CO_2 and O_2, they have close vibrational frequencies but very different coherence dephasing rates. Relative concentration between CO_2 and O_2 can then be extracted by using a short probe delay, and the temperature information can be determined by using long probe delays and the O_2 transitions will not interfere with CO_2 and nonresonant contribution of the CARS signal can be suppressed. CO_2 CPP fs CARS measurements inside the high-pressure high-temperature gas cell were presented and discussed. Collisional narrowing effects for CO_2 especially for high gas number density situation were discussed.

CHAPTER 1. INTRODUCTION

1.1 Motivation

Laser spectroscopy is a useful tool in combustion diagnostics. Compared to conventional non-laser-based techniques like using thermocouple for temperature measurement, most laser-based methods are nonintrusive and are more suitable for harsh environment measurements.

Combustion diagnostics at high pressure conditions are of practical interests for applications like gas turbine combustor, jet engine, rocket combustion and explosive material studies etc. For those systems, time-dependent and spatially resolved thermometric measurements are critical due to the fast combustion kinetics and turbulent thermo-fluid dynamics at high pressures. Among the many laser diagnostic techniques, laser induced fluorescence (LIF) is widely used for flame imaging. Typically, a monochromatic laser source in UV wavelength is used to excite the electronic transitions. The fluorescence signal will then be collected and analyzed through a photomultiplier tube (PMT). By creating planar laser sheets (PLIF) and using intensified cameras for detection, 2-D or even 3-D flame imaging with relative concentration and temperature distributions can be obtained. One of the limitations for high pressure LIF applications is that the collisional quenching rate also scales with gas number density. Meanwhile, the luminous flame can create significant background for LIF signal collection. Absorption spectroscopy is another popular diagnostic technique. Usually, optical intensity of a laser pulse is measured before and after its transmission through a gaseous medium to extract the material absorptivity and the subsequent temperature information. The collisional effects can be accounted into the spectral modelling through collisional line broadening and line shifting in absorption spectra, and flame chemiluminescence can be mitigated because the signal is laser-like. However, absorption spectroscopy is a beam path averaged measurement technique. To obtain spatially resolved measurement, usually a detection array and some tomography methods will need to be applied. Coherent anti-Stokes Raman scattering (CARS) is a third-order optical process. CARS is well-known for its high spatial resolution and accurate measurement precision in combustion diagnostics. Meanwhile, the CARS signal intensity scales quadratically with target molecule's number density, the laser-like signal also makes CARS convenient and efficient to collect in harsh environment like in high pressure systems.

A typical CARS setup usually requires a pump and a Stokes pulse to prepare the Raman excitation, and a probe pulse to frequency-couple the Raman coherence to generate the CARS signal. For many nanosecond CARS studies, a broad band dye laser will need to be used together with the nanosecond laser source to excite the Raman transitions, the major limitation of ns CARS for high pressure measurements are the slow laser repetition rate and the significant collisional effects due to the long laser-matter interaction timescale. The advent of commercially available ultrafast laser systems has made femtosecond CARS an alternative solution for high pressure combustion diagnostics. For example, for the femtosecond laser source that is featuring chirped pulse amplification (CPA), typical pulsed outputs are on the order of millijoules and with pulse repetition rates over 1 kHz. The high laser repetition rate enables better time resolution during experimental measurement, and the high laser intensity ensures sufficient CARS signal strength for single-shot detection while avoiding excess laser energy deposition.

In this thesis, a technique called chirped-probe pulse (CPP) fs CARS is used to perform the high-pressure studies. The probe pulse originates from the femtosecond laser source and is being frequency-chirped from about 50 fs to 3 ps to map the time domain Raman coherence into frequency domain analysis. The single laser source ensures no time jittering when synchronizing three laser beams. And the frequency chirp of the probe pulse can be easily reached by passing the femtosecond pulse through some dispersive glass rods, which simplifies the experimental setup and maximizes the energy transfer efficiency when proper material is used.

1.2 Research Objective

High pressure fs CARS measurements have attracted growing interests during the past few years. As it will be introduced in more details in the literature review, many recent studies have devoted to N_2 CARS measurements in a static high-pressure cell or some canonical flames in a high-pressure facility. However, for some practical high-pressure combustion applications like in rocket combustion studies, N_2 is usually unavailable because oxygen is used as the oxidizer. Thus, one of the objectives of this research is to develop fs CARS measurements and CARS thermometry for gaseous species other than N_2.

On the other hand, this thesis will approach aspects associated with femtosecond laser propagation in the high-pressure facility and high-pressure gas medium. For example, considerable amount of frequency chirp can be applied to the pump and Stokes pulses when the laser beams

transmit through thick glass windows of the high-pressure chamber. The effects of frequency chirp on Raman excitation efficiency profile were evaluated by solving the full set of time-dependent density matrix equations. Similarly, self-phase modulation can happen when intensive femtosecond laser beams transmit through high pressure gas medium, the consequence of self-phase modulation on the induced laser beam profile as well as on the fs CARS measurements will be discussed in this thesis.

High pressure fs CARS measurements of gaseous species like CO_2, O_2 and H_2 will be performed in a heated high-pressure gas cell. The objective is to successfully interoperate the CARS spectra from those measurements to extract temperature and species concentration information. The efforts of bridging from the gas cell measurement to a more practical rocket relevant combustion measurement will also be introduced in this thesis.

.

CHAPTER 2. LITERATURE REVIEW

2.1 Overview of CARS

2.1.1 Development of CARS for Gas Phase Measurement

Coherent anti-Stokes Raman scattering (CARS) spectroscopy was first demonstrated by Maker and Terhune in 1960s[1], the initial studies were performed in some crystalline to study the third-order susceptibilities of the isotropic materials. CARS started drawing attentions in gas phase combustion diagnostics in late 1970s[2-4] and since that it has been applied in many different combustion systems for thermometry measurement[5-8]. The accuracy of CARS thermometry has been verified through several approaches. For example, Farrow et. al compared the N_2 CARS temperature with the radiation-corrected thermocouple measurement in a methane diffusion flame and excellent agreement was obtained. In another study performed by Lucht et.al, N_2 and H_2 CARS measurements were performed in a non-premixed laminar flame over a Hencken burner and the extracted thermometry matched with the adiabatic flame temperature satisfactorily[9]. Besides, there are some studies comparing CARS measured temperatures with other laser diagnostic techniques such as spontaneous Raman scattering [10], absorption spectroscopy [11] and laser induced fluorescence spectroscopy[12]. Conventional gas phase CARS measurement usually requires a narrow band laser source together with a broadband dye laser to excite the full ro-vibrational transitions and to obtain good spectral resolution. To measure multiple species simultaneously, Eckbreth and Anderson et. al developed a dual-Stokes CARS system in which two broadband laser sources were used as the Stokes beams[13]. Similarly, the dual-pump CARS technique was proposed by Lucht to simultaneously measure N_2 and O_2 CARS spectra[14], this idea was latter evolved into a triple-pump CARS system to further extend its capability for multi-species measurements[15]. For all those CARS measurements with a nanosecond laser system or a broad band dye laser source, the major limitations are the shot-to-shot instability due to the laser fluctuation, the slow data acquisition due to the laser repetition rate and the strong nonresonant background due to the long-lasting laser durations. Femtosecond/picosecond CARS technique, on the other hand, has proven with more stable laser generation, faster data acquisition rate and easier suppression of nonresonant background as compared to those conventional CARS techniques.

2.1.2 Time-resolved Femtosecond CARS

The first gas phase time-resolved femtosecond CARS measurement was performed by Hayden and Chandler [16] on benzene and 1,3,5-hexatrine. For benzene, the Raman polarizability is mostly isotropic, Q-branch vibrational transitions are effectively excited, and the decay of the macroscopic polarization is thus due to the different frequencies of various Q-branch transitions. For 1,3,5-hexatrine, the anisotropic Raman polarizability results in spatially oriented sample of the molecule after pump-Stokes excitation, the overall polarization decay is mostly due to the excited molecules rotate away from their original orientations. M. Schmitt et. al [17, 18]measured the temporal evolution of the ro-vibrational features of iodine vapor as well as bromine, quantum mechanical calculations were proposed latter to simulate the wave-packet dynamics of different molecules in the ground electronic level. Time resolved fs CARS measurements for more combustion related species such as H_2, N_2 and CO_2 were latter conducted by M. Motzkus et. al [19-21]. The initial measurements were performed to retrieve ro-vibrational molecular constants as well as pressure dependent rotational relaxation coefficients from the fs CARS transients for long probe delays. As implied by the temperature dependence of the ro-vibrational transients, the first time resolved fs CARS thermometry was performed by Motzkus et. al on H_2 [20] and was latter applied to N_2 [22]. In Motzkus's studies, time-resolved fs CARS signal was recorded tens to hundreds of picoseconds after the impulsive Raman excitation, and the recursive Raman coherence information was fitted to get satisfactory temperature measurement.

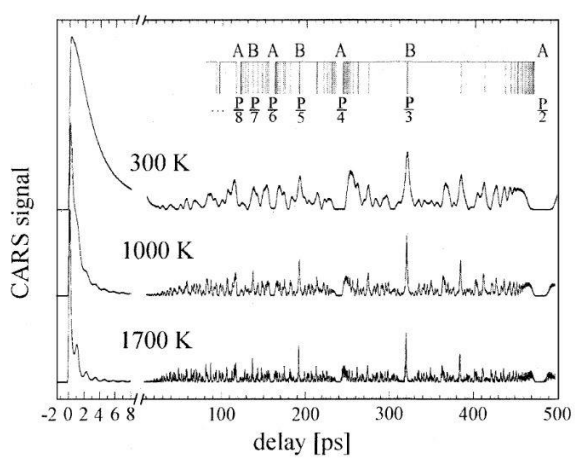

Figure 2.1 Simulated Q-branch fs-CARS transients for N_2 at 300, 1000 and 1700 K, respectively. A: Zones of silence, B: peaks suitable for single shot temperature determination, $p = 1/2\alpha_e$. C: periodicity of the vibrational CARS transients. The figure is from the work by Beaud et. al[22].

On the other hand, Lucht et al. investigated the fs CARS signal dephasing few picoseconds right after the impulsive pump and Stokes excitation [23] . Temperature information was extracted from the overall dephasing rate of the resonant polarization signal, which is also known as 'frequency spread decay. The switch from long probe delays to short probe delays enables 'collision free' measurement of fs CARS at elevated pressures (1-10 bar) because this initial 'frequency spread dephasing' is less susceptible to collisional induced effects. Temperature measurement using N_2 CARS was performed in a near adiabatic, hydrogen-air diffusion flames, and the measurement accuracy and precision were ±40K and ±50K respectively from 1500K - 2400K as reported in literature [24]

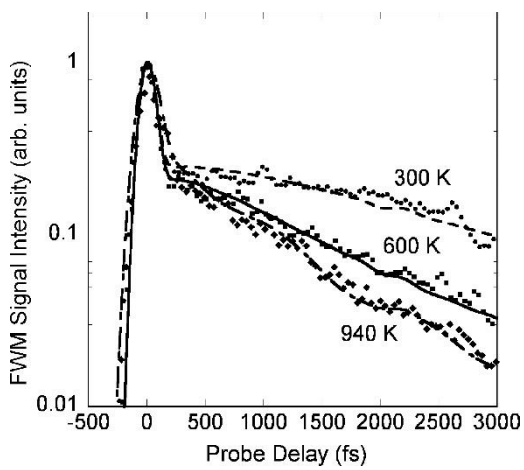

Figure 2.2 CARS (including resonant and nonresonant contributions) signal intensity vs probe time delay for air at temperatures of 300, 600, and 940 K. The pressure was 1 bar for all three temperatures. The figure was from the work by Lucht et. al[23].

Single shot femtosecond CARS in heated gas cell was first demonstrated by Lang et. al [25]. In that study, temperature dependent H_2 CARS signal was mapped into time domain analysis by using a linearly chirped probe pulse. However, the CARS signal was not collision free as the Raman polarization was probed 10 ps after Raman excitation. The applicability of single shot measurement significantly boosts the potential of fs CARS in more practical combustion diagnostics where high data acquisition rate will be required to resolve the fluid or thermal effects related transients. Also, single-shot femtosecond CARS measurement is more versatile and can be used for 1-D [26] or even 2-D [27] CARS thermometry measurement or a simultaneous time and frequency measurement[28] when proper laser configurations are applied.

2.1.3 Hybrid fs/ps CARS

The essential ideal of single-shot fs CARS is to change from time domain measurement to frequency domain measurement. In hybrid fs/ps CARS, broad band femtosecond pump and Stokes pulses are used to initiate Raman coherence in the gas medium, and the different frequency components in the giant Raman coherence is resolved by a narrow band probe pulse.

Nonresonant background suppression is also important in hybrid fs/ps CARS. Miller et. al used a 4f-pulse shaping system [29] to create frequency narrowed (FWHM ~ 12 cm^{-1}) 2.5 ps probe pulse that is time delayed to suppress the nonresonant background. With probe time delay of about 2.36 ps after pump & Stokes excitation of the N_2 ro-vibrational transitions, the nonresonant background was suppressed by 2 magnitudes while the resonant signal was found still strong enough for high temperature measurement. For temperatures up to 2400 K, they reported overall measurement precision of better than 2.2%. [30]

Choices of probe pulse optimization were also discussed, using a narrow band Lorentzian filter [31] or Fabry-Perot etalon [32] time asymmetric probe pulse can be generated. Compared with time symmetric narrow band probe pulse generated through 4-f pulse shaper, this time asymmetric probe pulse enables shorter probe delay necessary for non-resonant suppression and thus maintains higher signal strength as well as 'collision free' measurement in elevated pressures. The finest probe resolution as reported so far was by Scherman et. al [33]. In their study, the probe pulse was generated by sending a broad band femtosecond pulse into volume Bragg grating. With 0.7 cm^{-1} spectral resolution, the single shot measurement was able to resolve the full ro-vibrational features of N_2 spectra. The limitation, however, is that the low SNR at high temperatures due to the low laser power of probe pulse and high susceptibility to collisional effects because the temporal long probe pulse duration. On the other hand, Kearney investigated the influence of coarse probe resolution on vibrational CARS thermometry by using a 1.5 ps probe pulse [34]. No evidence showed this would degrade the fitting accuracy as compared to the conventional setup where probe pulse of few picoseconds was being used. This can be understood when we consider, for example, the broad bandwidth of the vibrational manifold as compared to the probe spectral resolution.

Pure rotational hybrid fs/ps CARS requires longer probe pulses (narrower linewidth) in order to resolve the rotational line structures. Longer probe delay will be needed for nonresonant suppression. By delaying an 8.4 ps probe by 13.5 ps with respect to pump/Stokes pulse, non-resonant background suppressed pure rotational N_2 CARS signals were used to extract J-level

dependent collisional dephasing rate [35]. In general, pressure dependent rotational linewidth corrections are needed for high pressure measurements and with long probe delays This could be a significant problem for complex combustion scenario where the molecular composition in the probe volume is mostly unknown. One of the limitations of using pure rotational hybrid fs/ps CARS at flame condition is the relative low efficiency of generating ps pulses through the femtosecond laser source either by 4-f grating or Lorentzian filter. Kearney et. al [34] proposed narrow band (3.5 cm^{-1}) probe pulse generation through second harmonic bandwidth compression (SHBC). For 2.8 mJ 800 nm input pump pulse with 100 fs pulse length, the second harmonic generation energy can reach as high as 1.1 mJ. This facilitates first pure rotational hybrid fs/ps CARS thermometry at flame measurements with good accuracy and precision [34].

At relatively low temperatures, pure rotational CARS was found to be more accurate than hybrid fs/ps vibrational CARS because rotational levels can be more efficiently excited as compared to vibrational levels. On the other hand, vibrational CARS usually exhibited better measurement accuracy at high temperatures. The incorporation of simultaneous pure rotational and vibrational CARS measurements was realized by Chloe et. al [36] by using a dual pump lasers. Satisfactory measurement accuracy was obtained over a wide temperature range from 298-2400 K.

2.1.4 Chirped Probe Pulse Fs CARS

Unlike the time resolved analysis in Lang's studies [37], an alternative solution is to use a frequency chirped probe pulse (CPP) to map the time-resolved ro-vibrational molecular dynamics into frequency domain directly for single shot measurement. Vibrational CPP fs CARS measurement with 1 kHz acquisition rate was first demonstrated by Roy et. al [38] and was applied in H_2-air flame stabilized over a Hencken burner [39]. Accuracy and precision were found to be approximately 1%-6% and 1.5%-3% for temperature range from 300-2400K.

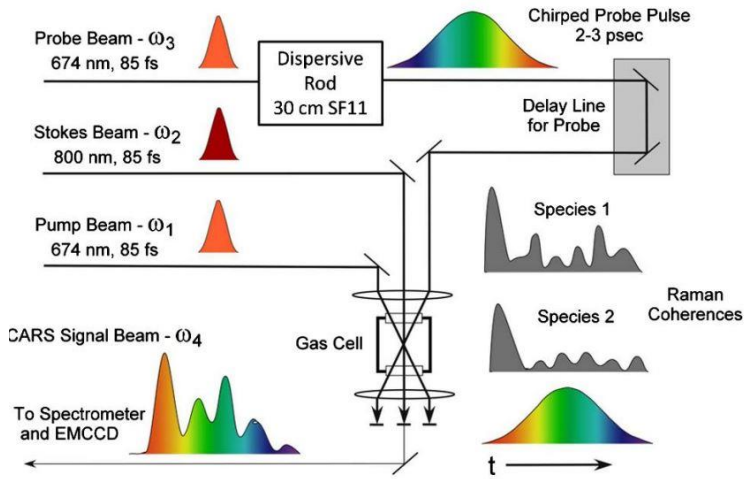

Figure 2.3 Optical layout used for Chirped-probe-pulse fs CARS measurements. The figure is from the work by Richardson et. al.[40]

The theoretical modelling for the CPP fs CARS spectral fitting was developed and discussed in detail by Richardson et. al [41]. This spectral fitting code was further refined by Thomas et. al [42] by introducing a weighted fitting scheme and shall be discussed in more details in the following chapters.

Nonresonant suppression through a delayed probe pulse was also used in CPP fs CARS[43]. Richardson et. al also investigated the suppression of the non-resonant background by polarization control [44].

Except from fundamental ro-vibrational constants extraction and the applications of temperature measurement, CPP fs CARS as well as fs/ps CARS were also being investigated for concentration measurement [40, 45] and pressure measurement [46]. Aided by all those fundamental spectroscopic studies, single shot frequency resolved fs CARS measurements have been utilized for more practical combustion related applications. For example, detailed flame characteristics in a gas turbine combustor with significant swirl and high levels of turbulence were revealed by Dennis et al. through using a 5-kHz CPP fs CARS system [47, 48]; the same laser system was later being applied to turbulent spray flames by Thomas et. al [49, 50]; Hybrid fs/ps CARS was also being applied in different consequences such as in metalized propellant combustion[51], canonical flat flames [52], and dielectric barrier discharge plasma transients [53]. The comparison between CPP fs CARS and hybrid fs/ps CARS has been discussed by Richardson et. al [54], though the temperature range being investigated is all above 1000K. In general, the

spectral fitting routine for hybrid fs/ps CARS is simpler as it reduces the maximum number of laser parameters needed. On the other hand, CPP fs CARS benefits from simpler experimental setup as it requires only dispersive material such as chirping glass to generate picosecond length pulse, while for hybrid fs/ps CARS, either a pulse shaper or a SHBC would be needed for bandwidth compression. As a result, the probe pulse generation efficiency is also much higher by using CPP fs CARS. For example, with proper anti-reflection coating, nearly 100% probe pulse generation efficiency can be achieved by using long chirping glass, the generation efficiency through SHBC is about 40% as reported by Kearney et. al [55], higher probe pulse energy brings up higher SNR especially at high temperature conditions. In the meanwhile, CPP fs CARS can reveal all the ro-vibrational transitions from the frequency beating featuures while the hybrid fs/ps CARS is only optimized for either pure rotational or pure vibrational transitions as is limited by the probe bandwidth. However, it was also found that satisfactory temperature measurement accuracy and precision can be obtained by using both techniques

2.2 CARS Measurement at High Pressure Condition

2.2.1 Collisional Effects

Rotational collisions can result into collisional line broadening and even collisional line mixing (narrowing) in spectroscopic analysis, and the collisional frequency increases with higher molecular density. Thus, rotational collision is an essential topic in many high-pressure CARS studies. Pressure induced collisions are more frequently encountered, and usually more thoroughly studied in ns CARS measurements. This is because the nanosecond time scale of laser pulse duration matches with the typical collisional time scale.

The rate of molecular collisions can be approximated by some semi-empirical fitting laws. For most of the semi-empirical laws, a mathematical formula is given with some floating parameters which can be determined by the experimental measurements. And those parameter sets are usually different when the collisional partner changes. Even for the same gaseous species, the parameters might need to be adjusted in different pressure and temperature range. Among those fitting laws the exponential gap law (EGL) and the energy corrected sudden law (ECS) are most widely used. EGL law is usually given in a form as

$$\gamma_{ij} = \alpha\, p \cdot \exp\left(-\beta \Delta E / k_b T\right) \tag{1.1}$$

where γ_{ij} denotes the collisional rate, ΔE is the energy difference between the initial and final state of collision, T is the temperature and α, β are just the floating parameters. Koszykowski et. al explained the collisional narrowing effects in room temperature N_2 CARS measurement when pressure increases from 1 to 10 atm [56]. They latter used a more advanced form of EGL law expression and successfully extracted the fitting parameters from their experimental measurements under 10 atm [57, 58]. The pressure and temperature range validity was extended by Bouche et. al[59], they measured N_2 Q-branch transitions up to 2500 bar and 700 K, the experimental measurements matched with their calculations when EGL law was used. ECS fitting laws was proposed by De Pristo et. al[60], it usually takes a more complex form as compared to EGL law as

$$\gamma_{J'J} = \left(2J'+1\right) exp\left[\left(E_J - E_{J>}\right)/k_B T\right] \Omega^2{}_{J>} \times \sum_L \begin{pmatrix} J & J' & L \\ 0 & 0 & 0 \end{pmatrix}^2 \left(2L+1\right) \Omega_L^{-2}\, ReW_{0L} \tag{1.2}$$

where Ω is the adiabatic factor, for diatomic molecule like N_2 it is given as

$$\Omega_J = \frac{1}{1+\Delta\omega\tau_c{}^2/24} \tag{1.3}$$

$J>$ is the greater of J and J'. ReW_{0L} is the basis rate constant and it can have several forms. For example, for ECS-P scaling law the basis rate is usually given in a form of[61]

$$ReW_{0L} = -\frac{A(T)}{\left[L\left(L+1\right)\right]^{\alpha}} \tag{1.4}$$

and $A(T)$ is a temperature dependent floating function and α is also a fitting parameter. Lavorel et. al measured N_2 CARS spectrum and compared the Q-branch linewidth with ECS fitting law and good agreement was obtained for temperatures up to 2400 K. In another study, they validated ECS fitting law at room temperature and pressure up to 35 atm [62]. There were also some recent studies investigating the validity of ECS fitting laws for N_2-N_2 collisions from low pressure region (0.2 bar) to moderately high pressure region (5 bar) using time-resolved femtosecond CARS measurements and excellent agreement was reported[63, 64]. Many other studies compared the accuracy between EGL law and ECS law in terms of accurately modelling the collisional linewidth and it turns out both of them give satisfactory performance when the fitting parameters are properly chosen[65, 66].

The collisional rate calculation among different gaseous species are of practical interests for high pressure CARS diagnostics. For example, N_2 collisional linewidth and line shift coefficient in

CH_4-N_2 mixture [67] or in a H_2-N_2 [68-70] mixture were measured and well-characterized by scaling laws in an extensive pressure range. Bonamy et. al[71] measured collisional linewidth of N_2 in a N_2-CO_2-H_2O system and the linewidth was also modeled using EGL law. The target species of collisional linewidth studies are not confined to simple diatomic molecules like N_2 and O_2. Buldyreva[72] investigated C_2H_2 pure rotational CARS spectra for pressures up to 6 bar and the linewidth was modeled using a semi-emperical Robert-Bonamy formalism. More recently, Jiang et. al[73, 74] measured CO_2 *S*-branch linewidths broadened by CO, CO_2, O_2, Ar and C_2H_4 using a picosecond CARS system.

In general, collisional effect is critical in high pressure CARS studies. On the other hand, due to the complexities of molecular collisions especially when multiple species are involved, it is preferable to avoid the collisional interferences in femtosecond CARS studies if it is possible.

2.2.2 Frequency Chirp Effects

Frequency chirp occurs when a spectrally broad pulse propagates through dispersive materials such as glass windows. Different frequency components of the pulse will experience indices of refraction. This causes a frequency dependent delay such that the overall pulse length is stretched in time. For normal dispersion, the low frequency component experiences a lower index of refraction and thus travels ‘faster’ than the high frequency component, while for abnormal dispersion cases are reversed. Unlike in our previous introduction for CPP fs CARS where the probe pulse is usually chirped extensively from tens of femtoseconds to few picoseconds, the frequency chirp that is going to be discussed in the following section is mainly for the pump and Stokes pulses. The extent of the frequency chirp is relatively small as compared to the chirped probe pulse. This discussion will be of practical interest because for most high pressure measurements where femtosecond pulses must travel through thick glass windows in order to reach the probe volume, the pump and Stokes beams will experience moderate amount of frequency chirp.

The technique of using chirped pump and Stokes pulses in fs CARS was first demonstrated by Nibbering et. al [75]. In their study, considerable degree of frequency chirp was induced for both pump and Stokes pulses. By tuning the pump and Stokes delay, the instantaneous frequency difference between pump and Stokes pulses was precisely controlled so that specific Raman transitions were excited sequentially. This technique is also known as ‘spectral focusing’, depending on the application, selective excitation or spectral resolution enhancement [76-82] can

be achieved. Kearney[34, 79] used spectral focusing to vary the spectral regions from which pure rotational CARS spectra of N_2 were generated, and to minimize the effect of the nonresonant background on the measured single-laser-shot pure rotational CARS signals. In his study, the pump and Stokes frequencies were degenerate. Thus, the Stokes delay was tuned to shift the Raman excitation profile towards a transition frequency of interest. This may lead to degradation of the overall Raman excitation efficiency with increasing amount of Stokes delay. Richardson et al. [41] investigated frequency chirp as a spectral fitting parameter in CPP fs CARS modelling, yet the Raman excitation efficiency was assumed to be identical for all Q-branch transitions and the nonresonant narrowing as a result of frequency chirp was not considered at that time. In spectral focusing studies by Wrzesinski et al., mechanical stages were used to scan the pump and Stokes delay in order to resolve the full spectral information [83]. The tradeoff, however, is that single shot measurements with high data acquisition rates are not available. More recently, Marrocco developed a numerical model to interpret the experimental vibrational CARS spectrum as well as pure rotational CARS signal where the extent of frequency chirp is significant [84].

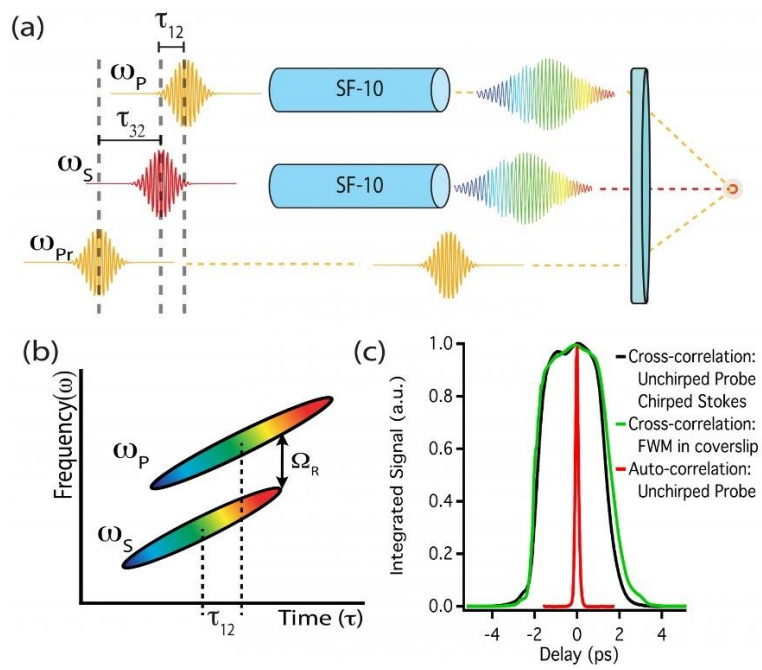

Figure 2.4 (a) Schematic layout of the optical setup. (b) Time-vs-frequency diagram for chirped pump and Stokes pulses. The excited Raman transition Ω_R is dependent on the relative delay τ_{12} between the two pulses. (c) Cross-correlation (black) of the unchirped probe and chirped Stokes, cross-correlation (green) between the chirped pump/Stokes and unchirped probe, and auto-correlation (red) of two unchirped probe pulses. The figure is from the work by Wrzensinski et. al.[83]

The inclusion of frequency chirp is important for high pressure CARS measurement especially when thick glass windows is used. The most obvious effects of frequency chirp in CPP fs CARS is to affect the Raman excitation efficiency profile and cause the spectral narrowing of the nonresonant signal.

2.2.3 Self-phase Modulation

Self-phase-modulation (SPM) is a nonlinear Kerr-like phenomenon in which an ultrashort pulse accumulates temporal phase as it propagates through a gas medium [85-87]. This nonlinear phase accumulation depends on the intensity profile of the laser pulse and the nonlinear refractive index of the gas. In the study of Nibbering et al. [88], the nonlinear refractive index was measured for N_2, O_2 and Ar at pressures up to 1.6 bar by recording the power spectrum of the transmitted pulses. Nibbering et al. [88] used a well-collimated, unfocused 120-fs, 800-nm beam directed through a 2.5-m long gas cell to measure self-modulation effects. At the exit of the cell, they selected the central 1-mm-diameter region of the beam for spectral analysis. In more recent studies by Langevin et. al [89] and by Wahlstrand et. al [90], the nonlinear refractive index of N_2 was measured for several different pulse durations because variations in the pulse duration can affect the accuracy of retrieving the nonlinear refractive index. While most of the studies reported the measurements of nonlinear refractive index near atmospheric pressure [91], the pressure dependence of the nonlinear refractive index was measured by Börzsönyi et al. [92] for pressures up to 1 bar. It was found that, for these pressures, the nonlinear refractive index was approximately proportional to pressure for several inert gases such as N_2 and Ar.

Obviously, for high pressure fs CARS measurement, the self-phase modulation effect could lead to femtosecond pulse profile changing when it transmits through the high-pressure gas medium. This could become more complex in high pressure combustion studies as the fractions of gas species in the combustion product is not known in priori. Thus, elimination of suppression of SPM would be ideal, this can be done by tuning down the laser intensity.

2.2.4 CARS Studies for H_2, O_2 and CO_2,

Theoretical modelling for H_2 and O_2 CARS spectrum are similar to N_2. For H_2, spectroscopic information including the line position[21, 93], transition strength and linewidth modelling has been

studied by different groups. Accurate linewidth model for H_2 CARS for a wide pressure range is hard to obtain because Doppler's broadening is more significant for light molecules. Though, H_2 CARS (ns or fs) for thermometry measurement has been reported and found to be accurate especially at high temperature flames and rocket combustion environment.

Theoretical modelling of the CO_2 CARS spectrum requires detailed spectroscopic information such as line positions, collisional line widths, and Raman cross sections [94]. Ab initio calculations of force constants for CO_2, considering Fermi resonances, were performed by Suzuki et al [95]. Measurements of Raman cross-sections of vibrational modes of CO_2 were tabulated by Rothman et. al [96]. Investigations of collisional linewidths were performed using semi-empirical scaling laws [97] or directly from diffusion model calculations [98]. Recent spectroscopic studies of CO_2 have focused on bridging the gap between the experimental measurements and the ab initio calculations that were performed using different potential energy surfaces, over a wide range of temperatures [99]. The measurements of absolute Raman cross sections for CO_2 vibrational transitions has focused mostly on the Fermi dyads (1285 cm^{-1} and 1388 cm^{-1}) [100]. Tejeda et. al. reported [101] calculations of the first and higher order derivatives of the CO_2 mean polarizability based on experimentally measured Raman intensities from some weak Fermi resonances as well as from the $2\nu_3$ overtone. Similar studies were performed by Sanchez et. al [102]. They developed an algebraic model to calculate derivatives of the Raman polarizability which showed good agreement with the ab initio calculations [103] as well as with the experimental measurements [101]. They also simulated the spontaneous Raman spectrum of CO_2 at a flame temperature of 1743 K and the comparison between their simulations and experiments was satisfactory[104].

Examples of practical applications of CO_2 CARS include measurements in the exhaust stream of a swirl-stabilized JP-8-fueld combustor under sooting conditions [105] as well as measurements inside an optically accessible gas turbine combustor facility [105, 106]. In these measurements, a N_2-CO_2 dual-pump CARS system with narrow band pump laser sources and a broadband Stokes laser source was employed. Temperature and relative species concentration were obtained from the frequency resolved N_2-CO_2 dual-pump CARS spectrum. Recently, Roy et. al demonstrated CO_2 fs CARS measurement by using a single 7-fs broad band pulse [107]. Kerstan et al. [108] obtained femtosecond CARS spectra for CO_2 with a two beam configuration. In their study, a 7 fs pump/Stokes pulse was used to excite the CO_2 vibrational Raman coherences, which were then probed by a 1 ps probe pulse. Those measurements were performed in a heated gas cell and the

fitted temperatures, between 300 K-900K, were in good agreement with experimental results.

An interesting aspect of CO_2 fs CARS is that since the vibrational frequency of O_2 (1556 cm^{-1}) is very close to that of CO_2 (1388 cm^{-1}), both vibrations are excited due to the broad bandwidth of the pump and Stokes pulses. Kulatilaka et al. [109] performed time-resolved fs CARS measurements for CO_2 and O_2 mixtures in a gas cell at temperatures from 300 K to 900 K with varying CO_2-O_2 concentrations. They found that the frequency-spread dephasing rate of CO_2 was much slower than that of O_2. This indicates that by delaying the arrival of the probe pulse one can suppress the O_2 resonant contribution. Similar studies, by Seeger et.al., used a delayed probe pulse to temporally separate the N_2/O_2 pure rotational CARS signals from the unwanted non-resonant contributions for thermometry/concentration analysis [110]. In work by Bitter et al. [26] the probe pulse was delayed by a few hundred picoseconds to fully suppress the resonant contributions from O_2 molecule. By measuring the CARS intensity at two probe time delays (PTDs) they obtained the relative concentrations of CO_2 and O_2 [111].

2.2.5 Practical CARS Measurements at High Pressure Condition

High pressure gas cell can provide a well-controlled pressure and temperature condition for CARS measurement, and it is an important preparation work for further high-pressure combustion diagnostic studies. One of the goals of high-pressure cell CARS studies is to increase the pressure and temperature range of measurement. Lucht et. al[23] reported time resolved fs CARS measurement of N_2 inside a high pressure gas cell. For pressure range from 1 to 10 atm and temperature range from 300-940 K, they found that the dephasing of the Raman transitions was not affected by pressure within the first few picoseconds of impulsive Raman excitation. This finding indicates that “collisional free” measurement is still valid within a moderate pressure range if a proper probe delay is chosen. Wrzesinski et al.[112] extended this high pressure gas cell measurement to pressures up to 50 bar, for both N_2 and O_2, they concluded that accurate thermometric measurements could be made within the first 1-3 picosecond range without the need to account for collisional effects.

Miller et. al[35] reported hybrid fs/ps CARS measurement for N_2 pure rotational transitions. In their study, it was found that the ‘collision free’ assumption was valid for N_2 and O_2 for pressures up to 15 atm. Though, they only reported measurement at room temperature. Courtney et. al[113, 114] reported N_2 pure rotational CARS measurement in a heated high pressure gas cell with hybrid

fs/ps CARS. Satisfactory thermometry measurement was reported for pressure ranges from 1-70 atm and temperature ranges from 300-1000 K. Due to the broadband nature of the femtosecond pulse, in their studies, a single 42 fs pulse was spectrally broad to excite pure rotational transitions, the Raman coherence was then scattered by a narrow band probe pulse. They claimed pure rotational CARS was less susceptible to pressure induced broadening due to the greater transition frequency separation, thus it was more ideal for high pressure CARS measurement. On the other hand, the transition frequency difference among different gaseous species are usually smaller in terms of their pure rotational transitions than their vibrational transitions, this could be problematic in practical combustion applications as gaseous mixtures are usually unavoidable.

As best to our knowledge, fs CARS studies in high pressure flames are very limited. This is partly due to the complexities of high-pressure combustion phenomenon as well as some nonlinear optical effects involved in high pressure environment. By setting up canonical combustion system in a well-controlled high pressure chamber, fs CARS measurement in a high pressure flame was made available by Stauffer et. al[115]. In their study, a Hencken burner was modified and installed inside a high-pressure facility, both CH_4-Air and H_2-Air flames were tested for pressures up to 10 bar and N_2 vibrational CARS was applied for thermometry measurement. Good thermometry accuracy and precision were obtained for adiabatic flame temperatures ranging from 1300-2300 K. They compared the CARS measurement both at short probe delay (200-300 fs) and at long probe delay (30ps) cases, it was found that for short probe delay the collisional effect could be neglected while accurate collisional linewidth modelling would be required for long probe delay scenario.

No femtosecond CARS measurement has been done or at least been reported yet in any rocket combustor. However, there are some nanosecond CARS studies in a high pressure liquid rocket engine[116, 117] or in a pulsed combustion chamber[118, 119] and the typical pressure range is from 1-4 MPa and temperature range is from 1000K to 3000K. In those studies, gaseous species like H_2, O_2, CO_2 and CH_4 were frequently used other than N_2 for CARS measurements because O_2 is used as the oxidizer. Challenges associated with those studies include the unstable flame condition. Especially for ns CARS system, the slow laser repetition rate made it hard to capture the time transient of high-pressure combustion process. The femtosecond CARS system, on the other hand, would allow much faster data acquisition. But other obstacles could arise for fs CARS measurements as well. For example, due to the much higher laser intensity in fs CARS system than ns CARS system, it is more likely to introduce nonlinear optical effects such as self-phase

modulation (SPM) when a femtosecond pulse transmits through high pressure gas medium. Besides, a high pressure combustion facility usually requires thick glass windows as optical access, the transmission of femtosecond pulse through those windows could also induce significant amount of frequency chirp and thus it will also need to be accounted for CARS modelling.

CHAPTER 3. THEORY OF CPP FS CARS

3.1 Wave Equation Derivation of CARS

The wave equation derivation of CARS in this section follows the framework by Eckbreth et. al [120-122].

Based on Maxwell's equations, the general wave equation that relates the laser electric field and the induced polarization is given as

$$\nabla^2 \vec{E} - \frac{1}{c^2}\frac{\partial^2 \vec{E}}{\partial t^2} = \mu_0 \frac{\partial^2 \vec{P}}{\partial t^2} \tag{2.1}$$

Both the overall electric field and the induced polarization can be written as a function of a sum of different fields each with its own optical frequency

$$\vec{E} = \sum_j \vec{E}\left(\omega_j, \vec{r}\right) \cdot e^{-i\omega_j t} \tag{2.2}$$

$$\vec{P} = \sum_j \vec{P}\left(\omega_j, \vec{r}\right) \cdot e^{-i\omega_j t} \tag{2.3}$$

Substitute Eq.(2.2) and Eq.(2.3) into Eq.(2.1) and separate terms with same optical frequency we can have

$$\nabla^2 \vec{E}\left(\omega_j, \vec{r}\right) + \frac{\omega_j^2}{c^2}\vec{E}\left(\omega_j, \vec{r}\right) = -\mu_0 \omega_j^2 \vec{P}\left(\omega_j, \vec{r}\right) \tag{2.4}$$

Given that in an isotropic medium, like in most gas phase environment, the even order of nonlinear terms is zero because the energy potential is centrosymmetric. Including first and third order nonlinear response as higher order polarization is negligible, we can obtain that

$$\vec{P}\left(\omega_3, \vec{r}\right) = \vec{P}^{(1)}\left(\omega_3, \vec{r}\right) + \vec{P}^{(3)}\left(\omega_3, \vec{r}\right) = \varepsilon_0 \chi^{(1)} \vec{E}\left(\omega_3, \vec{r}\right) + \vec{P}^{(3)}\left(\omega_3, \vec{r}\right) \tag{2.5}$$

$$\nabla^2 \vec{E}\left(\omega_3, \vec{r}\right) + \frac{\omega_3^2}{c^2}\frac{\varepsilon}{\varepsilon_0}\vec{E}\left(\omega_3, \vec{r}\right) = -\mu_0 \omega_3^2 \vec{P}^{(3)}\left(\omega_3, \vec{r}\right) \tag{2.6}$$

The third order polarization can be expressed in terms of third order polarizability and the interactive electric fields as

$$P_i^{(3)}\left(\omega_3, \vec{r}\right) = \varepsilon_0 \sum_{jkl} \chi_{ijkl}^{(3)}\left(\omega_3, \omega_0, \omega_1, \omega_2\right) E_j\left(\omega_0, \vec{r}\right) E_k\left(\omega_1, \vec{r}\right) E_l\left(\omega_2, \vec{r}\right) \tag{2.7}$$

The subscript i, j, k, l represent the Cartesian coordinate indices (denoting the direction of polarization) and ω_0, ω_1, ω_2 are the optical frequencies of the three electric fields. There are many conventions of putting electric field component in a certain sequence, in this study, we write the susceptibility in a way that the first optical frequency equals the summation of the rest of the three. For CARS process, specifically, we can write Eq.(2.7) as

$$P_i^{(3)}\left(\omega_3,\vec{r}\right)=\varepsilon_0\sum_{jkl}\chi_{ijkl}^{(3)}\left(\omega_3,\omega_0,-\omega_1,\omega_2\right)E_j\left(\omega_0,\vec{r}\right)E_k^*\left(\omega_1,\vec{r}\right)E_l\left(\omega_2,\vec{r}\right) \tag{2.8}$$

Assuming parallel polarization for all three electric fields, the permutation symmetry and the isotropic property of the gas medium reduces the summation into a simple form as

$$P^{(3)}\left(\omega_3,\vec{r}\right)=\varepsilon_0\chi_{CARS}E\left(\omega_0,\vec{r}\right)E^*\left(\omega_1,\vec{r}\right)E\left(\omega_2,\vec{r}\right) \tag{2.9}$$

where χ_{CARS} is the CARS susceptibility and is an intrinsic property of the gas medium, it can be written in forms of a resonant and nonresonant contribution as

$$\chi_{CARS}=\sum_j\frac{K_j\Gamma_j}{2\Delta\omega_j-i\Gamma_j}+\chi_{nres} \tag{2.10}$$

K_j denotes the transition strength and Γ_j is the transition linewidth. $\Delta\omega_j$ is given as $\Delta\omega_j=\omega_j-\left(\omega_0-\omega_1\right)$ where ω_j is the transition frequency. The resonant response is maximized when the laser frequency matches with the transition frequency ($\Delta\omega_j=0$). The nonresonant contribution is also known as the degenerate four wave mixing process and has the same frequency as the resonant CARS signal. A typical energy level diagram of CARS process is shown in Figure 3.1.

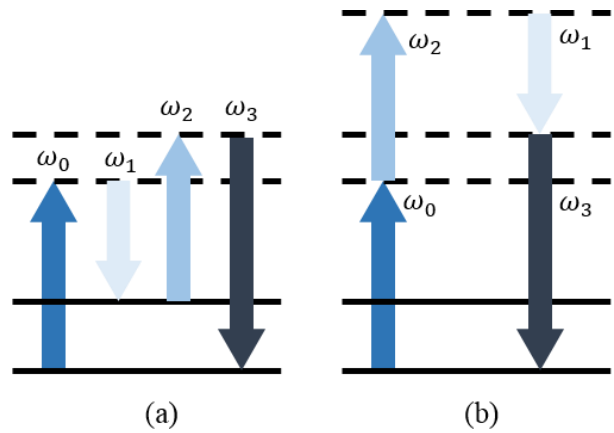

Figure 3.1 Typical energy level diagram for (a) CARS process and (b) nonresonant degenerate four wave mixing process

The spatial dependence of the electric field can be expressed in terms of a travelling wave as

$$E\left(\omega_i,\vec{r}\right)=E\left(\omega_i\right)e^{i\vec{k}\cdot\vec{r}} \tag{2.11}$$

Substituting Eq.(2.9) and Eq.(2.11) into Eq.(2.6), and assuming the CARS signal is propagating through z direction, we can further show that

$$\frac{d^2E\left(\omega_3\right)}{dz^2}+2i\vec{k}_3z\frac{dE\left(\omega_3\right)}{dz}=-\frac{\omega_3^2}{c^2}\chi_{CARS}E\left(\omega_0\right)E^*\left(\omega_1\right)E\left(\omega_2\right)e^{i\left(\vec{k}_0-\vec{k}_1+\vec{k}_2-\vec{k}_3\right)z} \tag{2.12}$$

Assuming slowly varying amplitude of the CARS electric field over propagation, the second order derivative is negligible as compared to the first order derivative thus can be omitted. The integration of the CARS electric field over the z direction $\int_0^l dz$ can give the CARS intensity formula as

$$I\left(\omega_3\right)=\frac{1}{2}c\varepsilon_0\left|E\left(\omega_3\right)\right|^2=\frac{\omega_3^2}{c^4\varepsilon_0^2}I_0I_1I_2\left|\chi_{CARS}\right|^2l^2\left[\frac{sin\left(\Delta\vec{k}l/2\right)}{\Delta\vec{k}l/2}\right]^2 \tag{2.13}$$

$\Delta\vec{k}$ is the spatial phase mismatch and l is the propagating distance where CARS intensity is accumulated. (when the propagating vectors for three electric fields are collinear, the spatial phase mismatch can be reduced to a scalar). Obviously, the growth of integrated CARS intensity will become negligible when Δkl becomes nonzero. The CARS signal is thus generated and propagated in a certain direction which is dictated by the phase matching condition as

$$\vec{k}_3=\vec{k}_0-\vec{k}_1+\vec{k}_2 \tag{2.14}$$

3.2 Modelling of CPP Fs CARS

3.2.1 Governing Equations

In CARS process, molecular polarization is introduced by the incident pump and Stokes pulses and then frequency-coupled to a probe laser. There are two types of molecular polarizations, the resonant polarization which is associated with the rovibrational transitions within the sample molecule, and the nonresonant polarization which is due to the instantaneous electronic contribution.

Assuming linearly polarized pump and Stokes pulses at the same direction, the nonresonant and resonant molecular polarizations can be modelled in time domain as

$$P_{nres}(t) = E_{pu}(t) E_{St}^{*}(t) \tag{2.15}$$

$$P_{res}(t) = \beta \left[\int_{-\infty}^{t} E_{pu}(\tau) E_{St}^{*}(\tau) d\tau \right] \sum_{i} \left\{ \Delta N_i \left(\frac{d\sigma}{d\Omega} \right)_i f_i \cos(\omega_i t + \phi) e^{-\Gamma_i t} \right\} \tag{2.16}$$

where β is the relative resonant to nonresonant scaling parameters that will be determined in the spectral fitting routine to match with the experimental data. ΔN_i is the difference of the Boltzmann population distribution between the upper and lower energy level within the molecular transition. $(d\sigma / d\Omega)_i$ is known as the Raman cross section and is calculated from the Raman tensor invariants. f_i is the Herman-Wallis correction factor which accounts for the influence of centrifugal force on the intensity of spectral lines, Herman-Wallis correction factor is found to be more significant in small molecules like H_2 other than molecules like N_2 due to the stronger rovibrational coupling. In some conventions, the Boltzmann population distribution and the Herman-Wallis correction factor will be all incorporated in the Raman cross section calculations. ω_i and Γ_i are the transition frequencies and transition linewidth respectively. ϕ is a constant phase shift between the resonant and nonresonant polarization. The summation is over all molecular transitions for a certain molecule, when there are multiple species present in the probe volume and their transition frequencies are close, the summation of all possible contributions from those gas species will also be needed.

The CARS electric field can be modeled as the product between the probe electric field and the molecular polarizations

$$E_{CARS}(t) = E_{pr}(t) \left[P_{res}(t) + P_{nres}(t) \right] \tag{2.17}$$

In Figure 3.2, we showed a time domain representation of the molecular polarizations. In time domain, P_{nres} is transient while P_{res} has a much longer dephasing time scale. Experimentally, the choice of probe pulse delay can affect the CARS signal by interacting the probe electric field with different part of the Raman coherence. In this thesis, since a chirped probe pulse with a probe pulse width of 3 ps is used, usually a minimum 3 ps probe time delay will be needed in order to suppress the nonresonant signal. In some studies, when a time asymmetric probe pulse is used[31], the necessary probe pulse delay can be reduced to fully get rid of the nonresonant interference.

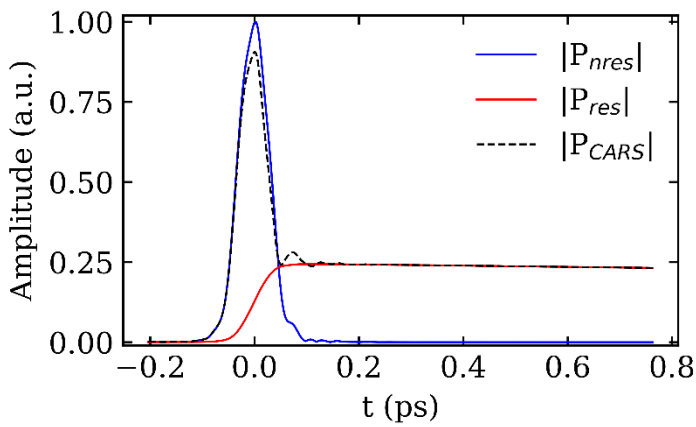

Figure 3.2 Time domain representation of the magnitude of the resonant, nonresonant and CARS polarization.

Figure 3.3 shows a theoretical calculation of the resonant and nonresonant contribution of N_2 CARS signal at room temperature and 2300 K. For higher temperature, as more rovibrational transitions are excited, the resonant signal decays faster. The relative magnitude of the resonant to nonresonant contribution of CARS intensity is thus much lower at high temperature. The modulation pattern of the CPP fs CARS spectrum is as a result of the alternating phase difference between the resonant and the nonresonant contributions. Besides, the recursive patterns of resonant Raman coherence can be observed near 15100 cm^{-1} and 15250 cm^{-1} are due to the first and second hot band transitions. Those temperature dependent features are essential in the CARS spectrum fitting to help determine the CARS thermometry. In the following sections, we will introduce the electric field characterization, the calculation for Raman transition frequency, strength, and linewidth in more details.

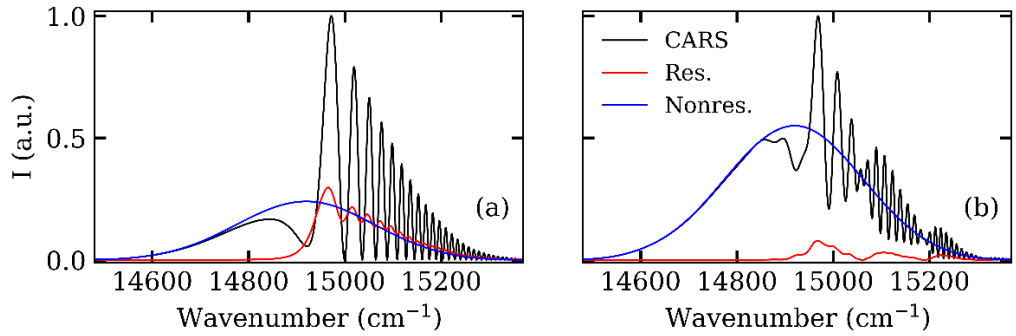

Figure 3.3 Simulated N_2 CPP fs CARS signal and its resonant and nonresonant contributions at (a) 298 K and (b) 2300 K. The probe time delay is 0.5 ps.

3.2.2 Characterization of Laser Electric Field

In general, the time domain electric field expression for a given pulse can be given as:

$$E(t) = E^{(+)}(t) + E^{(-)}(t) = \frac{1}{2}(A(t)e^{-j\omega_0 t} + A^*(t)e^{+j\omega_0 t}) \tag{2.18}$$

Written as Eq. (2.18), the electric field can be understood as having both positive and negative frequency component. When we consider for a four-wave mixing (FWM) process like CARS. All the possible nonlinear FWM signals can be written as following

$$I \propto \left| E_{pu} \cdot E_{St} \cdot E_{pr} \right|^2 \tag{2.19}$$

After substituting the electric field expression in Eq. (2.19) into Eq. (2.18), we can further get

$$I \propto \left| \left(E_{pu}^{(+)} + E_{pu}^{(-)}\right)\left(E_{St}^{(+)} + E_{St}^{(-)}\right)\left(E_{pr}^{(+)} + E_{pr}^{(-)}\right) \right|^2 \tag{2.20}$$

The expansion of Eq. (2.20) gives 8 terms in total, the over-count of the complex conjugate pairs reduces the total number to 4 and they are sorted as: 1). $E_{pu}^{(-)} \cdot E_{St}^{(+)} \cdot E_{pr}^{(+)}$; 2). $E_{pu}^{(+)} \cdot E_{St}^{(-)} \cdot E_{pr}^{(+)}$; 3). $E_{pu}^{(+)} \cdot E_{St}^{(+)} \cdot E_{pr}^{(-)}$; 4). $E_{pu}^{(+)} \cdot E_{St}^{(+)} \cdot E_{pr}^{(+)}$

For different specific laser setup, the above four FWM signals can be distinguished by frequency separation. For example, in our usual setup for N_2 CARS experiment, ω_{pu} =14830 cm^{-1}, ω_{St} =12500 cm^{-1}, ω_{pr} =12500 cm^{-1}. $E_{pu}^{(+)} \cdot E_{St}^{(-)} \cdot E_{pr}^{(+)}$ and $E_{pu}^{(+)} \cdot E_{St}^{(+)} \cdot E_{pr}^{(-)}$ will result into the same signal frequency at 14830 cm^{-1} while $E_{pu}^{(-)} \cdot E_{St}^{(+)} \cdot E_{pr}^{(+)}$ is associated with coherent Stokes Raman

scattering (CSRS) and $E_{pu}^{(+)} \cdot E_{St}^{(+)} \cdot E_{pr}^{(+)}$ is related to sum frequency generation. To determine if both $E_{pu}^{(+)} \cdot E_{St}^{(-)} \cdot E_{pr}^{(+)}$ and $E_{pu}^{(+)} \cdot E_{St}^{(+)} \cdot E_{pr}^{(-)}$ will contribute to the experimental collected CARS signal we also need to check the phase matching condition.

In Figure 3.4 we showed the positions of three laser pulses on the focusing lens and on the collimating lens. The locations of the two FWM signals $E_{pu}^{(+)} \cdot E_{St}^{(-)} \cdot E_{pr}^{(+)}$ (CARS) and $E_{pu}^{(+)} \cdot E_{St}^{(+)} \cdot E_{pr}^{(-)}$ (CARS*) were also denoted according to the phase matching calculation. It turns out we can spatially separate the major CARS signal generation from the $E_{pu}^{(+)} \cdot E_{St}^{(+)} \cdot E_{pr}^{(-)}$ nonlinear signal. As a result, with the above laser configuration, we need to model CARS signal generation with complex electric field expression $E_{pu}^{(+)} \cdot E_{St}^{(-)} \cdot E_{pr}^{(+)}$ in order not to include extra contributions.

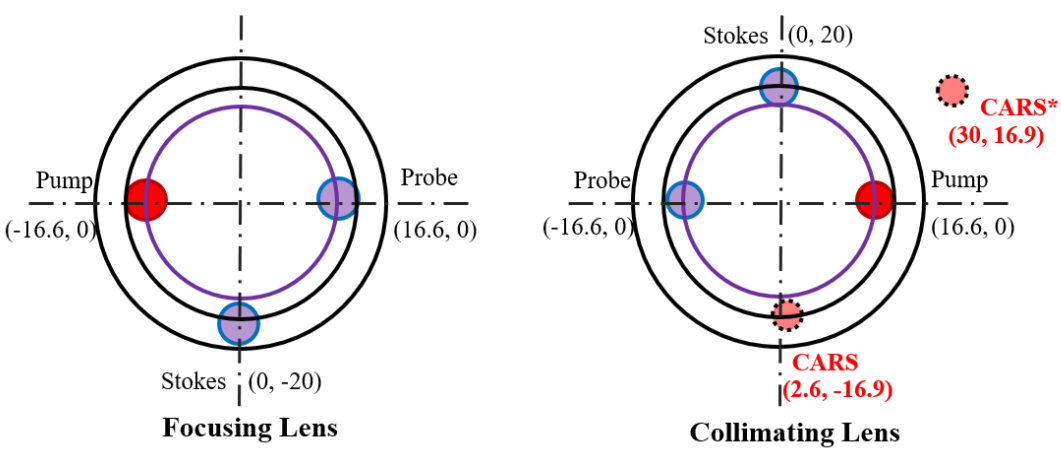

Figure 3.4 Positions of three laser beams and the CARS/CARS* signals on the focusing lens and on the collimating lens. The center frequencies of the three laser beams are ω_{pu} =14830 cm^{-1}, ω_{St} =12500 cm^{-1}, ω_{pr} =12500 cm^{-1}.

Similar analysis can be performed for our previous laser configuration where ω_{pu} =12500 cm^{-1}, ω_{St} =10170 cm^{-1}, ω_{pr} =12500 cm^{-1} . In this setting, the phase matching condition calculation indicates the spatial overlap of the two FWM signals. Thus, in this case, a complex electric field characterization will be needed for accurate CARS signal modelling. As a conclusion, the choices of complex/purely real electric field expression for CARS modelling will rely on the laser

frequencies as well as the phase matching conditions. In the context throughout this thesis, the electric field expression is denoted as complex form unless otherwise specified.

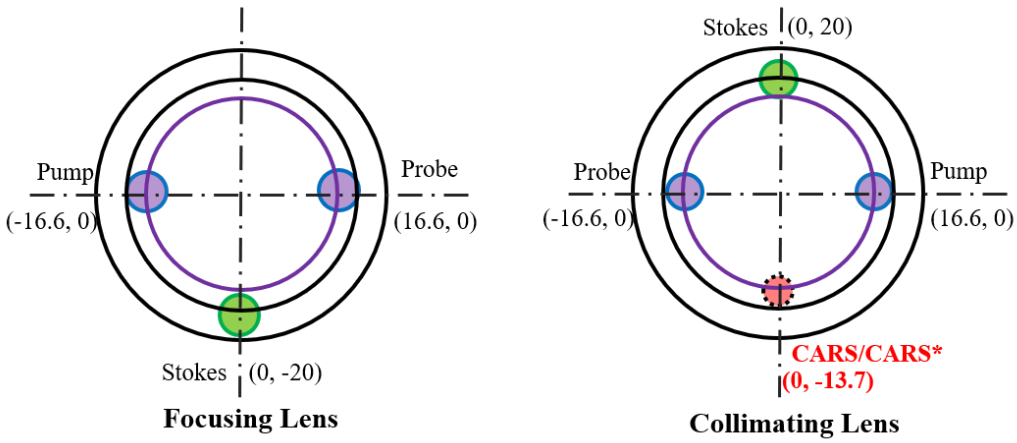

Figure 3.5 Positions of three laser beams and the CARS/CARS* signals on the focusing lens and on the collimating lens. The center frequencies of the three laser beams are ω_{pu} =12500 cm^{-1}, ω_{St} =10170 cm^{-1}, ω_{pr} =12500 cm^{-1}.

3.2.3 Raman Frequency

According to Born-Oppenheimer approximation, the internal energy modes of molecules can be expressed as a summation of separation terms

$$\varepsilon_{int} = \varepsilon_{elec} + \varepsilon_{vib} + \varepsilon_{rot} \tag{2.21}$$

Most gas phase CARS diagnostic techniques involve only the vibrational and rotational transitions. To obtain the analytical expression of the vibrational and rotational energy levels, a derivation from Schrödinger's wave equation (SWE) is usually needed. For a diatomic molecule, the solution of the angular part of the SWE leads to rotational energy level structure.

$$\varepsilon_{rot} = \left[J\left(J+1\right) \right] \hbar^2 / \left(2\mu r_e^{\,2}\right) \tag{2.22}$$

J is the rotational quantum number and can only be non-negative integer. r_e denotes the internuclear spacing, when rigid rotor approximation is applied, it can be considered as a constant. However, when J is large enough the rigid rotor approximation could fail because of the centrifugal stretching force. The rotational energy can thus be written as

$$F_v\left(J\right) = \frac{\varepsilon_{rot}}{hc} = B_v J\left(J+1\right) - D_v J^2 \left(J+1\right)^2 \tag{2.23}$$

The rotational constant B_v and D_v are vibrational level dependent due to the vibration-rotation interactions. One of the key factors of solving SWE for vibrational energy levels is to find an appropriate potential energy function. When harmonic oscillator assumption is made the potential energy function can be written as

$$V(r) = \frac{1}{2}k(r - r_e)^2 \tag{2.24}$$

Where k is the force constant and r_e denotes the equilibrium internuclear distance. Accordingly, the solution of the vibrational energy is quantized and can be written as

$$\varepsilon_{vib} = \left(\mathrm{v} + \frac{1}{2}\right)h\nu_{vib} \tag{2.25}$$

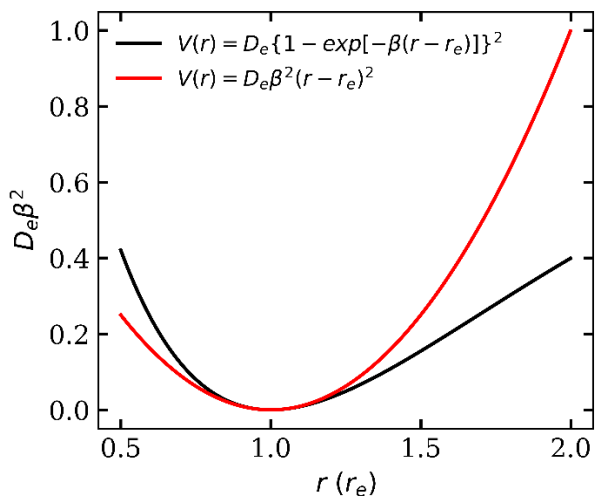

Figure 3.6 Vibrational potential energy function for a Morse potential and a quadratic potential respectively.

v is the vibrational quantum number and can only be non-negative integer. As is shown in Figure 3.6, the harmonic oscillator assumption is appropriate only at small v. A more general potential energy function is the Morse potential function

$$V(r) = D_e\left\{1 - exp\left[-\beta(r - r_e)\right]\right\}^2 \tag{2.26}$$

where D_e is the electronic dissociation energy and shouldn't be confused with the rotational constant as described previously. $\beta = \omega_e \sqrt{\pi c \mu / \hbar D_e}$ is determined by D_e and vibrational constant ω_e. Accordingly, the solution of the Morse energy potential gives the vibrational energy expression as

$$G(\mathrm{v}) = \frac{\varepsilon_{vib}}{hc} = \omega_e \left(\mathrm{v} + \frac{1}{2}\right) - \omega_e x_e \left(\mathrm{v} + \frac{1}{2}\right)^2 + \omega_e y_e \left(\mathrm{v} + \frac{1}{2}\right)^3 - \ldots \tag{2.27}$$

Mostly, the first and second order terms are enough to characterize the vibrational energy accurately. Higher order corrections can be added if necessary. The total ro-vibrational energy is denoted as

$$E(\mathrm{v}, J) = G(v) + F_v(J) \tag{2.28}$$

The selection rule for Raman-active transitions requires that for vibrational transition, $\Delta \mathrm{v}=1$, $\Delta J = 0$ (Q-branch transition). Or for pure rotational transition, $\Delta \mathrm{v}=0$, $\Delta J = +2$ (S-branch) and $\Delta \mathrm{v}=0$, $\Delta J = -2$ (O-branch). For example, the Q-branch transition frequency can thus be calculated as

$$\omega_J = E(v+1, J) - E(v, J) \tag{2.29}$$

3.2.4 Raman Linewidth

The determination of Raman linewidth Γ_i (full width half maximum) usually requires the help of some semi-empirical models. Such models include the well-known modified energy gap law (MEG)[57] and energy-corrected fitting law (ECS)[62]. MEG law is a more advanced version of EGL law and it will be used for collisional linewidth modelling throughout this thesis.

Unless otherwise specified, the Raman linewidth Γ_i is this section only accounts for rotational collision contributions. This is a reasonable assumption for simple diatomic molecules like N_2 and O_2, in our future discussion of CO_2 CARS, we shall see that the vibrational dephasing is no longer negligible and both the vibrational and rotational linewidth will need to be considered. The state-to-state rotational collision rate from rotational state i to rotational state j ($i < j$), according to MEG law, is given as

$$\gamma_{ij} = \alpha p \frac{1-exp(-m)}{1-exp(-mT/T_0)} \left(\frac{T_0}{T}\right)^{0.5} \left(\frac{1+1.5E_i/k_B T\delta}{1+1.5E_i/k_B}\right)^2 exp\left(-\beta\left|\Delta E_{ij}\right|/k_B T\right) \tag{2.30}$$

In Eq.(2.30), p is the pressure, T and T_0 are the real temperature and reference temperature respectively. E_i is the rotational energy of state i and k_B is the Boltzmann constant, ΔE_{ij} is the energy difference between state i and state j. The rest of the parameters are fitting parameters and are determined from experimental measurements. An example of the fitting parameters for N_2 as summarized by Rahn et. al is listed in Table 3.1.

Table 3.1 List of the fitting parameters in the MEG law and the corresponding values for N_2.

Parameter	Value
α	0.0231 $cm^{-1}atm^{-1}$
m	0.1487
δ	1.21
β	1.67
T_0	295

The downward collisional rate can be calculated based on microscopic reversibility at steady state

$$\gamma_{ji} = \gamma_{ij} \frac{g_i}{g_j} exp\left(\Delta E_{ij}/k_B T\right) \tag{2.31}$$

Where g_i and g_j are the rotational degeneracies. The collisional line width Γ_i can be given as (for Q-branch transition)

$$\frac{\Gamma_i}{2} = \sum_{j \neq i} \gamma_{ij} \tag{2.32}$$

At moderately low number densities, Eq.(2.32) and Eq.(2.16) are accurate enough to characterize the collisional effects. At high number densities, collisional line mixing effects become important, the *G*-matrix approach[56] can be used to calculate the CARS spectra.

In frequency domain, CARS spectra can be expressed in *G*-matrix formulation as

$$I(\omega) = c\mathbf{d} \cdot \mathbf{G}^{-1}(\omega) \cdot \mathbf{P} \cdot \mathbf{d}^T \tag{2.33}$$

where c is a constant, $\mathbf{d}$ is a vector denotes the Raman cross section, $\mathbf{P}$ is a diagonal matrix where the diagonal elements representing the Boltzmann population difference between the initial and final rovibrational states. $\mathbf{G}(\omega)$ includes the transition frequency and linewidth information as

$$\mathbf{G}(\omega) = -\omega\mathbf{I} + \mathbf{\Omega_0} + i\mathbf{\Gamma} \tag{2.34}$$

where $\mathbf{I}$ is the identity matrix, $\mathbf{\Omega_0}$ is the diagonal matrix of transition frequencies and $\mathbf{\Gamma}$ is the collisional relaxation matrix. With MEG law, the off diagonal matrix elements of $\mathbf{\Gamma}$ are given according to Eq. (2.30) and Eq. (2.31), and the diagonal matrix elements are given according to Eq. (2.32). At moderately low number densities, the off diagonal elements of $\mathbf{\Gamma}$ are negligible small and can be approximated to zero. The inverse Fourier transform of the diagonal matrix $\mathbf{G}^{-1}(\omega)$ is straightforward, and can give a time domain expression of Raman susceptibility in a form of

$$\int_{-\infty}^{+\infty} \mathbf{G}^{-1}(\omega) e^{-i\omega t} d\omega \propto \sum_j exp\left(-i\omega_{0,j} + \Gamma_j\right)t \tag{2.35}$$

The transition frequency and linewidth in Eq. (2.35) are consistent as in Eq. (2.16). For higher number densities, a full matrix inversion $\mathbf{G}^{-1}(\omega)$ is required. Notice that if we can diagonalize $\mathbf{G}(\omega)$, the inversion of the diagonal matrix will then become convenient. More importantly, the inverse Fourier transform of the diagonal matrix will give us an expression similar to Eq. (2.35). The following derivation of matrix operation follows the work by Koszykowski et. al.[56]. $\mathbf{G}(\omega)$ can be decomposed as

$$\mathbf{G}(\omega) = -\omega\mathbf{I} + \mathbf{K} \tag{2.36}$$

$$\mathbf{K} = \mathbf{\Omega}_0 + i\mathbf{\Gamma} \tag{2.37}$$

The square matrix $\mathbf{A}$ that can diagonalize $\mathbf{G}$ can also diagonalize $\mathbf{K}$ since that $-\omega\mathbf{I}$ is already a diagonal matrix.

$$\mathbf{A}^{-1}\mathbf{G}(\omega)\mathbf{A} = -\omega\mathbf{I} + \mathbf{D}_K \tag{2.38}$$

$\mathbf{D}_K$ is the diagonal matrix that is composed of the eigenvalues λ_k of $\mathbf{K}$. Accordingly, we can have the inverse of Eq.(2.38) as

$$\mathbf{A}^{-1}\mathbf{G}^{-1}(\omega)\mathbf{A} = \left[-\omega\mathbf{I} + \mathbf{D}_K\right]^{-1} = \mathbf{D}^{-1} \tag{2.39}$$

Substitute Eq.(2.39) into Eq.(2.33) we can have

$$I(\omega) = c(\mathbf{d}\cdot\mathbf{A})\cdot\mathbf{D}^{-1}(\omega)\cdot\left(\mathbf{A}^{-1}\cdot\mathbf{P}\cdot\mathbf{d}^{T}\right) \tag{2.40}$$

The inverse Fourier transform of $\mathbf{D}^{-1}(\omega)$ can still be written in a way similar to Eq. (2.35) as

$$\int_{-\infty}^{+\infty}\mathbf{D}^{-1}(\omega)e^{-i\omega t}d\omega \propto \sum_{j} exp\left(-i\tilde{\omega}_{0,j}+\tilde{\Gamma}_{j}\right)t \tag{2.41}$$

where the transition frequency $\tilde{\omega}_{0,j}$ and the collisional linewidth $\tilde{\Gamma}_{j}$ now are as a result of the collisional line mixing effects. And from Eq.(2.40) it is obvious that the transition strength is also modified because of the collisional line mixing effects. Eq. (2.40) can be written as a summation of each individual transition as

$$I(\omega) = \pi^{-1}\,\mathrm{Re}\sum_{j} -i\frac{p_j + iq_j}{(\tilde{\omega}_{0,j}-\omega)-i\tilde{\gamma}_{jj}} \tag{2.42}$$

Where $p_j + iq_j$ denote the complex intensity factor as can be determined from

$$p_j + iq_j = (\mathbf{d}\cdot\mathbf{A})_j\cdot\left(\mathbf{A}^{-1}\cdot\mathbf{P}\cdot\mathbf{d}^{T}\right)_j \tag{2.43}$$

Eq. (2.42) can also be written as a Lorenzian and dispersive contribution of CARS intensity as

$$I(\omega) = \pi^{-1}\sum_{j}\frac{p_j\tilde{\gamma}_{jj}}{(\tilde{\omega}_{0,j}-\omega)^2+\tilde{\gamma}_{jj}^{\,2}} + \pi^{-1}\sum_{j}\frac{q_j(\tilde{\omega}_{0,j}-\omega)}{(\tilde{\omega}_{0,j}-\omega)^2+\tilde{\gamma}_{jj}^{\,2}} \tag{2.44}$$

In Figure 3.7, we showed the simulated N_2 ns CARS spectra with and without the correction of collisional line mixing. Obviously, the collisional line mixing effects become more significant at higher pressures. For most atmospheric pressure studies, the number density is low, and the well separated transitions assumption is reasonable.

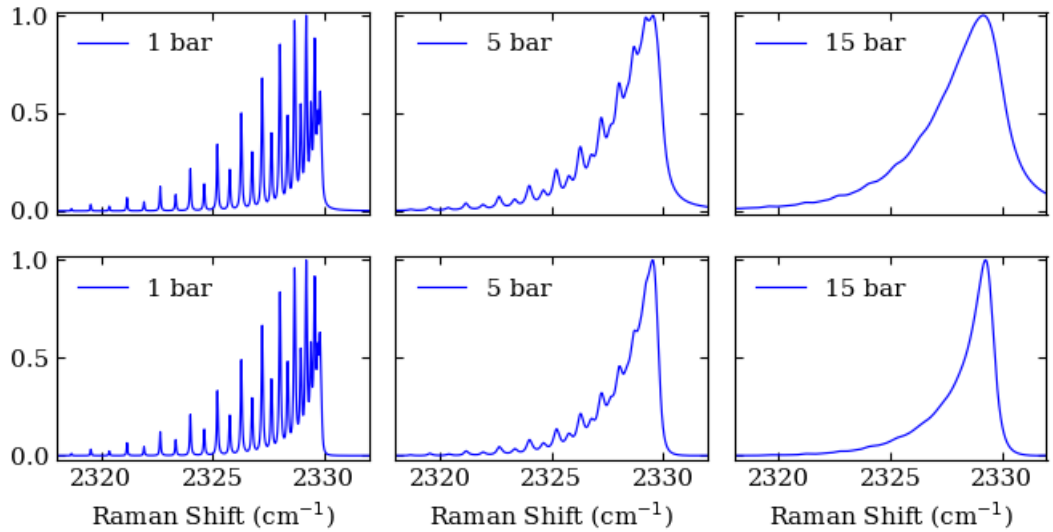

Figure 3.7. Simulated room temperature N_2 ns CARS spectra at 1, 5 and 15 bars. The first and second column show the cases without and with considering collisional line mixing effects separately.

For fs CARS, the effects of collisional narrowing on the CARS spectra can become less significant than ns CARS because the shorter laser-matter interaction timescale.

3.2.5 Raman Transition Strength

According to Eq.(2.16), the Raman transition strength is determined by $\Delta N\left(d\sigma / d\Omega\right) f$. The population difference (relative population) can usually be calculated through Boltzmann population distribution.

$$\Delta N = g_i \, exp\left(-\varepsilon_i / k_B T\right) - g_j \, exp\left(-\varepsilon_j / k_B T\right) \tag{2.45}$$

In general, g_i and g_j in Eq.(2.45) denote the overall degeneracy which include the nuclear, electronic, vibrational, rotational and translational degeneracies. Most of them can be cancelled when they are in the same state. For example, for CARS transition that within the same electronic level, Eq.(2.45) can be written as

$$\Delta N = g_{\mathrm{vi}} g_{ni} g_{Ji} \, exp\left(-\varepsilon_i / k_B T\right) - g_{\mathrm{vj}} g_{nj} g_{Jj} \, exp\left(-\varepsilon_j / k_B T\right) \tag{2.46}$$

Where g_{v}, g_n and g_J are the vibrational, nuclear and rotational degeneracies respectively. For simple diatomic molecules $g_{\mathrm{v}}=1$, $g_J=2J+1$. The determination of nuclear degeneracy needs to consider the symmetric property of the particle wave function with respect to parity operation.

For example, for diatomic molecules like N_2, the ground electronic level ${}^1\Sigma_g^+$ is symmetric, the nuclear spin statistics weight (NSSW) give

$$g_0=2I+1 \tag{2.47}$$

$$g_n=\frac{g_0\left(g_0-1\right)}{2},\left(J=1,3,5,...\right) \tag{2.48}$$

$$g_n=\frac{g_0\left(g_0+1\right)}{2},\left(J=0,2,4,...\right) \tag{2.49}$$

Where I is the nuclear spin. For N_2, $I=1$, $g_0=3$. For O_2, the ground electronic level ${}^3\Sigma_g^-$ is antisymmetric, thus

$$g_n=\frac{g_0\left(g_0+1\right)}{2},\left(J=1,3,5,...\right) \tag{2.50}$$

$$g_n=\frac{g_0\left(g_0-1\right)}{2},\left(J=0,2,4,...\right) \tag{2.51}$$

Similarly, the nuclear spin of O_2 is $I=0$, $g_0=1$. Notice also the above discussion is valid only for diatomic molecules. For polyatomic molecules like CO_2 and CH_4, the calculation of rovibrational degeneracies are usually more complex, some literatures have discussed them in more details using group theory[123], an alternative option is to use some well-tabulated database[96].

Raman cross section for Q-branch transitions can be given as

$$\frac{\partial\sigma}{\partial\Omega}\propto\left(\mathrm{v}+1\right)\left[\left(a'\right)^2+\frac{4}{45}b_{J,J}\left(\gamma'\right)^2\right] \tag{2.52}$$

v is the vibrational quantum number, $\left(a'\right)^2$ and $\left(\gamma'\right)^2$ are the isotropic and anisotropic invariants of the polarizability tensor and they can be found in literature[124]. $b_{J,J}$ is the Placzek-Teller coefficient and is given as

$$b_{J,J}=\frac{J\left(J+1\right)}{\left(2J-1\right)\left(2J+3\right)} \tag{2.53}$$

Herman-Wallis (HW) correction factor is used to correct the Raman transition line strength as calculated from rigid rotor approximation. The HW factor used in this work is from Tipping and Bouanich's work[125].

$$f = 1 - \left[3\left(a_1 + 1\right)/2 - 4\left(p_2 / p_1\right)\right]^2 \gamma^2 J\left(J+1\right) \tag{2.54}$$

a_1 is the first Dunham coefficient that accounts for the anharmonicity of the internuclear potential, p_1 and p_2 are the coefficients of the isotropic polarizability expansion, and $\gamma = 2B_e / \omega_e$ denotes the rovibrational coupling strength through dividing the rotational constant to the vibrational frequency. The influence of HW factors are generally more significant in small molecules because the much greater rotational constant. Marrocco has summarized the parameters in Eq. (2.54) for several diatomic molecules that are typical for CARS diagnostics[126].

3.3 Density Matrix Formulation

3.3.1 Time-dependent Density Matrix Equations

Time dependent density matrix equations (TDDM) are important in terms of revealing the fundamental physics for N_2 fs CARS. The theoretical framework was based on the work by Lucht et. al [127]. The theoretical modelling of TDDM is further developed in this work from two aspects: (1) the numerical code has been modified to enable for parallelized computation and the numerical efficiency has been significantly improved; and (2) state to state population and coherence transfer have been enabled, and the rotational collisional rates are evaluated according to modified energy gap (MEG).

The general structure of the nitrogen Q-branch model is depicted in Figure 3.8. In the development of the density matrix equations, energy levels will be designated using upper case letters, and quantum states will be designated using lower case letters. Levels *G* and *E* are specific rotational levels in the vibrational levels in the $X\,^1\Sigma_g^+$ ground electronic level of N_2; the lower case letters *g* and *e* will be used to designate Zeeman states in levels *G* and *E*, respectively. For Q-branch transitions, the rotational quantum numbers for levels *G* and *E* are equal $J_G = J_E$, and the vibrational quantum numbers are related by $\mathrm{v}_E = \mathrm{v}_G + 1$. An effective (fictitious) electronic level with character is defined as the intermediate level for the Q-branch Raman transitions.

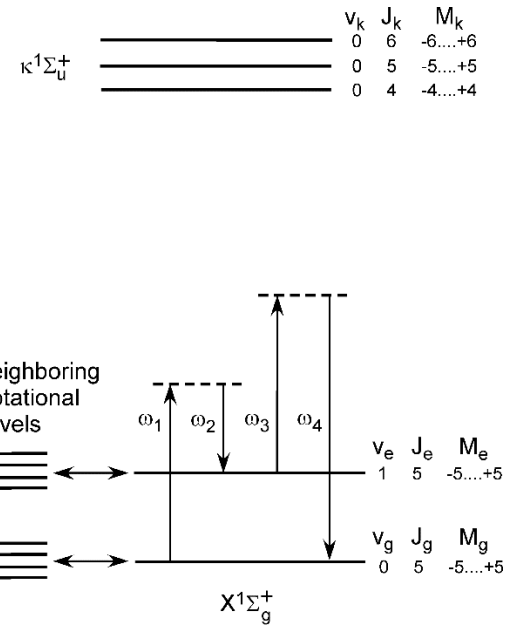

Figure 3.8. Schematic diagram of the energy level structure for the femtosecond CARS calculation of the Q(5) transition in the fundamental (1,0) Raman band of the nitrogen molecule.

The time-dependent density matrix equations for the ground states *g* and excited state *e* populations, and the coherence between states *g* and *e* can be given as

$$\frac{\partial \rho_{ee}}{\partial t} = -\Gamma_e \rho_{ee} + \sum_{e'} \Gamma_{e'e} \rho_{e'e'} - \frac{i}{\hbar} \sum_m \left(V_{em} \rho_{me} - \rho_{em} V_{me} \right) \tag{2.55}$$

$$\frac{\partial \rho_{gg}}{\partial t} = -\Gamma_g \rho_{gg} + \sum_{g'} \Gamma_{g'g} \rho_{g'g'} - \frac{i}{\hbar} \sum_m \left(V_{gm} \rho_{mg} - \rho_{gm} V_{mg} \right) \tag{2.56}$$

$$\frac{\partial \rho_{eg}}{\partial t} = -\partial \rho_{eg} \left(i\omega_{eg} + \gamma_{eg} \right) + \sum_{g'} \Gamma_{g'g} \rho_{e'g'} - \frac{i}{\hbar} \sum_m \left(V_{em} \rho_{mg} - \rho_{em} V_{mg} \right) \tag{2.57}$$

In Eqs.(2.55), (2.56) and (2.57), ω_{eg} is the transition frequency between state *e* and *g*, and pumping terms such as V_{em} are used to model the laser matter interaction through the driving electric field.

$$V_{ek} = -\hat{\mu}_{ek} \cdot \hat{E}\left(r,t\right) \tag{2.58}$$

In Eq. (2.58) $\hat{\mu}_{ek}$ is the dipole moment of the single photon coupling states *e* and *k* transition

Relaxation terms like $\Gamma_{e'e} / \Gamma_{g'g}$ denote the rotational relaxation rate from state g'/e' to state g/e, while Γ_e / Γ_g is the total population transfer rate out of quantum state *e*/*g*. For gaseous N_2, the rates of vibrational inelastic collisions and pure dephasing collisions are usually negligible as

compared to rotational inelastic collisions. The total population transfer rate out of state g is given by

$$\Gamma_g = \sum_g \Gamma_{gg'} \tag{2.59}$$

The dephasing rate for the eg coherence is given by

$$\gamma_{eg} = \frac{1}{2}\left(\Gamma_e + \Gamma_g\right) + \gamma_{vib} \approx \frac{1}{2}\left(\Gamma_e + \Gamma_g\right) \tag{2.60}$$

The downward state to state transition rate is given according to MEG law as consistent in Eq.(2.30)

In Eqs.(2.55), Eq.(2.56) and Eq.(2.57), calculations of population elements in different rotational levels as well as the calculations of coherence elements in different Q branch transitions are correlated through rotational relaxations, for example, through terms like $\sum_{e'} \Gamma_{e'e}\rho_{e'e'}$, $\sum_{g'} \Gamma_{g'g}\rho_{g'g'}$ and $\sum_{g'} \Gamma_{g'g}\rho_{e'g'}$. Those terms will be of greater significance for high gas number density conditions and can be neglected for most of the atmospheric pressure calculations. Thus, for low gas number density conditions, Eq. (2.55) to Eq.(2.57) can be further reduced as

$$\frac{\partial \rho_{ee}}{\partial t} = -\Gamma_e \rho_{ee} - \frac{i}{\hbar}\sum_m \left(V_{em}\rho_{me} - \rho_{em}V_{me}\right) \tag{2.61}$$

$$\frac{\partial \rho_{gg}}{\partial t} = -\Gamma_g \rho_{gg} - \frac{i}{\hbar}\sum_m \left(V_{gm}\rho_{mg} - \rho_{gm}V_{mg}\right) \tag{2.62}$$

$$\frac{\partial \rho_{eg}}{\partial t} = -\partial \rho_{eg}\left(i\omega_{eg} + \gamma_{eg}\right) - \frac{i}{\hbar}\sum_m \left(V_{em}\rho_{mg} - \rho_{em}V_{mg}\right) \tag{2.63}$$

With extra information for the pump, Stokes and probe laser electric field characterization, a full set of density matrix equations can be constructed and solved through direct numerical integration (DNI). The time resolved resonant and non-resonant polarizations of the CARS signal are given by [127]

$$P_{res}(t) = \left(\hat{e}_4 \cdot \boldsymbol{\mu}_{gk}\right)\eta_{kg}(t) \tag{2.64}$$

$$P_{nres}(t) = \beta\chi_{NR}E_{pu}(t)E_{St}^{*}(t)E_{pr}(t) \tag{2.65}$$

In Eq. (2.64) density matrix element η_{kg} denotes the Raman coherence between fictitious electronic state k and ground vibrational state g, $\hat{e}_4$ is the unit directional vector dictated by phase

matching condition. Non-resonant response is the instantaneous product between the pump, Stokes and prove electric fields, χ_{NR} denotes the non-resonant susceptibility and β is simply a scaling parameter.

3.3.2 Numerical Aspects

The numerical code was originally written in Fortran 90 (PGI compiler) and has recently been rewritten in Python 2.7. Thanks to some numerically efficient modules from Python packages such as numpy and scipy, the rewritten code has comparable numerical efficiency compared to the original code even without further parallelization. First, we consider fs CARS calculations for near-atmospheric pressures where the population and coherence transfer among different rotational levels can be neglected. For this case, the calculations of density matrix elements among different Q-branch transitions are according to Eq.(2.61) to Eq.(2.63) and are independent of each other. Multiple Q-branch transitions can thus be assigned to one computational thread and a parallelized scheme can then be constructed in a way as shown in Figure 3.9.

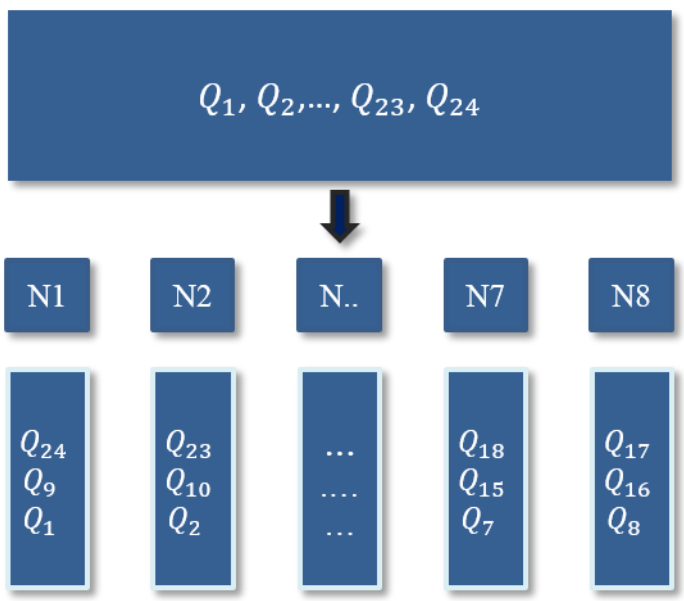

Figure 3.9. Numerical scheme for the parallelization. Thread communication is disabled, 24 Q-branch transitions and 8 computational threads are considered.

Load balancing strategies need to be considered when Q-branch transitions outnumber the available computational threads (which is usually the case). Also notice that for a specific transition with rotational quantum number J, the number of Zeeman states is $2J+1$, and the corresponding

density matrix size is $(2J+1)^2$. This implies that the computational cost scales with J, and correspondingly the CPU time is shown in Figure 3.10.

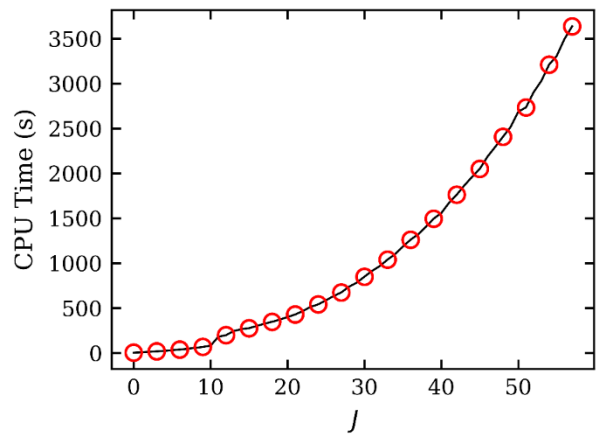

Figure 3.10. CPU time for computing all the density matrix elements within a Q-branch transition as compared to the rotational quantum number J for that transition. CPU time for 60 rotational levels are compared.

In general, the CPU time has an approximately quadratic dependence about the rotational quantum number. In such case, the problem can be generalized as following: Allocate a list of jobs $\{ Q_1, Q_2, \ldots, Q_n \}$ into k computational threads to enable optimum load balancing. This is a k partitioning problem and it is NP hard [128]. One simple strategy is called the first-fit decreasing algorithm:

1. Sort $\{ Q_1, Q_2, \ldots, Q_N \}$ in descending order in terms of load
2. Distribute the first k jobs across the k subgroups
3. Iterate over the remaining n-k tasks. Add each number into the subgroup that currently has the lowest sum.

By doing this we minimize idle time when multiple computational threads are being called. The overall CPU time as compared to the number of threads being called is shown in Figure 3.11.

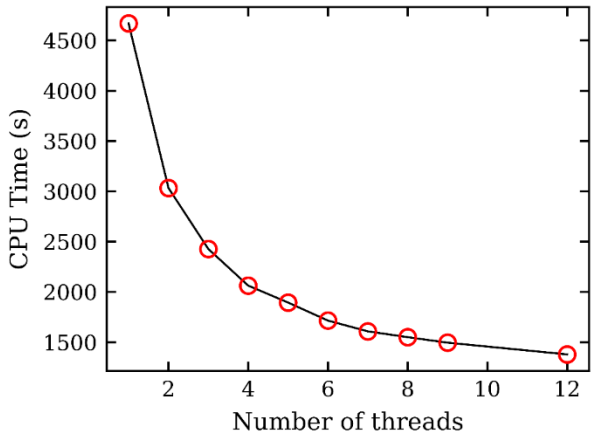

Figure 3.11. Computational time as compared to the number of threads being called in the parallelized code, 24 Q-branch transitions are included.

The CPU time speeds up by a factor of 3 when 6 threads are being called. The improvement of numerical efficiency is obvious, further advancement is mainly limited by the physical number of computational cores available and by the computational time needed for high J level Q-branch transitions.

For high pressure simulations where collisional induced population and coherence transfer are no longer negligible, each Q-branch transition calculation can only be assigned to one computer thread so that thread communication shall be enabled. Because of nuclear spin statistics, only rotational levels with rotational quantum number differences of $\Delta J = \pm 2, \pm 4, \pm 6...$ can have population and coherence transfer between each other. The numerical scheme for the parallelized code is shown in Figure 3.12.

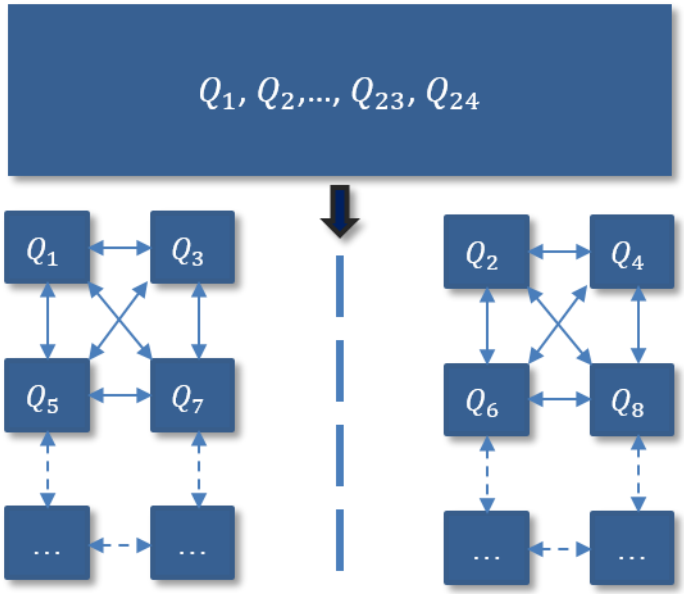

Figure 3.12. Numerical scheme for the parallelization. Thread communication is enabled, 24 Q-branch transitions and 8 computational threads are considered.

3.3.3 Simulations Results

In this simulation, N_2 ns CARS spectrum is generated at room temperature and at 1 bar and 10 bar pressures. To reduce the computational load while ensuring the accuracy, Q-branch transitions from Q(1) to Q(15) transition were included and a 0.02 cm^{-1} pump frequency detuning was set for every iteration. The simulated results are summarized in Figure 3.13 and Figure 3.14 respectively. At atmospheric pressure, when RET is not significant, there is no difference between the simulated CARS spectra with and without implementing the thread communication. At elevated pressure, the RET starts becoming important, the collisional narrowing effect is obvious when thread communication is enabled. The findings are consistent with our previous simulated ns CARS spectrum by using *G*-matrix method.

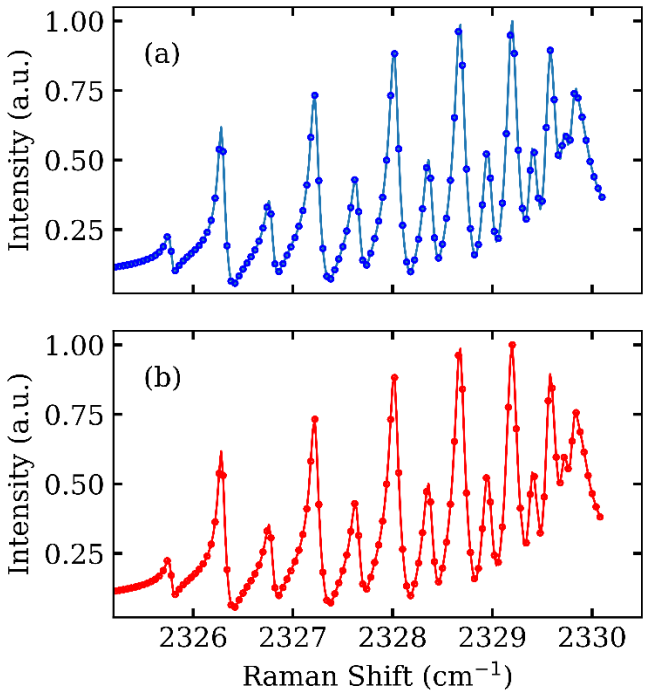

Figure 3.13 Simulated N_2 ns CARS spectrum by assuming (a) no thread communication and (b) with thread communication in the TDDM code. The simulated condition is at 1 bar and 298 K.

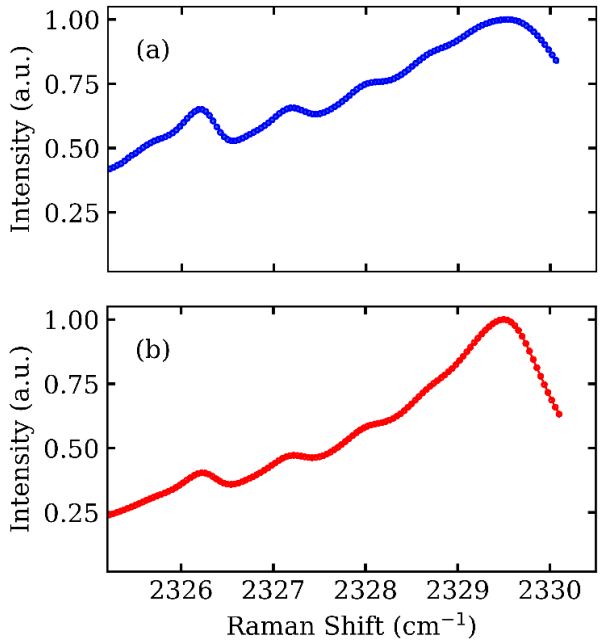

Figure 3.14 Simulated N_2 ns CARS spectrum by assuming (a) no thread communication and (b) with thread communication in the TDDM code. The simulated condition is at 10 bar and 298 K.

In conclusion, the proposed numerical schemes will be applied to solve the TDDM equations as discussed in previous section. The physical insights provided by the TDDM calculations, both for efficient atmospheric pressure calculations and for high pressure simulations will benefit our future experimental studies.

CHAPTER 4. EXPERIMENTAL SYSTEM

Schematic diagram of the experimental system is shown in Figure 4.1, this setup is specifically for N_2 vibrational CARS. However, the tuning range of the optical parametric amplifier (OPA) is from 230 nm to 10 μm, only a few changes need to be made in terms of optical alignment to investigate rovibrational transitions for other species. The detailed descriptions of the experimental system are given in the following sections.

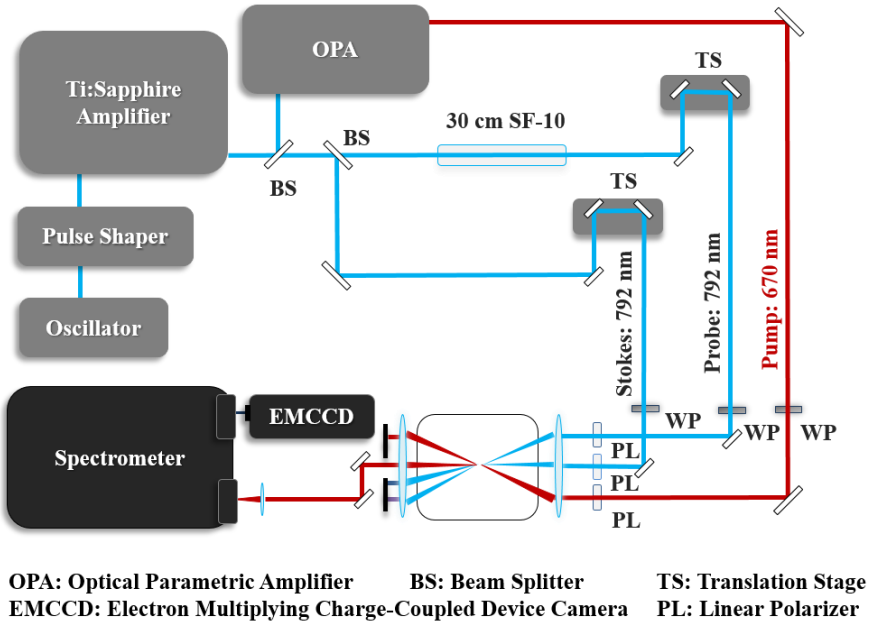

Figure 4.1 Schematic diagram of the experimental system

4.1 Laser System

The process of the femtosecond pulse generation for the experiment is as shown in Figure 4.2.

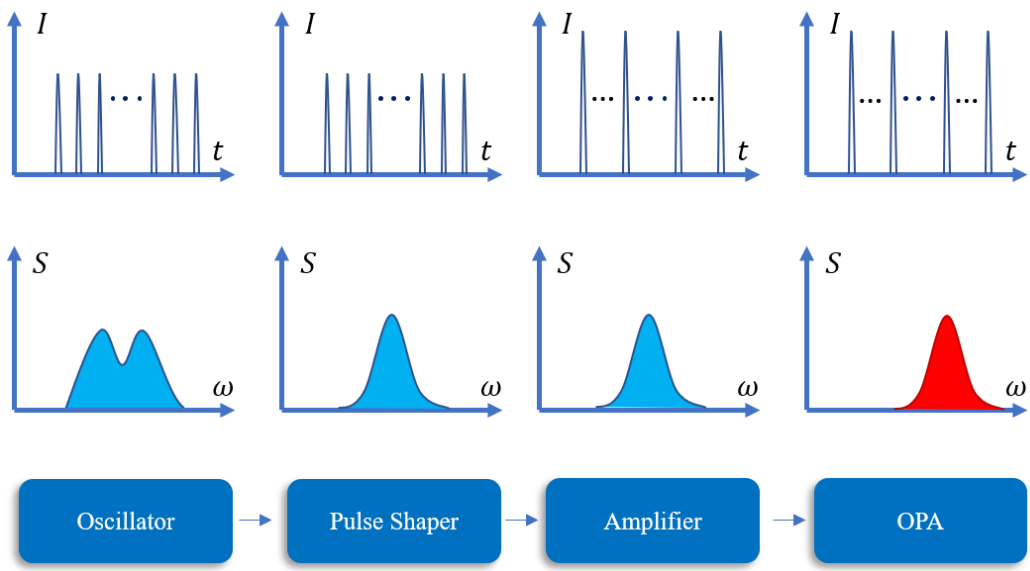

Figure 4.2 Overall process of the femtosecond pulse generation in the laser system.

The seed femtosecond pulse is generated from a passively mode-locked Titanium:Sappire (Ti:S) oscillator (Coherent Mantis^{TM}) with a repetition rate of 80085 kHz. With the internal diode laser pumping, the Ti:Sapphire crystal itself will amplify in the frequency range from 680 nm to 1100 nm. This broadband amplification will be restricted by the optics inside the oscillator. As a consequence, the spectral bandwidth of the Mantis output is around 68 nm and a typical Mantis output pulse spectrum is as shown in Figure 4.3. The output energy directly from Mantis is 6 nJ per pulse, this energy is too weak for OPA to operate normally and for gas phase CARS signal generation, thus a laser amplifier is added in the laser system. However, the bandwidth Mantis output pulse is still too much for the downstream amplifier, the spectral profile is also not like Gaussian or Lorentzian and they will be favored for optimal OPA performance. A pulse shaper is added in between the oscillator and the amplifier to tailor the spectral profile of the seed pulse.

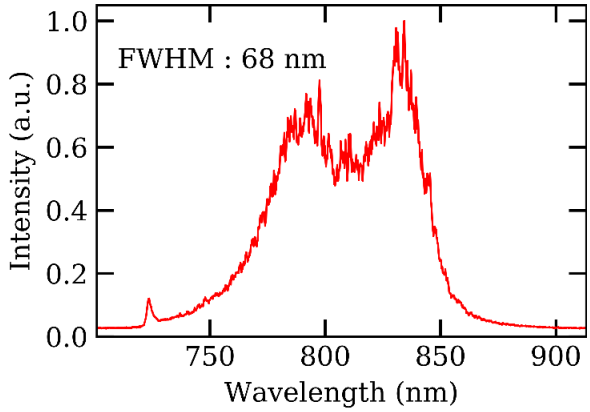

Figure 4.3. Typical power spectrum of the Mantis output pulse.

The 4-f pulse shaper (Femtojock, Biophotonic, Inc), depicted schematically in Figure 4.4, enables programmable amplitude and spectral phase modulation onto the input pulse. In general, different frequency components of the input pulse will first be spatially dispersed through a grating and then collimated by a focusing lens; as those frequency components fall into the spatial light modulation (SLM) units at corresponding locations, transmissivity and the index of the refractivity of the SLM unites can then be varied by controlling the voltages. The modulated light will then be re-collimated and combined by using a symmetric lens and grating setup. The use of the pulse shaper after the oscillator helps to remove the unwanted frequency components and ensures a transform-limited pulse into the main amplifier. Typical optical spectrum of the pulse shaper output is shown in Figure 4.5. Compared to the optical spectrum shown in Figure 4.3, the optical spectrum after the pulse shaper has a more Gaussian-like profile and the spectral bandwidth is significantly narrowed.

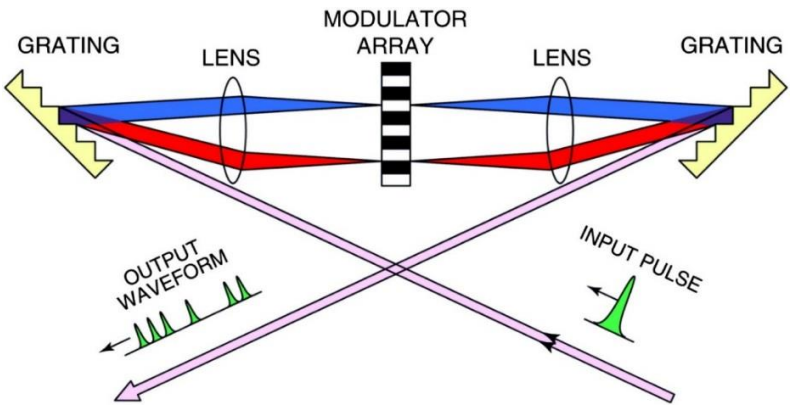

Figure 4.4. Schematic drawing of a typical 4-f pulse shaper, the drawing is from literature [129]

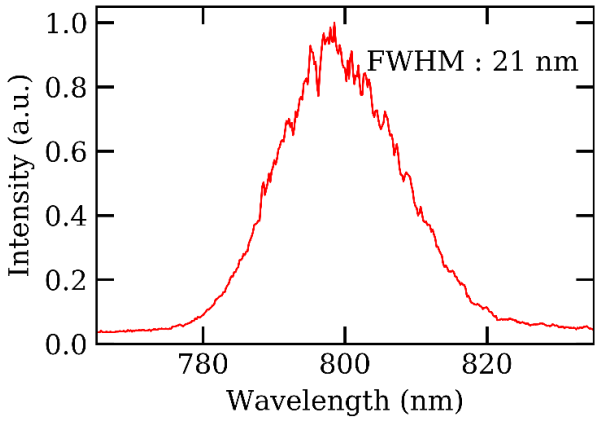

Figure 4.5. Typical power spectrum of the 4-f pulse shaper output pulse.

The femtosecond pulse is amplified from 6 nJ per pulse to about 2 mJ inside the laser amplifier (Legend Elite Duo, Coherent Inc). The femtosecond pulse amplification is achieved through chirped pulse amplification (CPA). I.e., the pulse is first being extensively frequency chirped in the stretcher. The implementation of CPA is critical for laser amplifier because different frequency components are amplified sequentially inside the gain medium and the amplified pulse remains below the crystal damage threshold. The chirped pulse then passes through the regenerative amplifier which is pumped by the 70 W Evolution pump laser. There are in general two amplification stages: a single pass amplifier (SPA) and a regenerative amplifier (RGA). Within the RGA, pockel cells and thin film polarizers are used to select and then amplify only 1/16000 out of the pulses through polarization control. This results in a 5 kHz laser repetition rate for the entire

laser system. Switching to a 10 kHz system is also possible by changing the pockel cell setting, however, the resulting pulse energy will be lower than the 5 kHz system and might affect the OPA performance. The amplified laser pulse is finally frequency recombined to form a near Fourier-transform limited (FTL) femtosecond pulse in the compressor. A typical optical power spectrum of the 5kHz Legend output is shown in Figure 4.6. Comparing to the laser spectral profile right after the pulse shaper, the slight spectral broadening and shift are due to the intuitive gain medium properties.

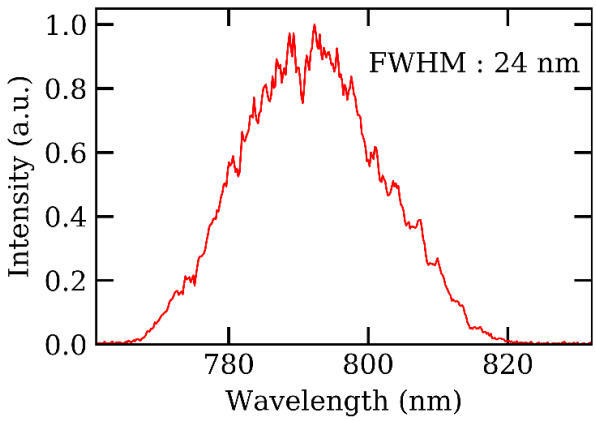

Figure 4.6. Typical power spectrum of the Legend output pulse.

N_2 vibrational CARS requires frequency detuning between the pump and Stokes pulses of about 2330 cm^{-1}. This is far beyond the spectral bandwidth within the 800 nm Legend output and thus a second frequency generation process is required. In our experimental system, the generation of this second beam is realized by using optical parametric amplification (OPA, OperA-Solo, Light Conversion). The basic arrangement inside the OPA includes a pre-amplification stage and a second-amplification stage. In the pre-amplification stage, a small portion of the input 800 nm pulse is used to pump a sapphire plate to generate white-light continuum (WLC). A specific frequency range of the WLC is then interacted with the 800 nm pump pulse inside a nonlinear crystal and gets amplified in the pre-amplification stage (called the signal). The signal beam then gets further strengthen in the second amplification stage with most of the 800 nm pump pulse. Along with the signal beam being amplified, an idler beam is also generated in the second amplification stage which can also be used if needed. However, the frequency tuning range of this basic setting is

limited from 1140 nm to 1640 nm for the signal beam and from 1554 nm to 2660 nm for the idler beam. To extend the frequency tuning range, several extra crystals were installed to enable other nonlinear optical interactions such as second-harmonic generation of signal/idler (SHS/SHI), sum frequency generation between the signal/idler and the pump beam (SFS/SFI) etc. A list of the tuning configuration is shown in Table 4.1.

Table 4.1 The wavelength tuning range of the corresponding laser power of the OPA

Interaction	Wavelength Range (nm) Low	High	Typical Energy
S	1140	1640	0.28 mJ @ 1300 nm
I	1554	2660	0.19 mJ @ 1680 nm
SHS	570	840	0.16 mJ @ 650 nm
SHI	781	1180	0.1 mJ @ 840 nm
SFS	470	533	0.2 mJ @ 500 nm
SFI	528	600	0.2 mJ @ 570 nm
FHS	285	402	40 μJ @ 330nm
FHI	397	485	40 μJ @ 420 nm
SH-SFS	235	266	40 μJ @ 250 nm
SH-SFI	265	295	60 μJ @ 285 nm
DFG1	2500	4900	24 μJ @ 3500 nm
DFG2	3500	18000	20 μJ @ 5000 nm

For most of the rovibrational CARS measurements performed in this work, SHS and SHI are the configurations that were used most often to obtain the frequency range of interest.

The optimal performance of OPA requires a good spatial and temporal profile of the input 800 nm pulse. Usually, a FTL input pulse can significantly increase the WLC generation efficiency as well as the pumping efficiency in the amplification stages because of the higher peak intensity. To ensure the Legend output pulse is as close to FTL as possible, a MIIPS (Multiphoton Intrapulse Interface Scan) system is set right after the Legend output to monitor the pulse spectral profile. The MIIPS system is also connected to the pulse shaper so that a feedback loop can be established, and spectral phase correction can be added to eliminate the unwanted frequency chirp.

A brief introduction to the MIIPS system is given here. MIIPS is essentially based on the relation of nonlinear optical process and the spectral phase content. Among all possible nonlinear optical processes that could be applied in MIIPS, second harmonic generation (SHG) process is mostly

widely adopted. Because SHG can be obtained using a single beam geometry, the theoretical modeling for SHG-MIIPS can also get much simplified.

Consider, an arbitrary electric field function in frequency domain as

$$E(\omega) = |E(\omega)| \cdot e^{j\Psi(\omega)} \tag{3.1}$$

Without the consideration of intermediate resonance, SHG signal intensity can be given as the electric filed convolution inside the pulse with frequency sum as

$$S_{SHG}(2\omega_s) \propto \left| \int |E(\omega_s - \omega)| |E(\omega_s + \omega)| e^{j[\Psi(\omega_s - \omega) + \Psi(\omega_s + \omega)]} d\omega \right|^2 \tag{3.2}$$

While the amplitude integration is somehow fixed once the input field is specified. The SHG signal intensity is dependent only on the spectral phase term.

Obviously, the SHG signal has its maximum when the input pulses are transform-limited because it has least extent of oscillations.

In more general consequence, we can write the spectral phase term in its form of Taylor expansions.

$$\Psi(\omega_s + \omega) = \Psi(\omega_s) + \Psi'(\omega)_{\omega=\omega_s} \cdot \omega + \frac{\Psi''(\omega)_{\omega=\omega_s}}{2!} \cdot \omega^2 + \ldots + (+1)^{n-1} \frac{\Psi^n(\omega)_{\omega=\omega_s}}{n!} \cdot \omega^n \tag{3.3}$$

$$\Psi(\omega_s - \omega) = \Psi(\omega_s) - \Psi'(\omega)_{\omega=\omega_s} \cdot \omega + \frac{\Psi''(\omega)_{\omega=\omega_s}}{2!} \cdot \omega^2 + \ldots + (-1)^{n-1} \frac{\Psi^n(\omega)_{\omega=\omega_s}}{n!} \cdot \omega^n \tag{3.4}$$

The odd spectral phase terms cancel out intuitively. Leaving only the even order phase affecting the general outcome of SHG. In order to obtain maximum SHG signal, now we introduce a compensating phase function f to cancel out all the even order spectral phase components as well.

$$\Psi^{(2n)}(\omega) + f^{(2n)}(\omega) = 0 \tag{3.5}$$

Practically, in most ultrafast optics studies where the quadratic phase term is of primary concern, we can reduce our zero-phase condition as

$$\Psi''(\omega) + f''(\omega) = 0 \tag{3.6}$$

The form of compensating function f can vary a lot, one basic criterion is to introduce as least parameters as necessary to characterize the phase. In many MIIPS studies, f is given as sinusoidal function (though not necessary), so that we can have the following relation as

$$f(\omega) = \alpha \cos(\gamma\omega - \delta) \tag{3.7}$$

$$\Psi''(\omega) = \alpha\gamma^2 \cos(\gamma\omega - \delta) \tag{3.8}$$

α denotes maximum phase shift, γ is the modulation period and δ is a scanning parameter which is used to find the maximum SHG signal intensity. Maximum phase retardation α is always limited by the instrument, too large or too small value of α will all have side effect to MIIPS measurement (e.g. too large α value might cause steep phase modulation, while small α won't be able to compensate large phase distortion.). γ is given such that the periodic phase function should last at least one period across the spectral bandwidth of the pulse. The fact that the maximum allowable phase compensation should be larger or at least comparable to the actual phase distortion indicates that $\left|\alpha\gamma^2\right| \geq \Psi''_{max,est}$, alternatively spectral phase wrapping will be needed, which in some cases could lead to degradation of MIIPS accuracy[130]. From practical considerations to construct MIIPS trace, we can also write the reference phase function as

$$f = f(\omega,\delta) \tag{3.9}$$

For each ω within the spectral region of interest , δ is scanned from 0 to nπ , and the corresponding SHG signal is recorded. Accordingly, a two-dimensional (mapped on ω and δ) MIIPS can then be constructed. By looking for the maximum SHG signal in MIIPS trace, the local spectral phase can be retrieved by performing double integration of $f''(\omega,\delta_{max}(\omega))$, the spectral phase of the entire pulse could also be reconstructed thereafter. A quick simulation of the MIIPS process can be given in a following manner: first we construct a spectral phase function by randomly assigning weighting coefficient like the following expression.

$$\Psi(\omega) = a_1 \cdot \Psi(sin) + a_1 \cdot \Psi(quadratic) + a_1 \cdot \Psi(cubic) \tag{3.10}$$

Then we scan a sinusoidal phase function like (3.7) with scanning parameter δ across the full spectral region. In Figure 4.7, we display the simulated MIIPS trace with this scanning phase function, as a comparison, we simulated the MIIPS trace of ideally compressed pulse case (i.e. transform limited).

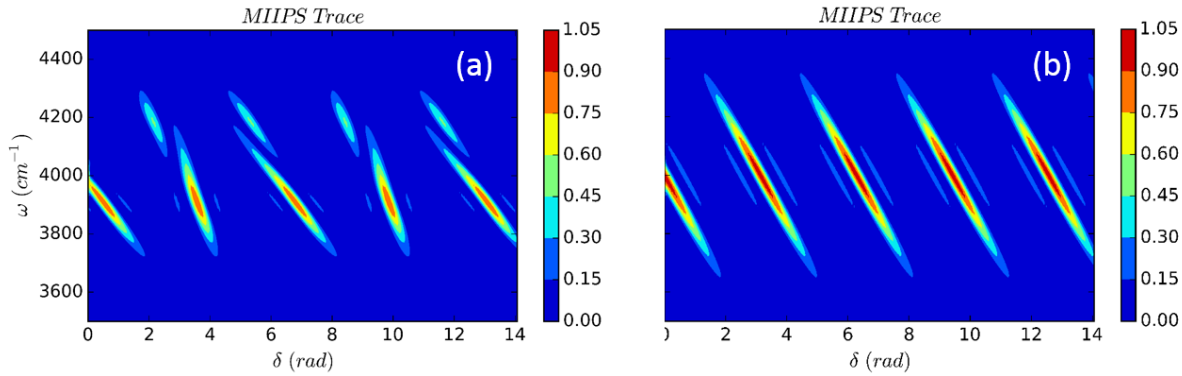

Figure 4.7 Simulated MIIPS trace (a) before and (b) after correcting the random phase

4.2 High Pressure and High Temperature Gas Cell

The high-pressure high temperature (HPHT) gas cell was designed to hold pressures up to 1000 psia and temperatures up to 1000 K. The design concept is to be scalable and provide insights for the high-pressure rocket experiment. The schematic drawing of the gas cell and a zoom in view near the optical port are shown in Figure 4.8.

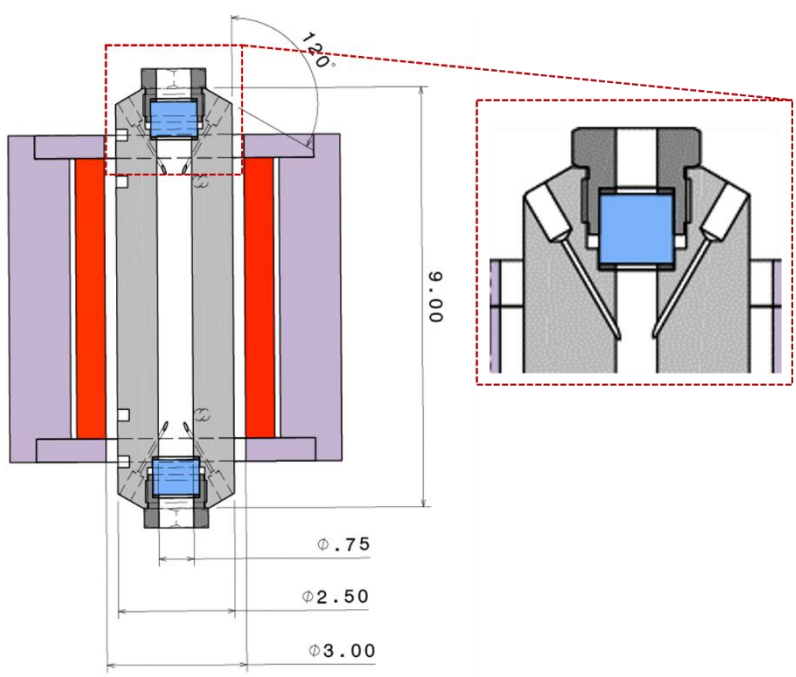

Figure 4.8 Schematic drawing of the HPHT cell.

The HPHT cell can be generally sorted into three parts: an external radiant heater, the gas cell main body and the optical port for femtosecond laser access. The radiant heater is designed to encompass the gas cell main body and is in total 6'' long. During operation, the cell is drawn to vacuum and filed to prescribed amount of gas mixtures using partial pressures. A radiant electrical heater (Thermcraft Inc. RH274) with feedback from a temperature regulator with PID control is used to heat the gas-cell to prescribed temperatures. An array of thermocouples is used to ensure uniform temperature distribution in the gas-cell and to verify the CARS measurements. The main cell body is built out of a single round-bar of Hast-X. 8XAS5202-02 ports are built to enable fuel, oxygen and inert gas injection and ventilation. The optical port uses a AS5202-16 'plug' adapted for window installation, the sealing between the optical port to the cell body is made through metal O-ring. Finally, for the proper material for the windows access, it needs to be able to hold high pressure high temperature as designated in the experiment, besides, it needs to have small frequency dispersion and high transmission as possible at 800 nm. Thus, fused quartz is chosen, the windows are 1'' diameter and 0.75'' thick with a 0.5° wedge angle to prevent etalon effect. The sealing between the windows and the optical port is through grafoil gaskets. To enable easier switch between the HPHT cell experiment with the rocket chamber experiment, a flexible data acquisition system is also built that the gas cell and the rocket chamber can be mounted on a rail.

4.3 Rocket Combustion Chamber

In addition to the gas-cell, experiments are planned in a rocket combustion chamber operated at elevated pressures. The rocket combustion chamber is designed to provide optical access for fs-CARS measurements at discrete axially distributed locations in the combustion chamber. The combustor is operated with methane or hydrogen as fuel and gaseous oxygen as the oxidizer. The reactants are introduced in the combustion chamber at ambient temperature using a shear co-axial injector. The flame is stabilized over the backward facing step of the combustor. A schematic representation of the rocket chamber as well as the injector are shown in Figure 4.9. The combustor will be operated at a range of mean chamber pressures for 1-10 MPa to allow quantification of the temperature field in the injector near field as well as near the exit nozzle using fs-CARS

measurements. Measurements in the gas-cell will be used to help guide the appropriate phase matching scheme and target species to be used for thermometry.

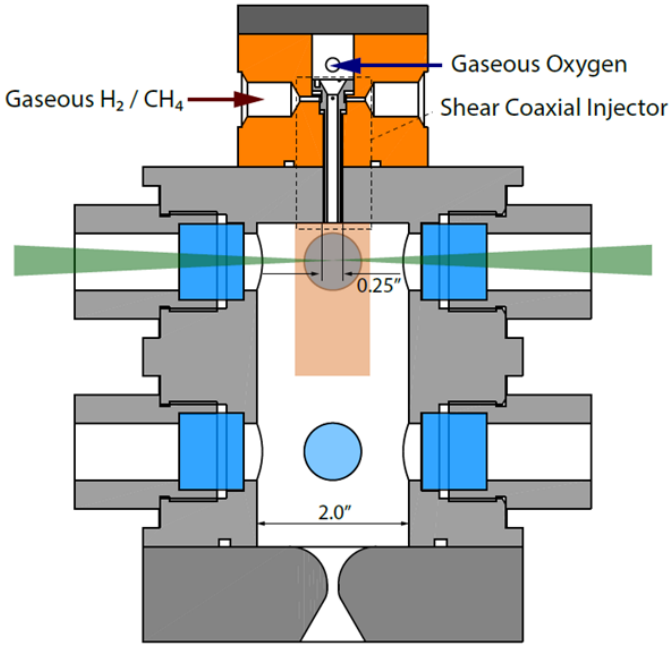

Figure 4.9 Schematic drawing of the high pressure rocket combustion chamber for the fs CARS measurements.

Table 4.2 High-pressure rocket combustor injector details for hydrogen-oxygen configuration

Injection Geometry	Values
Ox-post diameter (in)	0.141
Ox-post length (in)	2.303
Fuel collar thickness (in)	0.035
Fuel annulus gap (in)	0.017
Exit throat diameter (in)	0.150

Table 4.3 Instrumentation details for gas cell and the high-pressure rocket combustor

Measurement	Instrumentation	Range	Accuracy
LF Pressure	GE Sensing UNIK50E6	200-3000 psia	0.04% FSO
HF Pressure	Kulite WCT-312M-3000A	500-3000 psia (2 MHz)	0.1% FSO
Temperature	K-type thermocouple (GKMQIN-062G-06)	< 1523 K	2.2°C or 0.75%

4.4 CARS Signal Generation and Collection

In this thesis, the CARS signal is generated by focusing the pump, Stokes, and probe laser beams through a 500 mm plano-convex lens. The phase matching condition is satisfied ($\vec{k}_{CARS} = \vec{k}_{pump} - \vec{k}_{Stokes} + \vec{k}_{probe}$) with a folded BOXCARS geometry as shown in Figure 4.10.

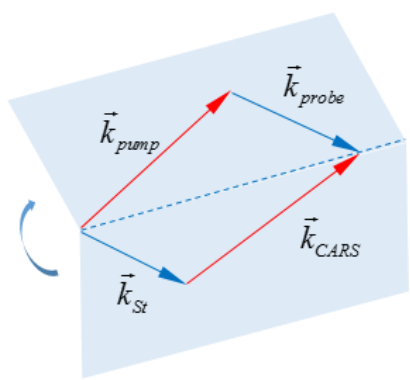

Figure 4.10 BOXCARS phase-matching geometry for typical N_2 vibrational CARS setup.

The probe volume can be calculated according to the laser beam diameter on the focusing lens the laser wavelength and the focal lens length according to Eq. (4.11).

$$d = 4M^2 f\lambda / (\pi D) \tag{3.11}$$

where M^2 for a Gaussian beam is 1.5. For the 500 mm focusing lens, the 800 nm Stokes pulse diameter on the lens is about 11mm. This results in the probe volume width of about 70 μm. The length of the probe volume can be determined by scanning a thin film BBO crystal alongside the laser propagation direction. The resultant probe volume length is about 800 μm. Temporal overlap

is achieved first by finding the mixing signal inside a 100 μm thick BBO crystal at the probe volume and then optimized by observing the nonresonant signal in pure argon. A typical image of the nonlinear mixing signals is shown in Figure 4.11.

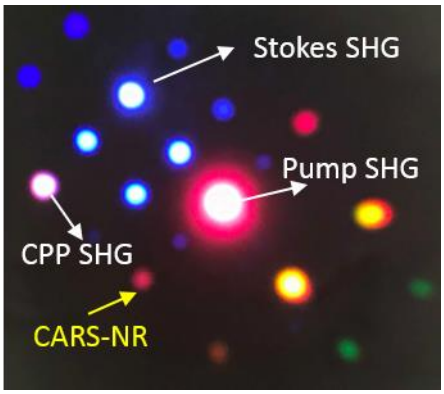

Figure 4.11. Image of the mixing signals from the BBO crystal along with the pump, Stokes and probe beams. Spatial separation of the CARS signal generation is realized by phase matching conditions using BOX CARS geometry.

Typical pulse energies for the pump, Stokes and probe beams at the probe volume were about 80 μJ, 80 μJ, and 320 μJ respectively. Before the focusing lens, a thin film polarizer and a half-wave plate is used for laser energy control especially at high pressure measurement where self-phase modulation can become significant. Without extra chirping glass, the pump and Stokes pulses are close to FTL as inferred from the spectral fitting code. The probe beam is chirped extensively from 55 fs to approximately 3 ps though a 30 cm SF10 glass rod to map the Raman coherences into frequency domain for single shot measurements. The CARS signal is finally directly into 0.5 m, Czerny-Turner-type spectrometer and sent into an electron-multiplying charge-coupled device camera system (Andor IXon Ultra 888). The size of the detection pixel is 13 μm and the dimension of the CCD array is 1024x1024, the camera uses cropped acquisition mode so that the image falls only onto the bottom 55 rows and this enables the camera to be synchronized at 5kHz with the laser repetition rate.

4.5 Processing of Experimental Data

The CPP fs CARS spectrum needs to get interoperated through spectral fitting code to extract useful information like temperature, species concentration etc. The general procedures for the CARS data processing is shown in Figure 4.12.

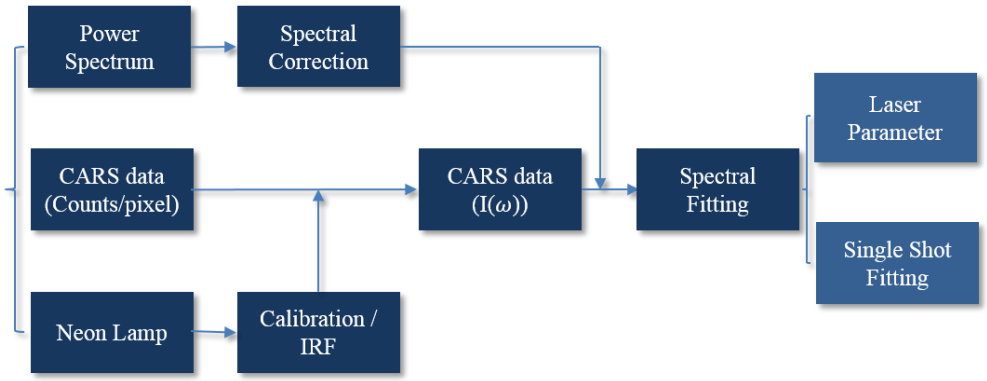

Figure 4.12. General procedures for CARS data processing

4.5.1 Data Acquisition and Post-processing

The data acquisition includes the recording of laser power spectrum (for pump, Stokes, and probe pulses respectively), the Neon lamp calibration spectrum and the original CPP fs CARS spectrum.

The power spectrum of pump, Stokes and probe beams are recorded right before the probe volume by a fiber-optic-coupled spectrometer (USB-VIS-NIR, Ocean Optics Inc.). These optical spectra require spectral correction based on the quantum efficiency curve of the instrument. As shown in Figure 4.13, within the wavelength range for pump (620-690 nm), Stokes and probe (770-825 nm) beams, the spectral correction is not significant as the spectrometer is optimized in this region. For high pressure CARS experiment, the laser power spectrum might need to be evaluated near the probe volume as the high-pressure gas or the glass windows can distort the spectral component of the input laser fields. The spectral profile of the pump pulse from OPA is closer to skew-Gaussian while the split of the 800 nm amplifier output (Stokes and probe) is more like Gaussian shaped. The typical spectral bandwidth (FWHM) for the pump, Stokes and probe beams are 450 cm^{-1}, 300 cm^{-1} and 350 cm^{-1} respectively. The broader bandwidth of the probe beam than

the Stokes beam is possibly due to the accumulated self-phase modulation inside the SF-10 chirping glass rod.

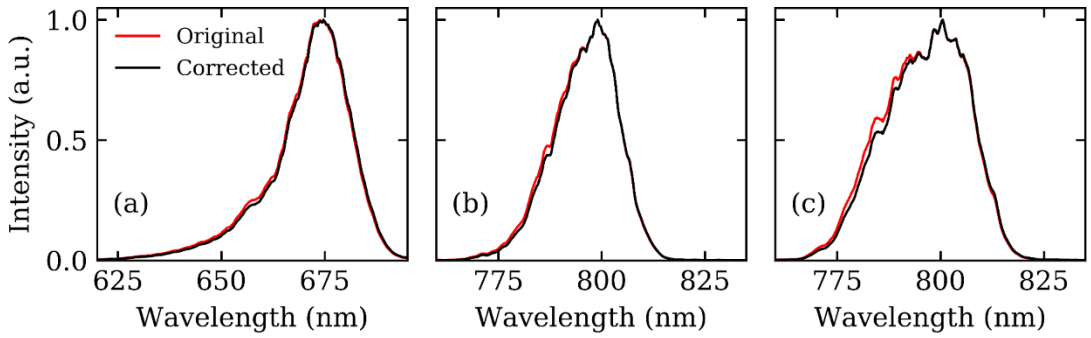

Figure 4.13. Recorded power spectrum before and after spectral correction for (a) pump (b) Stokes (c) probe beams.

The neon lamp data is needed to perform the frequency to pixel mapping on the CCD camera as well as to compute the wavelength dependent instrument response function (IRF). A typical Neon lamp calibration spectrum near 675 nm is shown in Figure 4.14.

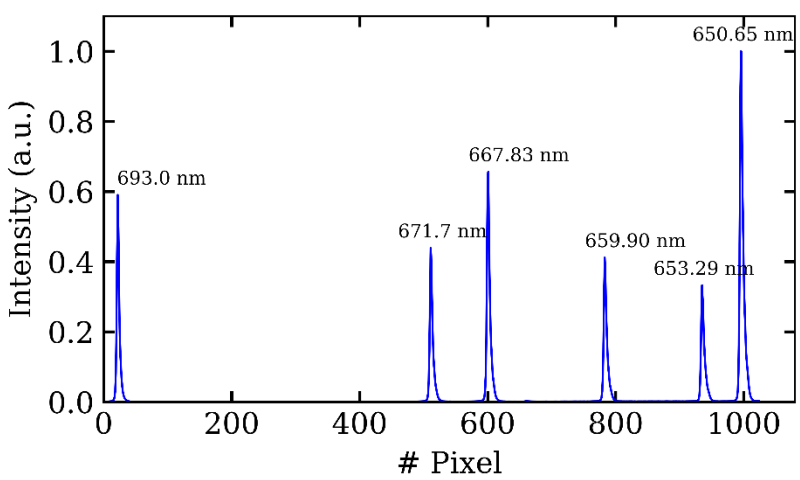

Figure 4.14 Neon calibration lamp spectrum near 675 nm. The fitted atomic line positions (in wavelength) have been added.

The first step of Neon lamp calibration is to fit the measured Neon lamp lines to the known atomic transitions, the frequency to pixel mapping is then established by assuming linear interpolation. The bandwidth of each atomic line can also be measured (FWHM), and it can be modelled as wavelength dependent. Usually, IRF linewidth can be modelled as a polynomial function

$$\Delta\omega_{IRF} = a\omega^2 + b\omega + c \tag{3.12}$$

where $\Delta\omega_{IRF}$ is the measured atomic line bandwidth, and a, b and c are the fitting coefficients. An example of the IRF linewidth polynomial fitting function is as shown in Figure 4.15.

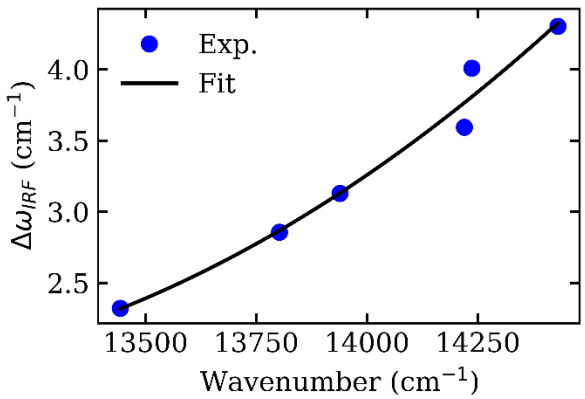

Figure 4.15 IRF linewidth as a function a frequency. The fitting curve is a quadratic polynomial function like Eq.(3.12)

Assuming a Gaussian-shaped IRF profile, the IRF function can be given by

$$IRF(\omega) = \exp\left[-4\ln(2)\left((\omega-\omega_c)/\Delta\omega_{IRF}\right)^2\right] \tag{3.13}$$

Physically, IRF is as an aftermath of the spectrometer resolution, camera pixel size and entrance slit size etc. For example, the ideal Neon atomic transition linewidth should be infinitesimally narrow, the measured linewidth is much greater because the spectral broadening caused by instrument limitations. Similarly, the measured CPP fs CARS spectrum will also experience the same IRF as it was retrieved from the Neon lamp measurement. For accurate spectral fitting of the experimental data to the theoretical calculation, we need to either spectrally convolve

the theoretically calculated CARS spectra with the IRF or deconvolve the experimentally measured spectra so as to compared with the theoretical calculation.

$$S(\omega) = \int_{-\infty}^{\infty} S^0(\Omega) IRF(\Omega - \omega) d\Omega \tag{3.14}$$

In Eq. (3.14), $S^0(\Omega)$ is the theoretically calculated CARS signal and $S(\omega)$ is the CARS signal after IRF convolution. In general, the processed CPP fs CARS spectrum and the power spectrum for pump, Stokes and probe beams will be used in the next stage of spectral fitting

4.5.2 Spectral Fitting

The spectral fitting code for CPP fs CARS was first developed by Richardson et. al [41] and was later optimized by Dennis [131] and Thomas[132]. A summary is given here. There are two main stages for the CPP fs CARS spectral fitting. First, CPP fs CARS spectrum was acquired at a reference condition. For example, we used laminar flame over a near-adiabatic Hencken burner with a 'known temperature' for the calibration measurement. The calibration measurements were shot-averaged and was then analyzed to extract the corresponding laser parameter set (laser parameter code). The laser parameters are all in the phenomenological model which has been discussed in Chapter 3. For completeness, some essential equations are summarized here.

$$P_{nres}(t) = \alpha E_{pu}(t) E_{St}^{*}(t) \tag{3.15}$$

$$P_{res}(t) = \beta \left[\int_{-\infty}^{t} E_{pu}(t') E_{St}^{*}(t') dt' \right] \sum_i \left\{ \Delta N_i \left(\frac{d\sigma}{d\Omega} \right)_i \cos(\omega_i t + \phi) \exp(-\Gamma_i t) \right\} \tag{3.16}$$

$$E_{CARS}(t) = E_{pr}(t) \left[P_{res}(t) + P_{nres}(t) \right] \tag{3.17}$$

For each electric field function, the time domain characterization can be related to the frequency information as

$$E(t) = \int_{-\infty}^{+\infty} A(\omega) e^{i\psi(\omega)} e^{i\omega t} d\omega \tag{3.18}$$

where $A(\omega)$ is the spectral amplitude function, the spectral phase function can be approximated as polynomial as

$$\psi(\omega) = a_0 + a_1\omega + a_2\omega^2 + a_3\omega^3 + \ldots \tag{3.19}$$

The constant phase and linear phase do not affect the temporal envelope and can be neglected. For pump and Stokes pulses, only the quadratic phase needs to be included, while for the probe pulse, both quadratic and cubic phase need to be included. The coefficients for those phase terms are as the floating parameters in the laser parameter code. Other than those parameters, there are 6 other laser parameters, and they are summarized in Table 4.4.

Table 4.4 Summary of floating parameters in the laser parameter code. ϕ is the relative resonant/nonresonant phase as in Eq. (3.16). τ_{St} and τ_{pr} denote the Stokes delay and probe delay, $\Delta\bar{x}$ and $\Delta\bar{y}$ are the horizontal and vertical shift, β/α is the relative resonant to nonresonant scaling factor.

Parameter	Typical Floating Range
$a_{3,probe}$	-15000 fs^3~1000 fs^3
$a_{2,probe}$	-28000 fs^2~20000 fs^2
$a_{2,pump}$	-2000 fs^2~0 fs^2
$a_{2,Stokes}$	-2000 fs^2~0 fs^2
ϕ	0-360°
τ_{st}	-60 fs~60 fs
τ_{probe}	\
$\Delta\bar{x}$	\
$\Delta\bar{y}$	\
β/α	\

The mathematic algorithm used for the parameter optimization in the spectral fitting code is called 'differential evolution'. It is a gradient descent technique that can converge to the global optimum solution [133]. A comparison between the experimental measured N_2 CPP fs CARS spectrum with its theoretical fit is shown in Figure 4.16

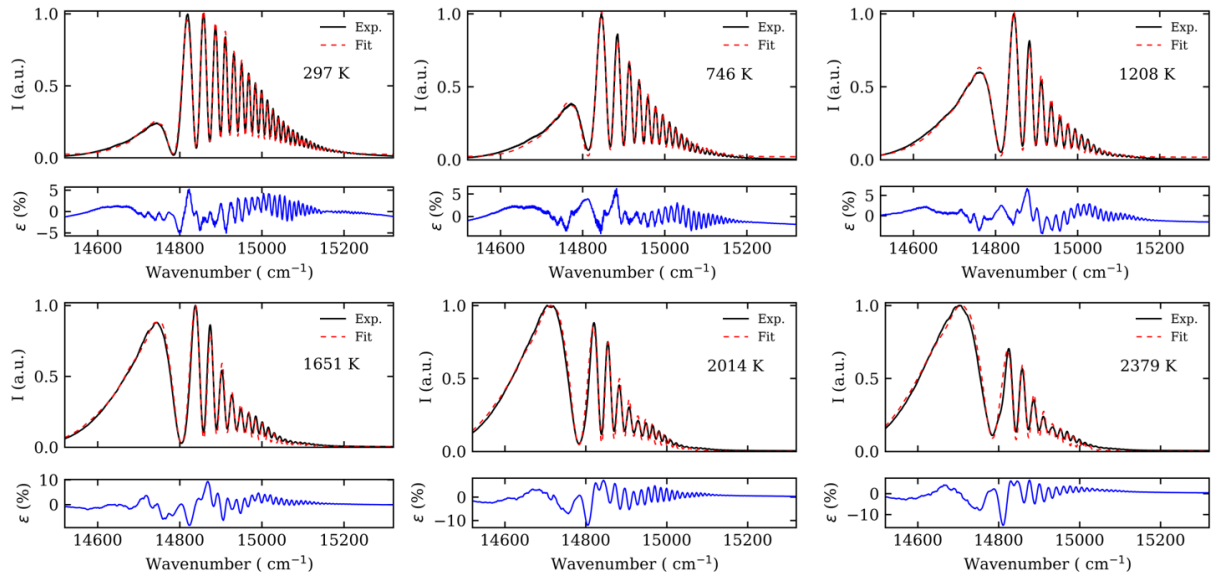

Figure 4.16 N_2 CPP fs CARS spectrum at various temperatures and their corresponding spectral fitting results. The probe delay is 1.2 ps, the residual between the experiment and the fitting result is displayed below.

For the single shot fitting code, only the temperature and the temperature dependent resonant/nonresonant ratio will be floated, the rest of the parameters are kept the same as in the laser parameter code. However, the laser parameters can be slightly different when they are extracted from different calibration flame temperatures. A possible explanation of the variations of laser parameters retrieved at different temperatures is due to sef-phase modulation effects. For example, at atmospheric pressures, low temperature indicates high number density thus stronger SPM, the accumulated nonlinear phase can modulate the laser spectra and on the fitting parameters.

$$\varepsilon_i = \int \left[S_{exp}(\omega) - S_{theory}(\omega) \right]^2 d\omega \tag{3.20}$$

$$T = \sum_i \frac{T_i}{\varepsilon_i} \tag{3.21}$$

One way to mitigate the uncertainty introduced by different laser parameter set is to first use a single set of laser parameter to fit the reference spectra recorded at several calibration temperatures, the corresponding fitting errors will then be compared and the best laser parameter set is the one that with minimum fitting error across the temperature region of interest. Another strategy is to use a weighted fitting scheme. I.e., as shown in Eq.(3.20) and Eq. (3.21), for a given CPP CARS spectrum with unknown temperature, it will be fit using several different laser parameter sets. The

final temperature can then be determined by weighting the different fitted temperatures, with the weights determined based on their corresponding fitting errors, the spectra with low fitting errors are weighted more heavily. Examples of using the error-weighted fitting scheme will be shown in the following section.

CHAPTER 5. FREQUENCY CHIRP EFFECTS ON CPP FS CARS

For fs CARS measurement in high-pressure systems, frequency chirp can happen when laser pulses transmit through dispersive materials like thick glass windows. The purpose of this study is to exam the effects of frequency chirp both experimentally, by inserting disks of SF11 glass into the pump and Stokes beam paths, and theoretically by incorporating pulse chirp into our time-dependent density matrix simulations (TDDM). Experimentally, we found that inducing moderate pump and Stokes chirp produced significant spectral narrowing of the nonresonant four wave mixing contribution to the CARS signal and allowed us to control the resonant excitation bandwidth to eliminate interferences from neighboring species. The temperature measurement accuracy and precision were essentially unchanged with respect to the unchirped pump and Stokes case. The effect of moderate pump and Stokes chirp on the narrowing of the Raman excitation efficiency envelope was investigated by solving the full set of time dependent density matrix equations (TDDM) through direct numerical integration (DNS). And the numerical efficiency has been advanced by enabling parallel computation.

5.1 Frequency Chirp Characterization

In the TDDM calculation, the temporal characterization of the laser electric fields is required. However, it is more straightforward to include the effects of frequency chirp in the frequency domain because chirp affects only the spectral phase function.

$$E(\omega) = A_{\omega}^{0} \exp\left(\eta\omega^{2}\right) \exp\left[i\left(\gamma\omega^{2} + \beta\omega^{3}\right)\right] \tag{4.1}$$

In Eq. (4.1), A_{ω}^{0} denotes amplitude of the electric field function and η determines the spectral bandwidth of the pulse; for the spectral phase function, the zero order phase term is omitted because it is a constant for all frequency components; the linear phase term is not included because it can be addressed by relative pulse delay. For a Gaussian shaped pulse with inclusion of only quadratic spectral phase function (linear chirp), the temporal expression for the laser electric field can be given through inverse Fourier transform

$$E(t) = A_{t}^{0} \exp\left[-2\ln(2)\left(\frac{t}{\tau}\right)^{2}\right] \exp\left(-i\omega_{j}t\right) \tag{4.2}$$

Similarly, A_t^0 is the electric field amplitude in time domain representation, τ denotes the temporal pulse duration (full width at half maximum, FWHM) and ω_j is the instantaneous carrier frequency

$$\omega_j = \omega_{j,0} + \frac{\gamma t}{4\left(\gamma^2 + \eta^2\right)} \tag{4.3}$$

where $\omega_{j,0}$ is the carrier frequency for the transform limited pulse.

The ratio of the temporal duration of the chirped pulse to the temporal duration of the Fourier transform limited pulse is given as [41, 84]

$$\frac{\tau\left(\gamma \neq 0\right)}{\tau\left(\gamma = 0\right)} = \sqrt{1 + \left(\frac{\gamma}{\eta}\right)^2} \tag{4.4}$$

For our CPP fs CARS experiments, the probe beam is chirped from approximately 55 fs to approximately 3 ps. Consequently, for accurate spectral phase characterization for the probe pulse, both quadratic and cubic terms must be included. For the pump and Stokes beams, the extent of the chirp is much less, and only the quadratic phase is required. Both the quadratic and cubic spectral phase information can be estimated from the dispersion properties and thicknesses of the glass materials through which the beams are transmitted.

In practical high-pressure combustion studies, frequency chirp will be induced by a few centimeters of thick windows composed of materials such as fused quartz. In this work, moderate frequency chirp was imposed on the pump and Stokes pulses by inserting 10-mm-thick disks of SF11 glass in the pump and Stokes beam paths. According to Sellmeier equation, frequency chirp parameter γ, GDD and material property can be related as shown in Eq. (5.5).

$$2\gamma = GDD = L\frac{\lambda^3}{2\pi c^2}\left(\frac{d^2 n}{d\lambda^2}\right) \tag{4.5}$$

where L denotes the thickness of optical transmittance length, λ is the central wavelength, c stands for speed of light and n is the wavelength dependent material refractive index. Correspondingly, this resulted in an overall GDD of about 2400 fs^2 and 2000 fs^2 for the pump and Stokes beams respectively. According to Eq. (4.4), the insertion of the SF11 glass stretched the pulse lengths of the Stokes and pump beams from approximately 55-60 fs to 120-150 fs. In Figure 5.1, we showed the nonresonant CARS signal recorded at argon when different lengths of SF-11

glass rods were added into the pump and Stokes paths. The trend of nonresonant narrowing with increasing SF-11 rods length agrees well with the simulation where pump and Stokes electric fields were convoluted.

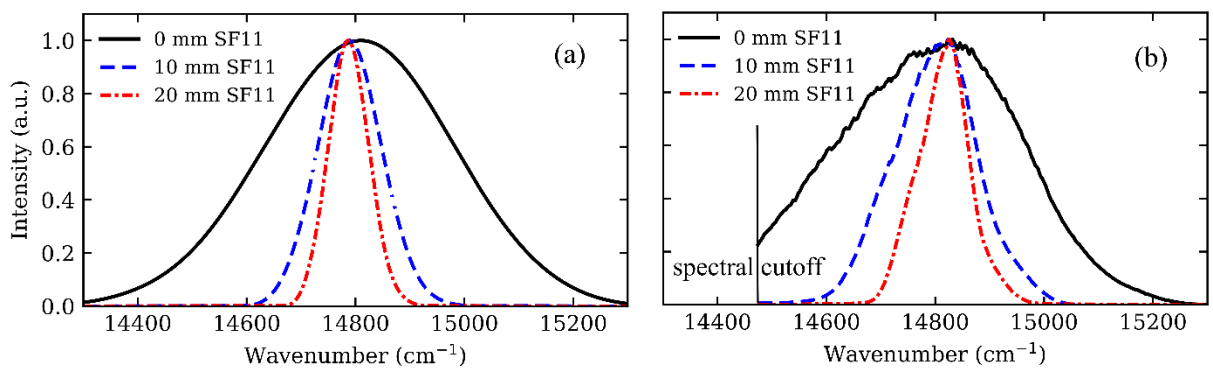

Figure 5.1 Comparisons between the theoretical calculation and experimental results of nonresonant signal in Argon.

5.2 Density Matrix Calculation of Raman Efficiency

The excitation efficiency for various Q-branch transitions can be obtained by constructing and solving the full set of density matrix equations through direct numerical integration, and the result for chirped and FTL pulses are shown in Figure 5.2. For FTL pump and Stokes pulses, the Raman excitation efficiency is basically identical within each vibrational manifold. The differences of the efficiency among different vibrational levels is because the vibrational number dependence of the Raman cross section.

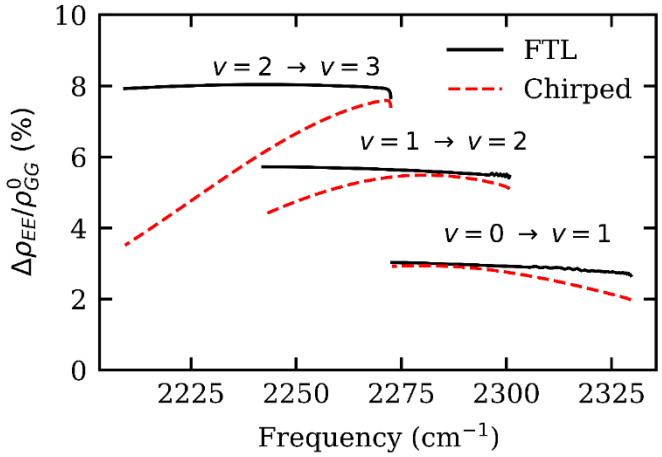

Figure 5.2. TDDM calculation of Raman excitation efficiency for FTL and chirped pump and Stokes pulses. The frequency difference between the pump and Stokes beams is set to 2280 cm^{-1} to match the experiment, transform-limited pump and Stokes pulse durations are 55 fs and the chirped pulse duration is set to be 125 fs. Nitrogen vibrational levels from v=0 to v=3 and rotational levels from J=0 to J=60 are included in the calculation.

Alternatively, we defined the normalized Raman excitation efficiency by dividing the Raman cross section.

$$\varepsilon = \frac{\Delta\rho_{EE}}{\rho^0_{GG}\left(\frac{d\sigma}{d\Omega}\right)_{EG}} \tag{4.6}$$

The vibrational Raman cross section exhibits a slight dependence on the rotational quantum number J through the Placzek-Teller coefficients, and is proportional to v+1, where v is the vibrational quantum number. The results of TDDM calculations of the normalized Raman excitation efficiency for chirped and FTL pulses are shown in Figure 5.3.

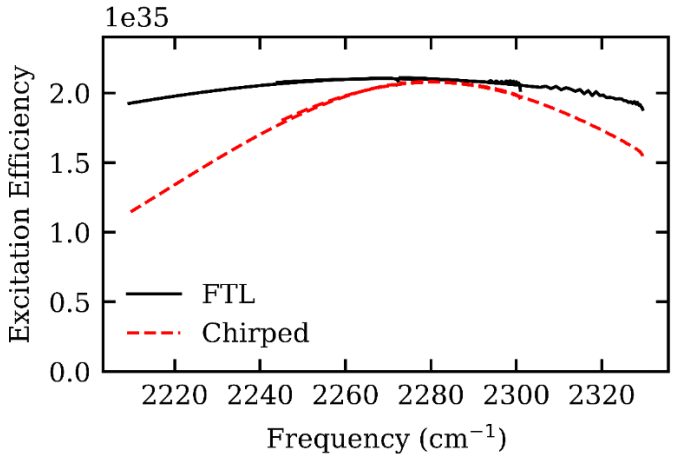

Figure 5.3. TDDM calculations of the normalized Raman excitation efficiency for FTL and chirped pump and Stokes pulses.

For the calculations shown in Figure 5.3, the difference between the central frequencies of the pump and Stokes beams was set to 2280 cm^{-1}. For FTL pump and Stokes pulses, the convolved spectral bandwidth between pump and Stokes pulses is about 350 cm^{-1}. This is greater than the frequency span of the ro-vibrational transitions for N_2 (~100 cm^{-1}), and therefore the Raman excitation efficiency is nearly the same for each Raman transition within the (v', v'') = (1,0), (2,1), and (3,2) vibrational manifold. For pump and Stokes pulses which are chirped from 55 fs to 125 fs, the effective convolved bandwidth between pump and Stokes pulses is approximately 140 cm^{-1}. The decrease in the Raman excitation efficiency at Raman transition frequencies both higher and lower than the central pump-Stokes frequency difference of 2280 cm^{-1} is obvious.

For the consideration of the CPP fs CARS spectral fitting, TDDM calculation for Raman excitation efficiency will become computational expensive because it needs to get updated every time the fitted spectral phase value changes. An alternative approach is to use the convolution product between pump and Stokes electric fields[81, 134] since the absolute value of the Raman excitation efficiency is less important in the spectral fitting module. As shown in Eq.(5.7), for given *Q* branch transition with transition frequency Ω, this pumping efficiency profile is proportional to the convolution product between the pump and Stokes electric field functions, as given by

$$\Delta\rho_{EE}(\Omega) \propto \left| \int E_p(\omega) E_{St}^*(\omega - \Omega) d\omega \right|^2 \tag{4.7}$$

A comparison of the normalized Raman excitation efficiency obtained from spectral convolution and from TDDM calculation is shown in Figure 5.4. In general, the convolution product matches with the TDDM calculation, though the Raman excitation efficiency for the convolution calculation is slightly greater than for the TDDM calculation for transitions frequency Ω that are significantly different than the central pump-Stokes frequency difference of 2280 cm^{-1}. The shape of the Raman excitation efficiency profile must be incorporated into the physical modeling, especially at flame conditions where several vibrationally excited levels are populated.

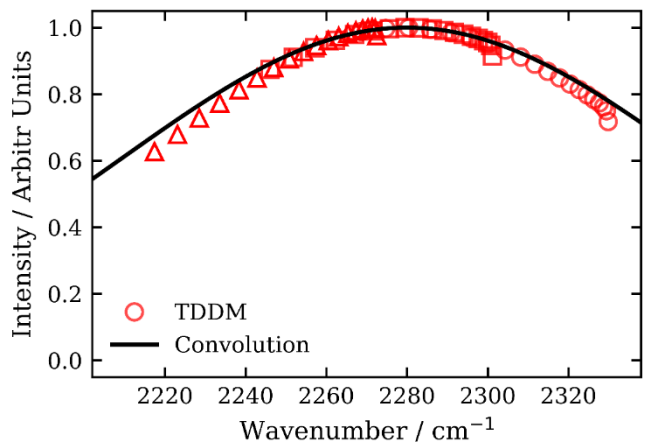

Figure 5.4. Comparison of the Raman excitation efficiency (normalized) obtained from TDDM calculation and spectral convolution. Both pump and Stokes pulses durations are chirped from 55 fs to 125 fs. Nitrogen vibrational levels from v=0 to v=1 and rotational levels from J=0 to J=60 are included in the calculation. The circle, square and triangle markers denote the normalized excitation efficiency for the fundamental band, first and second hot band respectively

TDDM calculations of the N_2 CPP fs CARS signal at three different temperatures are shown in Figure 5.5. for FTL and chirped pump pulses. The TDDM calculation of the nonresonant signal is also shown, the CPP fs CARS signal contains both resonant and nonresonant components.

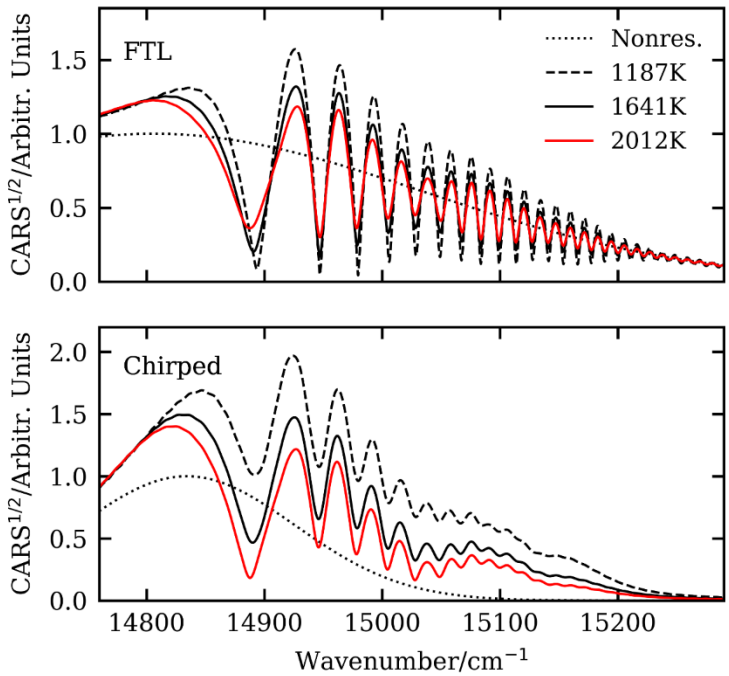

Figure 5.5 TDDM calculation of CPP fs CARS signals for three different temperatures for FTL (top panel) and chirped pump and Stokes pulses (bottom panel). The pump, Stokes, and probe pulse parameters are the same as those used for the calculation of the Raman excitation efficiency curve in Figure 5.3.

For moderately chirped pump and Stokes pulses, the nonresonant spectrum, as shown in TDDM calculation, is significantly narrowed. In particular, the nonresonant signal is minimized in the high-frequency portion of the spectrum which is more temperature-sensitive. For the chirped pulse case, the CPP fs CARS signal modulation near 15050 cm^{-1} is clearly evident, while this it is not apparent for FTL pulses. This signal modulation, which has a frequency width of approximately 50 cm^{-1}, is due to the heterodyning between the Raman coherences for the fundamental vibrational band ($v''=0 \rightarrow v'=1$) and the hot bands ($v'' \geq 1 \rightarrow v'= v''+1$). A signal modulation with a much narrower frequency bandwidth is also evident in all the spectra shown in Figure 5.5. For the unchirped case, the high-frequency signal modulation is due to the interference between the nonresonant background and the resonant CARS signal. In brief, our TDDM calculations indicate that moderate amount of frequency chirp can be beneficial for CPP fs CARS measurement, when we consider, for example, the potential of nonresonant suppression and consequently the improvement of temperature sensitivity.

5.3 Results and Discussions

The temperature measurements precision and accuracy for the CPP fs CARS system with moderately chirped pump and Stokes beams were tested by performing single-shot measurements in near-adiabatic Hencken burner flames[9]. The temperature was determined from the single-shot spectra using the spectral fitting algorithm discussed earlier. Recently, we have also developed a parallel version of the phenomenological model, resulting in greatly enhanced numerical efficiency for the genetic algorithm fitting routine. The computational time was reduced by more than one order of magnitude by using 24 computational threads. Also, the accuracy of the physics incorporated in the phenomenological model was improved by incorporating the excitation efficiency profile for different Q branch transitions as shown in Figure 5.2, rather than assuming that all Raman transitions were excited with the same efficiency.

An example of the laser parameters extracted from the spectral fitting code is summarized in

Table 5.1. The nominal spectral phase values are inferred from the material dispersion properties of the SF-10 glass and SF-11 glass. The relative pulse timing parameters are inferred from the fine adjustment of the translation stage by observing the nonresonant signal in pure argon. The quadratic spectral phase values for the pump and probe beams extracted from the fitting code are all slightly lower than the nominal values, while the fitted quadratic phase of Stokes pulse is slightly higher than predicted. This could be due to the uncertainty of determining the center frequency of the pulses, also, there could be extra frequency chirp due to all the routing optics. The cubic phase of probe pulse is very much different than the prediction, aside from the uncertainty in center frequency determination, we found that within the spectral bandwidth of the probe beam, the magnitude of cubic phase was much smaller than the quadratic phase, so the influence from cubic spectral phase is also less significant. The extracted pump and Stokes delay as well as probe delay are satisfactory when considering the minimum adjustable time step of the translation stage is about 10 fs. The phase term denotes the relative temporal phase between the resonant and nonresonant response and will in general influence the modulation pattern of the CPP fs CARS signal.

Table 5.1 Fitted laser parameters from the fs CARS spectral fitting code. The experimental data was taken from Hencken burner flame with fuel/air equivalence ratio ϕ = 0.5, 10 mm SF-11 glass was inserted into the optical path of pump and Stokes pulses.

Laser Parameters	Units	Fitted Value	Nominal Value
β_{pump}	fs^2	1125	1250
β_{Stokes}	fs^2	1399	959
β_{probe}	fs^2	23180	24969
γ_{probe}	fs^3	9615	5463
Stokes delay	fs	-3	0
Probe delay	ps	1.16	1.2
Phase	deg.	47	\

For moderately chirped pump and Stokes pulses, the fitted CPP fs CARS spectrum as compared to the experimental data is shown in Figure 5.7. The signal modulation near 15050 cm^{-1}, as indicated in Figure 5.5, is consistent with our TDDM calculation. The fitted spectrum matches the experimental data satisfactorily. The high-frequency modulation for the fitted spectrum is observed to be slightly weaker than for the experimental spectrum. This is probably because our fitting code does not include a broadband resonant contribution from the pure rotational interaction. As shown in Figure 5.6, the two broad band 792 nm pulses (Stokes and probe) can effectively serve as pump and Stokes pulses to excite the pure rotational transitions of N_2 [36]. This broadband pure rotational CARS signal will overlap spatially with the vibrational CARS signal at the CCD camera, and will interfere with the nonresonant background. The interference is probably responsible for the high-frequency modulation of the signal at frequencies higher than 15,000 cm^{-1}. While this is an interesting effect, it will not affect the accuracy of temperatures determined from the experimental spectra. We will incorporate this in both our TDDM calculations and in our phenomenological model for spectral fitting in the future.

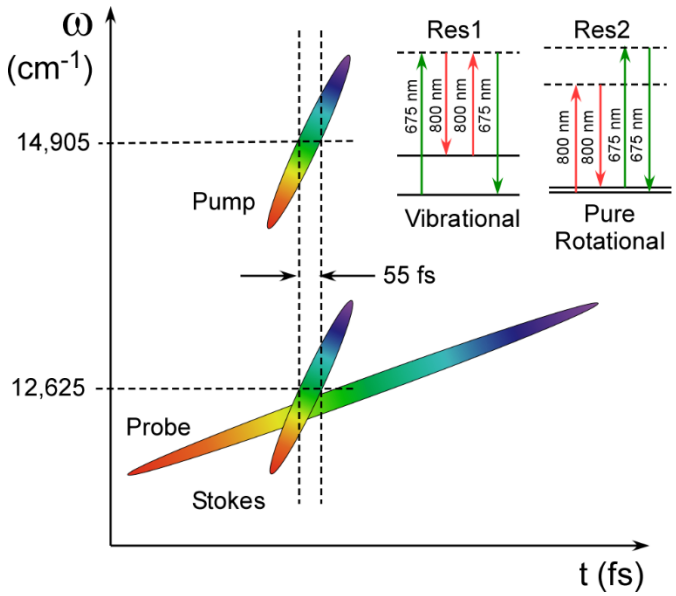

Figure 5.6. Time-frequency plots showing the CARS interaction for moderately chirped pump and Stokes beams and an extensively chirped probe beam. The energy level diagrams show the vibrational and pure rotational Raman coherences that are simultaneously excited.

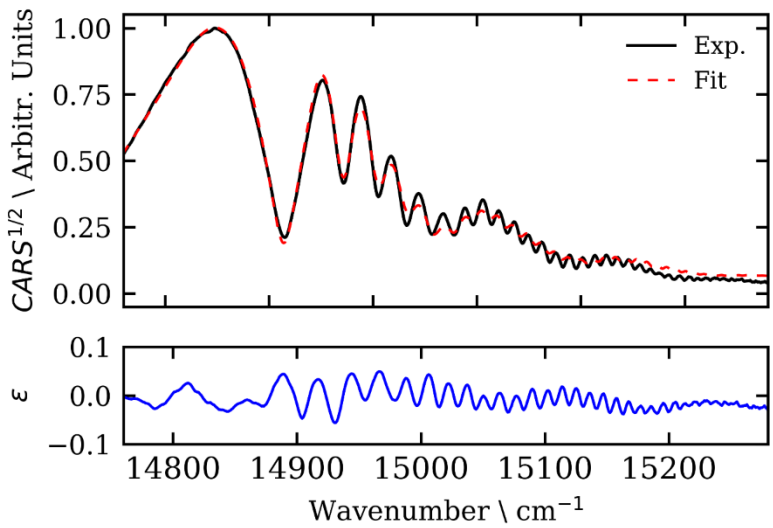

Figure 5.7. Fitted CPP fs CARS spectrum as compared to the experimental data. 10 mm SF-11 glass disks were inserted onto the optical paths for both pump and Stokes beams. The fuel-air equivalence ratio ϕ = 0.5, 2000 consecutive single shot spectra were averaged. The spectral difference ε between the fitted and the experimental data was displayed at the bottom.

As a comparison, the fitted CARS spectrum for unchirped pump & Stokes pulses is shown in Figure 5.8. Comparing to Figure 5.7, the effect of nonresonant narrowing as a result of frequency chirp is quite apparent. As is also implied in TDDM calculation, for unchirped pump and Stokes pulses case, the hot band beating is less evident because of the broadband interference between the resonant and the nonresonant signal.

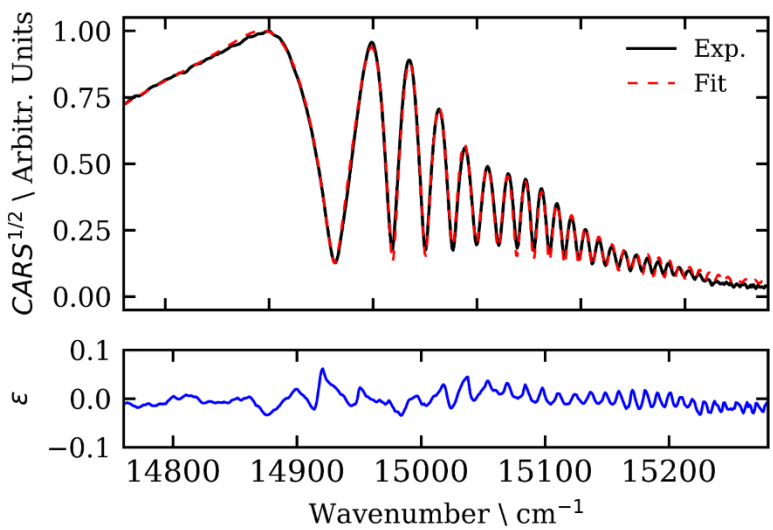

Figure 5.8. Fitted CPP fs CARS spectrum as compared to the experimental data. No extra chirping glass was added for pump and Stokes pulses. The fuel-air equivalence ratio ϕ = 0.5, 2000 consecutive single shot spectra were averaged. The spectral difference ε between the fitted and the experimental data was displayed at the bottom.

Accordingly, the fitted temperature histograms obtained from the updated fitting code for the chirped pump and Stokes system is shown in Figure 5.9. The fitting error is defined as the temperature difference between measured mean value and the adiabatic flame temperature, divided by the adiabatic flame temperature. The precision is defined as the standard deviation normalized by dividing by the mean temperature of the measurement.

$$\Delta_r = \left(T_{mean} - T_{ad.}\right) / T_{ad.} \tag{4.8}$$

$$\sigma_r = \sigma / T_{mean} \tag{4.9}$$

In Figure 5.7, one set of laser parameters was extracted from the 2000-shot-averaged $\Phi = 0.5$ spectrum. These laser parameters were then used to fit single-shot CPP fs CARS spectra from the Hencken burner operated at different equivalence ratios to obtain single-shot temperatures. For the cases with 10 mm SF11 chirping glass, the percentage error in the mean temperatures decreases as the equivalence ratio increases. The temperature measurements precision is slightly worse for the moderately chirped pump/Stokes case compare with the unchirped pump/Stokes case, despite the fact that in Figure 5.5 it appears that the moderately chirped pump/Stokes spectra exhibit more obvious temperature sensitivity. This temperature measurement precision of the unchirped pump/Stokes CPP fs CARS spectra is presumably enhanced by the higher signal strengths in the temperature sensitive region (signal frequencies above 14,900 cm^{-1}) and because of the shot-to-shot stability of the nonresonant background.

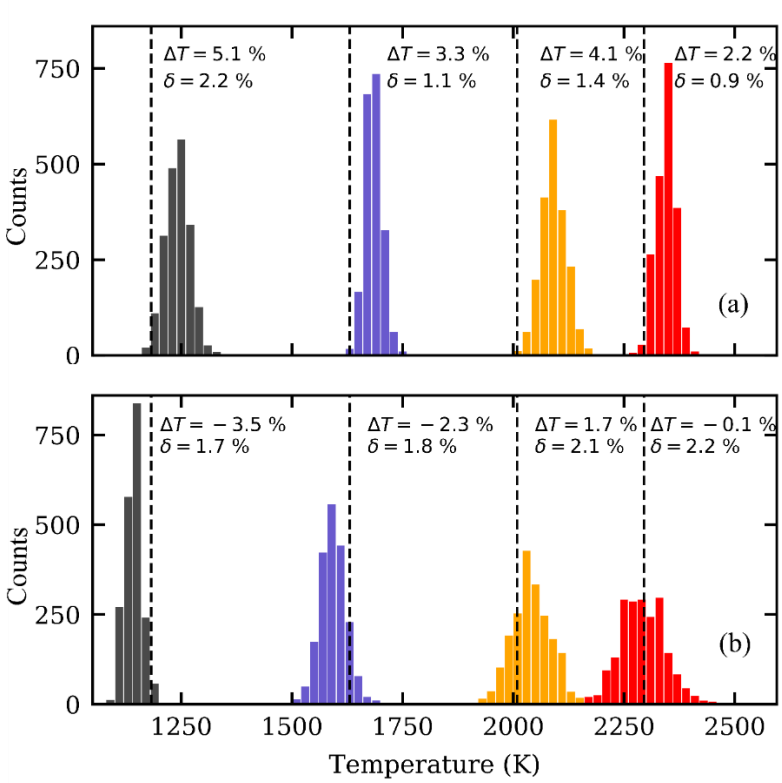

Figure 5.9. Histograms of temperature determined from fits of 2000 single-laser-shot CPP fs CARS spectra using a single set of laser parameters. The single set of laser parameters was determined from the averaged CPP fs CARS spectrum from a ϕ = 0.5 flame. The adiabatic flame temperatures are 1182K, 1630K, 2008K, and 2295K for ϕ = 0.3, 0.5, 0.7 and 0.9, respectively. (a) Unchirped pump/Stokes case. (b) Moderately chirped pump/Stokes case. For moderately chirped pump/Stokes case, 10-mm disks of SF11 glass were inserted in the pump, Stokes and probe beam paths. For the probe beam, the majority of the frequency chirp is induced by the 300-mm SF10 rod. The 10-mm SF 11 glass disk is inserted in the probe beam path to ensure that the temporal overlap is the same for the two cases.

Thomas et al.[42] recently reported a weighted fitting method to further improve the accuracy and precision for CPP fs CARS measurement. They used multiple laser parameters extracted from calibration flames at different equivalence ratios, as opposed to one equivalence ratio, to fit single-shot spectra. Based on the magnitude of the fitting errors, error weights were assigned to the fitted spectra in order to obtain a statistically weighted temperature. The weighted fit results for unchirped and chirped pump/Stokes beams are shown in Figure 5.10a and Figure 5.10b, respectively. The accuracy of temperature measurement is improved significantly by adopting the weighted fitting scheme, especially, for the unchirped pump/Stokes case. Similar to the single laser parameter fitting results, with moderately chirped pump/Stokes, slightly better

precision is observed at lower temperatures than at higher temperatures compared to the no chirp case. In general, the fitted temperature precision and accuracy for the moderately chirped pump/Stokes case is comparable to or slightly better than the unchirped pump/Stokes case. Consequently, despite our initial concerns, the transmission of the pump, Stokes, and probe beams through thick windows will not have any detrimental effects on temperature measurement precision and accuracy in high-pressure combustion systems

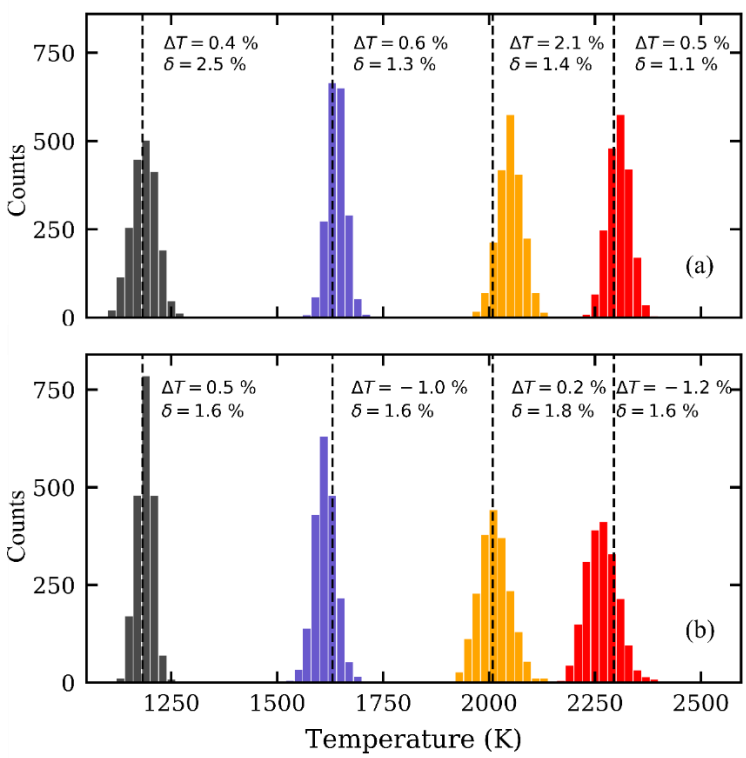

Figure 5.10. Histograms of temperature determined from fits of 2000 single-laser-shot CPP fs CARS spectra using an error-weighted fitting scheme. (a) Unchirped pump/Stokes case. (b) Moderately chirped pump/Stokes case.

Moderate chirp in the pump and Stokes beam can also help to suppress unwanted interference from species with neighboring Raman resonances. In recent temperature measurements in liquid-fueled flames[135], we encountered significant interferences in N_2 CPP fs CARS spectra when the hydrocarbon concentrations were high. These interferences resulted from the C-H stretch Raman resonances near 3000 cm^{-1}. To test the effectiveness of moderate pump/Stokes chirp for eliminating these interferences, measurements were performed for CH_4-N_2 mixtures in a static gas

cell. As shown in Figure 5.11, the narrowing of the Raman excitation efficiency envelope due to moderate pump/Stokes frequency chirp suppresses nearly completely the effects of the CH_4 interference in the N_2 spectrum. Notice that in the practical measurement local CH_4 fraction can be much higher than 50%, inducing moderate chirp is thus an easy means of discriminating against interfering CARS signals from neighboring species without adversely affecting the excitation efficiency for the target species of interest.

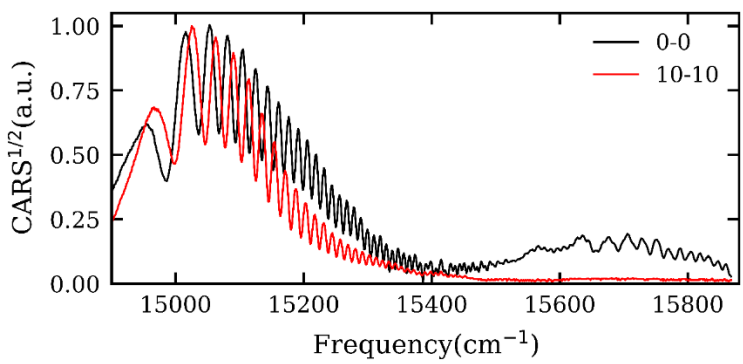

Figure 5.11. CPP fs CARS spectra for a mixture of 50% N_2 and 50% CH_4 by volume mixture at room temperature. The spectra for the unchirped pump/Stokes (0-0) and moderately chirped pump/Stokes cases are shown. The OPA is tuned to so that the pump-Stokes central frequency difference is 2300 cm^{-1}.

In this study, we investigated the effects of moderate frequency chirp for the pump and Stokes pulses on CPP fs CARS temperature measurements. The effects were investigated both theoretically, by computing the CPP fs CARS spectra by solution of the time-dependent density matrix equations, and experimentally by inserting disks of SF11 glass in the beam paths of the CARS input beams. A major conclusion of the study is that transmission of the beams through thick glass windows will not significantly affect temperature measurement accuracy and precision. One major effect of moderate pump/Stokes chirp is that the spectrum of the nonresonant background narrows significantly, and the influence of the nonresonant background spectrum can be minimized in the temperature sensitive region of the spectrum. The envelope of Raman excitation efficiency also narrows due to moderate pump/Stokes chirp, and this effect must be incorporated in phenomenological models used to fit CPP fs CARS spectra. This narrowing of the Raman excitation

envelope may be used to advantage to minimize interferences in CARS spectra of target species due to CARS signals from neighboring species.

CHAPTER 6. SELF-PHASE MODULATION (SPM) EFFECTS ON CPP FS CARS

The effects of self-phase modulation (SPM) on the power spectra of fs pulses and the consequent impact on N_2 chirped-probe-pulse (CPP) fs coherent anti-Stokes Raman scattering (CARS) spectra are discussed. We investigated the pressure dependence of CPP fs CARS for N_2 in a room-temperature gas cell at pressures ranging from 1 to 10 bar, and in our initial experiments the spectrum changed drastically as the pressure increased. We found that the spectra of the near-Fourier-transform-limited, 60-fs pump and Stokes pulses at the exit of the gas cell changed drastically as the pressure increased due to self-phase-modulation (SPM). We examined this effect in detail in further experiments where the pulse energies of the pump and Stokes pulses were controlled using a combination of a half-wave plate and a linear polarizer. Along with the generated CARS spectrum, the spectra of pump and Stokes pulses were measured at the entrance and exit of the gas cell. The extent of SPM effects for a particular spectrum was characterized by the least squares difference between that spectrum and a spectrum recorded at low enough pressure and laser intensities that SPM was negligible. SPM effects were investigated for N_2, O_2, CO_2, and CH_4, for pressures ranging from 1 to 10 bar, and for pump and Stokes pulse energies ranging from 10 to 60 μJ. We found that SPM effects in N_2 were much weaker than for O_2, CO_2 and CH_4.

6.1 Theoretical Background of SPM

Self-phase-modulation, also known as non-linear Kerr-like effect is a phenomenon in which an ultrashort pulse accumulates nonlinear phase as it propagates through a gas medium[85]. This nonlinear phase accumulation depends on the intensity profile of the laser pulse and the nonlinear refractive index of the gas. In Nibbering's study, the nonlinear refractive index was measured for N_2, O_2 and Ar, in near atmospheric pressures (up to 1.6 bar), by recording the power spectrum of the transmitted pulses[88]. For diatomic molecules like N_2, there are in general two contributions of the nonlinear phase, as shown in Eq. (6.2), the pure rotational contribution ($\phi_{NL,rot}$) and the electronic contribution ($\phi_{NL,elec}$)

$$E(t,z) = E(t,0)\exp\left[i\phi_{NL}(t,z)\right] \tag{5.1}$$

$$\phi_{NL}(t,z) \propto \phi_{NL,elec} + \phi_{NL,rot} \tag{5.2}$$

The electronic part of the nonlinearity arises from the bound electrons of the molecule, and the magnitude follows the intensity profile of the electric filed

$$d\phi_{NL,elec} = n_{2,elec} I(t,z)\, dz \tag{5.3}$$

The pure rotational Raman contribution is time-delayed and can be related to molecular properties through

$$d\phi_{NL,rot} = \mathrm{Im}\left[n_{2,rot} \sum_{J=0}^{\infty} F_J \times \int_0^{\infty} I(t-\tau,z) \exp(-i\omega_J \tau)\, d\tau \right] dz \tag{5.4}$$

In Eq. (5.4), $n_{2,rot}$ describes the magnitude of the rotational nonlinear refractive index, F_J takes into account the relative magnitude of the different possible rotational transitions, and ω_J denotes the rotational transition frequency. The time development of the pure rotational polarization causes an effective delayed response of the nonlinearity in time domain. The delayed response causes the spectral components of the power spectrum to shift towards longer wavelengths whereas, the instantaneous response results in a homogeneous broadening of the optical spectrum. The pressure dependence of the nonlinear refractive index was measured by Börzsönyi et al. [136] for pressures up to 1 bar. It was found that, for these pressures, the nonlinear refractive index was approximately proportional to pressure for several inert gases such as N_2 and Ar.

In Eq.(5.3) and Eq.(5.4) the nonlinear phases are written in their differential forms, the overall nonlinear phase accumulation needs its spatial integration over the optical path inside the gas cell. For collimated beam, this spatial integration will be straightforward as only the laser electric field characterization at $z = 0$ is needed (i.e., $I(t,0)$). As for our experiment, laser beams were focused at the probe volume in order to generate the fs CARS signal, the spatial integration will need to take into account the laser intensity profile variation along propagation ($\phi_{NL}(t,z) \propto \int_0^z I(t,z')\, dz'$). When the frequency dispersion inside the gas medium is negligible (as is in our case), the time and the spatial laser intensity characterization can be separated [92].

$$I(t,z) = f(t) \frac{2P}{\pi w(z)^2} e^{-2r^2/[w(z)]^2} \tag{5.5}$$

In Eq. (5.5), $f(t)$ denotes the temporal envelope of the pulse and P is the laser power, $w(z)$ is the $1/e^2$ beam waist size, in the following discussion, we consider only on-axis laser intensity and

neglect the radial distribution. Assuming further for Gaussian-shape pulse, we can substitute Eq.(5.5) back to Eq. (5.3) and Eq.(5.4) and the spatial integral indicates that

$$\phi_{NL}(t,z) \propto \int_0^z I(t,z')dz' = f(t)\frac{2P}{\pi w_0^2}\int_0^z \frac{1}{1+\left(\frac{z}{z_R}\right)^2}dz' = f(t)\frac{2Pz_R}{\pi w_0^2}\arctan(z/z_R) \qquad (5.6)$$

where z_R is the Rayleigh range and is usually in the magnitude of few millimeters. From Eq.(5.6) and Figure 6.1 we can also concludes that the accumulation of SPM is mostly around the probe volume, especially at high pressure conditions where SPM will be significant. At 1 bar pressure, however, the amount of nonlinear phase accumulated on glass windows is about 1/4 of the overall nonlinear phase generated.

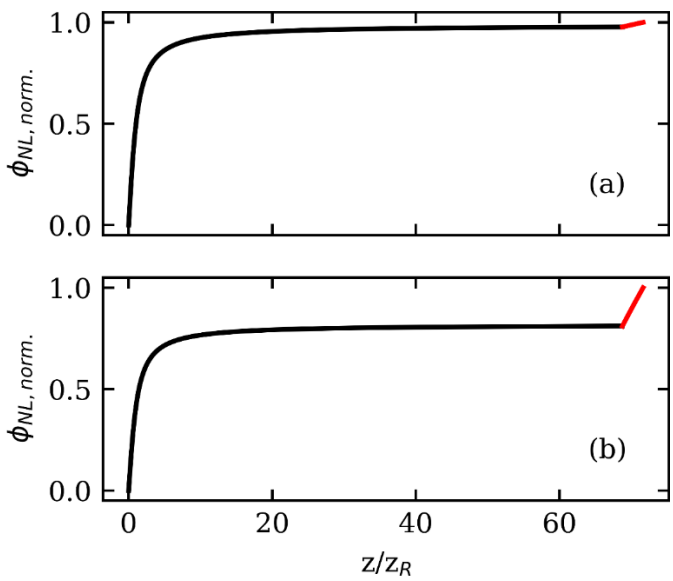

Figure 6.1. Accumulated nonlinear phase (normalized) as the pulse propagates through the gas cell (only halfway of the optical length is considered since the focusing geometry is symmetric at the probe volume). The red line at the end of the curve is because of the nonlinear phase accumulated on the cell windows. The simulation was evaluated at (a) 10 bar pressure and (b) 1 bar pressure, the nonlinear refractive index information for fused silica windows was taken from literature [82].

6.2 SPM on Laser Spectrum

The SPM due to the glass windows was accounted for by measuring the pump and Stokes optical spectra before and after the gas cell that is at atmospheric pressure. SPM in pure N_2 was evaluated by measuring the optical spectrum of the 800 nm Stokes pulse transmitted across the high-pressure cell with different cell pressures. Two laser energy settings were displayed for comparison, the recorded power spectrum was shown in Figure 6.2. For the low laser energy case (10 μJ per pulse), the recorded optical spectra are relatively unchanged throughout the pressure range being investigated. As expected, for the high laser energy case (60 μJ per pulse), the spectral components of the pulse tend to shift toward lower frequencies at higher pressures and the overall modulated spectrum is more asymmetric when the SPM is significant. We note that the presence of a second beam (for example, the presence of pump beam when measuring the SPM of Stokes beam) did not influence SPM induced in the first beam, which indicates the cross phase modulation is not a major concern in the context of this work.

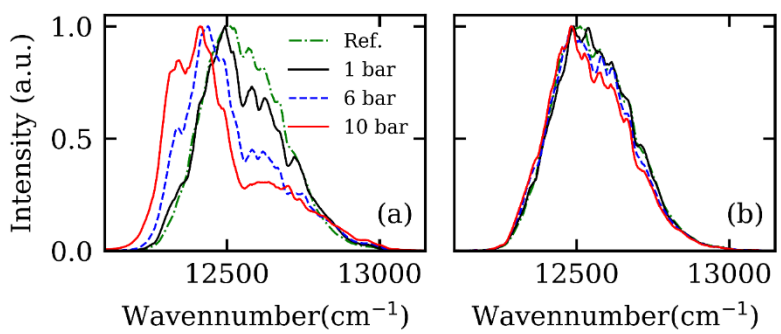

Figure 6.2. (a) Optical spectra of the Stokes pulse after the high pressure cell, recorded at various pressures with a) 60 μJ per pulse and (b) 10 μJ per pulse The peak intensity corresponding to the 10 μJ pulse, at the probe volume, is estimated to be on the order of 10^{16} W/m^2.

Similarly, we measured the self-modulated optical spectrum in pure CO_2, O_2 and CH_4. This study is of practical interest because for many high-pressure combustion applications, the local mole-fraction of those gaseous species, at the probe volume, can be comparable or even greater than N_2. Also, we plan to investigate oxy-fuel flames, where we will need to measure these species. A brief summary is given here, O_2 has both higher rotational and electronic contribution of nonlinear refractive index than N_2, thus it exhibited similar but more obvious spectral modulation

as compared to N_2. CO_2 has a much stronger rotational Raman cross section than N_2 and O_2 [124], as a result, its spectral component shifts toward lower frequency more significantly at high pressures. Another interesting fact is that since CH_4 does not have any rotational Raman transitions, the SPM is solely due to the electronic contribution of the nonlinear refractive index. As shown in Figure 6.2b, the self-modulated optical spectra of CH_4 exhibited only homogeneous broadening with negligible frequency shift. Thus, suppression of SPM is desirable, especially, when multiple gaseous species are expected at the probe volume.

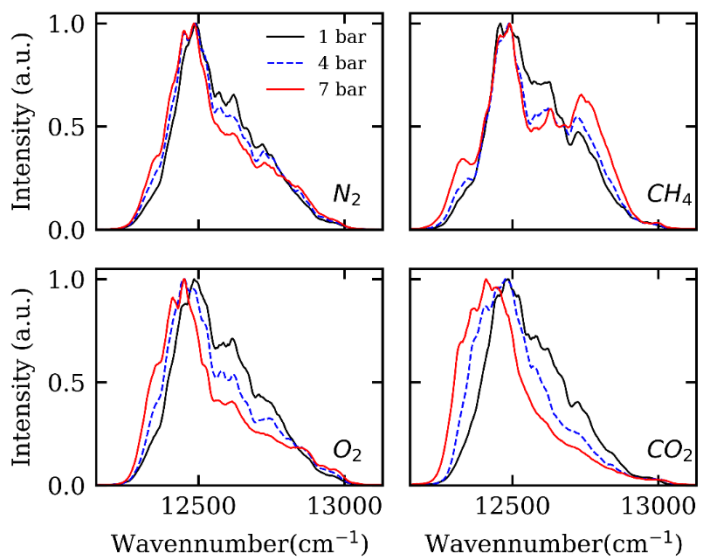

Figure 6.3. Self-modulated optical spectra in different gaseous species. The Stokes optical spectra was measured after the high pressure cell, laser energy was 40 μJ per pulse. Notice the large and negligible red-shift in the CO_2 and CH_4 spectra, respectively.

6.3 Evaluation of the Extent of SPM

To the best to our knowledge, nonlinear refractive index information for gaseous species like N_2 at elevated pressures is not available in literature. We propose an alternative way to characterize SPM, as shown in Eq.(6.7), by calculating the least squares difference between the modulated spectral intensity $S(\omega)$ and spectral intensity $S^0(\omega)$ recorded at low enough pressure and laser intensities that SPM was negligible. Both $S(\omega)$ and $S^0(\omega)$ are normalized such that the peak spectral intensity value is 1.0.

$$\Delta SPM = \int \left[S(\omega) - S^0(\omega) \right]^2 d\omega \tag{5.7}$$

The results are shown in Figure 6.4, not surprisingly, N_2 has least amount of SPM while CO_2 has strongest SPM effects for the gaseous species tested. For all the gaseous species being investigated, the SPM effects become increasingly significant at higher laser energies and high pressures.

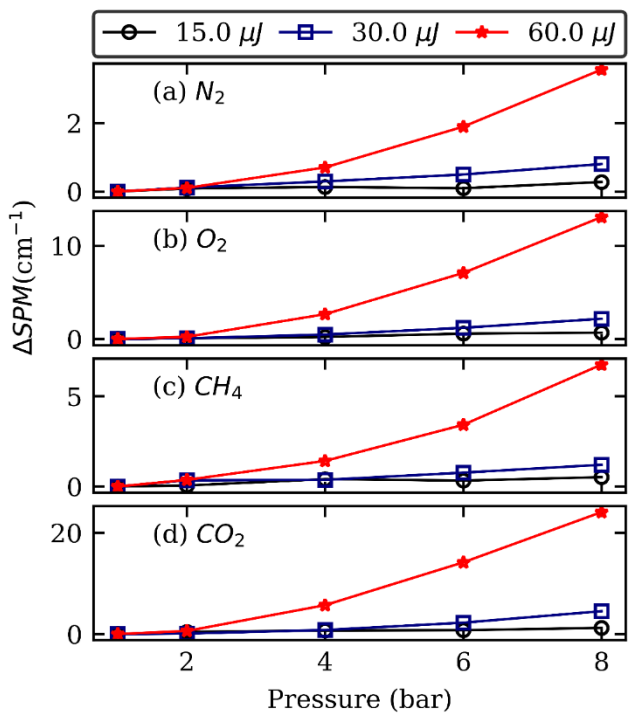

Figure 6.4. Evaluation of effect of SPM extent on the modulated optical spectra for different gaseous species

The time domain electric filed function $E(t,0)$ can be obtained from the inverse Fourier transform of $\sqrt{S(\omega,0)}$ if the spectral phase is specified. According to Eq.(5.1), we can even simulate the post cell optical spectrum $S(\omega,L)$ if the nonlinear phase $\phi_{NL}(t,L)$ was also known in prior. Vice versa, we can actually determine $\phi_{NL}(t,L)$ from the experimentally measured spectra $S(\omega,L)$ and $S(\omega,0)$.

In practice, we allowed $n_{2,elec}$, $n_{2,rot}$ and the quadratic spectral phase to be varied to obtain the best theoretical fit to the SPM spectrum $S(\omega, L)$ based on the pre-cell, unmodulated power spectrum $S(\omega, 0)$. The linear and cubic spectral phase were not included since the former only corresponds to a temporal shift and the latter is negligible for pump and Stokes beams. A spatially averaged laser intensity of about 2.3×10^{15} W/m^2 was used in the simulation according to analyses shown in Eq.(5.3) to Eq.(5.6). A summary of the fitting results is as shown in Figure 6.5, the fitted power spectrum matches satisfactorily with the experimental data. The magnitude of $n_{2,elec}$ and $n_{2,rot}$ obtained from the Stokes pulse spectral fitting at different pressures were normalized to the fitted nonlinear refractive index obtained at 2 bar and were as shown in Figure 6.6.

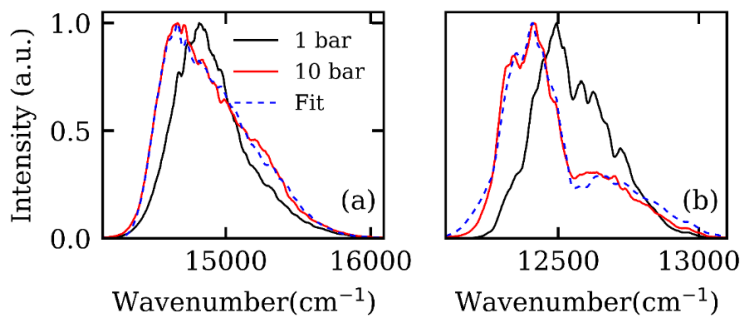

Figure 6.5. Fitted optical power spectrum through SPM simulation as compared to the experimental measurement. (a) For pump pulse. (b) For Stokes pulse.

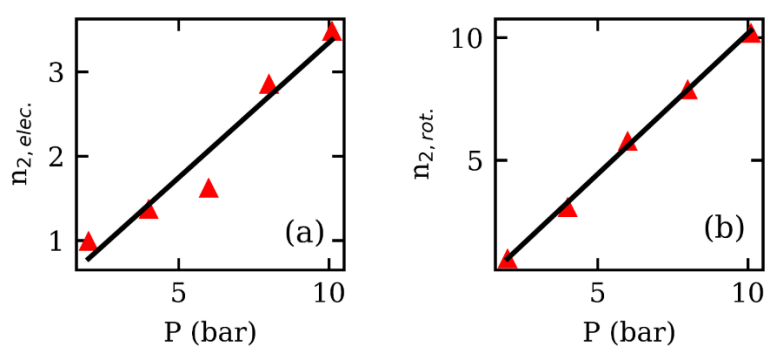

Figure 6.6. Normalized electronic (a) and rotational (b) contribution of the nonlinear refractive index as determined from the SPM spectral fitting. Linear correlation was found between the magnitude of nonlinear refractive index and the pressure. Stokes pulse energy was 60 μJ.

6.4 SPM on CPP Fs CARS Spectrum

As shown in Figure 6.7, for high laser energy settings (60 μJ per pulse), the CARS spectrum variation is much more evident than for the low energy case (10 μJ per pulse). Spectral distortion of the nonresonant signal, is evident, near 14600 cm^{-1} to 14800 cm^{-1} at 10 bar pressure, as can be correlated with the SPM pattern of N_2 as shown in Figure 6.2. One can observe slight spectral modulation of the CARS signal for the 10 μJ per pulse energy case. This may be attributed to the wavelength dependence of the linear refractive index of N_2. According to Lorenz-Lorenz equation, the linear refractive index difference of N_2 at 675 nm and 800 nm can be approximated to scale linearly from 1 to 10 bar [137] (higher refractive index at 675 nm). The optical path length of the pump and Stokes pulses inside the high pressure cell is about 370 mm, which leads to Stokes pulse being delayed by as much as 10 fs, relative to the pump beam, as the pressure was increased from 1 to 10 bar.

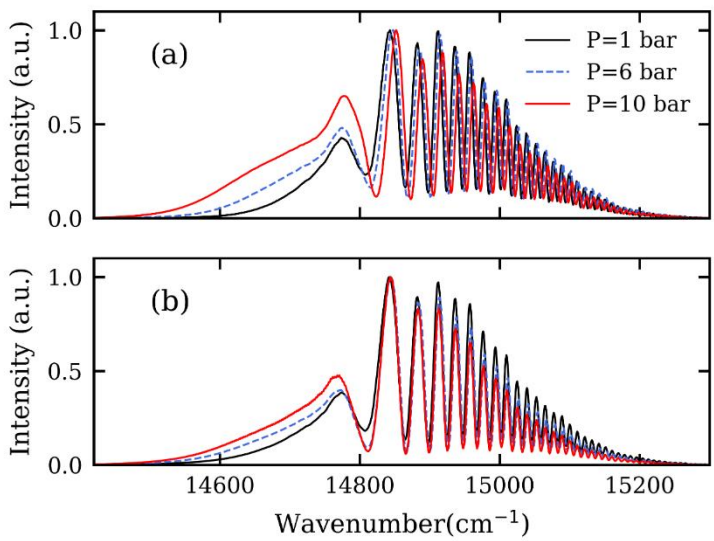

Figure 6.7. (a) Experimental CPP fs CARS spectra with high laser energy setting (pump and Stokes both with 60 μJ per pulse energy), spatial averaged peak intensity near probe volume is about $5x10^{17}$ W/m^2 (b) Low laser energy setting (10 μJ per pulse energy), peak intensity near probe volume is about $9x10^{16}$ W/m^2

To better identify the effects of SPM on pump and Stokes pulses, and on the CPP fs CARS spectrum, we can vary the laser intensity of only one laser pulse while keeping another laser intensity unchanged. As shown in Figure 6.8, for high pressure, with high Stokes energy, the Stokes

pulse spectra will start ‘red shift’ as indicated in Figure 6.2, thus, the CPP fs CARS spectrum will shift towards ‘blue frequency’ as a consequence of pump and Stokes convolution.

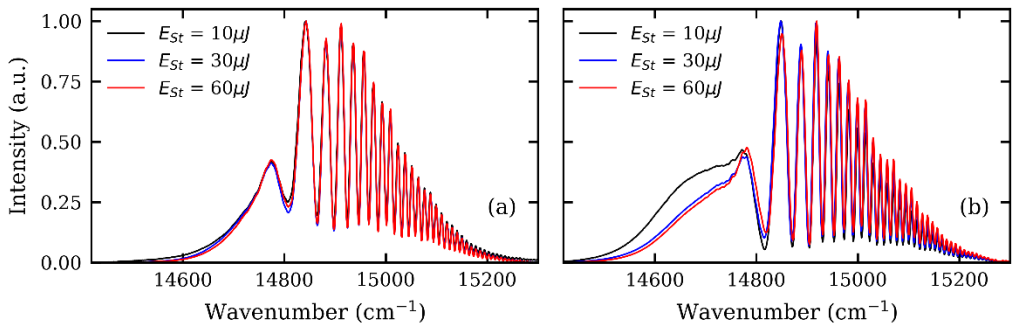

Figure 6.8 CPP fs CARS spectrum with 60 μJ per pulse energy pump energy and varying the Stokes pulse energy. (a) For atmospheric pressure and (b) for 10 bar pressure.

Using the optical spectra of the pump and Stokes pulses recorded at 1 bar, we can fit the CPP fs CARS spectrum recorded at low laser energies. A comparison of the fitted CARS spectrum and the experimental spectrum taken at 10 bar at lower energy is shown in Figure 6.9. The embedded figure shows the change of the fitted Stokes time delay for pressure increasing from 1 to 10 bar. In general, the theoretical spectrum is in good agreement with the experimental spectra. The trend of the linear delay of Stokes beam, with increasing pressures, matches with the fitting code prediction. However, the fitting code exhibits a best fit of value for the Stokes delay of 20 fs from 1 to 10 bar rather than the 10 fs calculated from the dispersion of the refractive index. This may indicate residual SPM effects even for low laser energies.

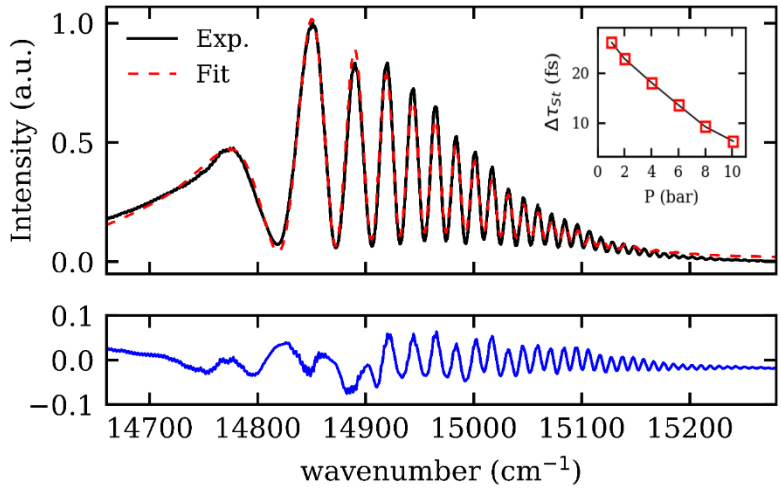

Figure 6.9. Fitted CPP fs CARS spectra at 10 bar condition as compared to the experimental data when 10 μJ per pulse energy was used for both pump and Stokes pulses. The fitting residual was displayed below the CPP fs CARS spectra. Embed: Fitted value of the Stokes delay at various pressures, relative Stokes delay reduces from about 25 fs to about 5 fs from 1 to 10 bar pressure. In the spectral fitting routine, only phase angle, resonant scaling factor and relative pump and Stokes delay were allowed to vary while all the rest of the laser parameters were fixed the same as they were extracted at 1 bar pressure.

Efforts were also made to fit the CPP fs CARS spectra for the high laser energy settings by using the optical spectra measured before or after the high-pressure cell. As shown in Figure 6.10a and Figure 6.10b, the fitting accuracy is much worse as compared to low energy case. This is because when SPM is significant, neither of the optical spectrum recorded before or the optical spectrum recorded after the test cell does not give satisfactory approximation of the pulse spectrum at the probe volume. For the pure N_2 measurement condition, better fitting accuracy can be obtained by simulating the SPM inside the high pressure cell as was discussed in previous section and as it was shown in Figure 6.5. For example, once the overall nonlinear phase $\phi_{NL}(t,z)$ was determined, we would assume $\phi_{NL}(t,z/2) \approx \phi_{NL}(t,z)/2$ at the probe volume, this was a reasonable assumption when we consider the symmetric focusing geometry, the corresponding power spectrum can then be interpolated from Figure 6.2. The CARS fitting results obtained from interpolated power spectrum are summarized in Figure 6.10c. The fitting accuracy is obviously better than the CARS fitting as shown in Figure 6.10a and Figure 6.10b.

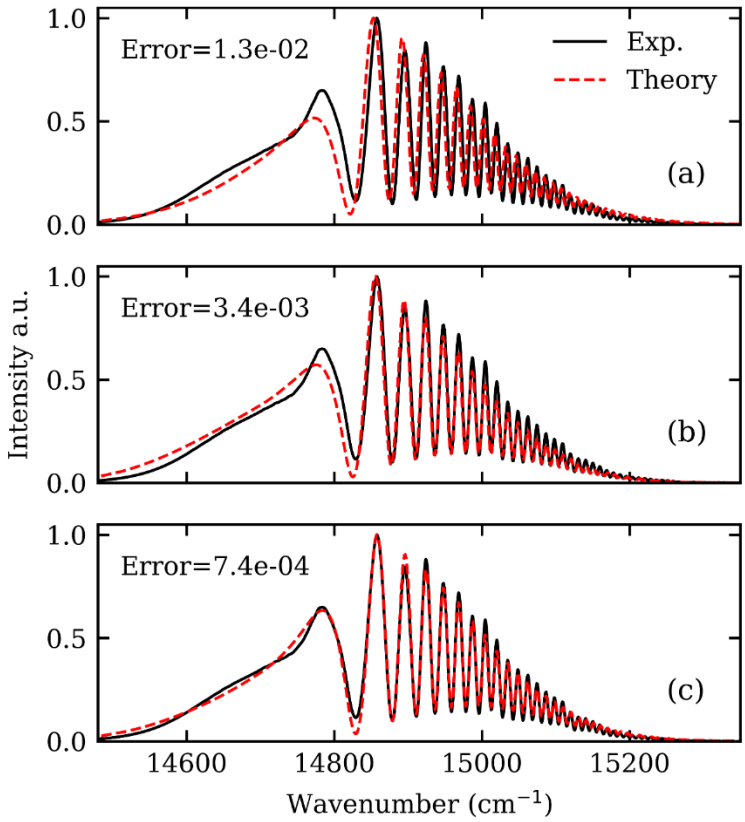

Figure 6.10. With 60 μJ per pulse energy, fitted CPP fs CARS spectrum as compared to the experimental measurement at 10 bar. (a). Using the optical spectra recorded before the gas cell. (b) Using the optical spectra recorded after the gas cell. (c). Using the power spectra interpolated through SPM fitting. The laser parameters were kept the same for all three cases.

6.5 Conclusions

We have investigated the effects of SPM at high pressures and with varying laser energies, on the power spectrum of fs pulses employed in CARS measurements and on the CPP fs CARS spectrum. We found that with sufficiently high laser energy, SPM can become significant and result in modulation of CPP fs CARS spectra even at moderate pressures. We also measured SPM effects for several different gaseous species including CO_2, O_2 and CH_4, it was found that N_2 exhibits least amount of SPM while CO_2 has strongest SPM among those molecules being studied. This indicates that SPM may affect CPP-fs-CARS spectra if there is significant CO_2 in the probe volume, even at atmospheric pressure. Also, we conclude that it will be preferable to eliminate SPM effects by reducing the laser intensity rather than to try to incorporate it into the CARS modelling since its influence can be much more complex and even intractable especially when several gaseous species

are to be involved. This work is meaningful not only for the study of CPP fs CARS measurements but also for all the other ultrafast spectroscopic studies at high pressure conditions, especially when the laser beams need to be focused or if the optical path inside the high pressure chamber is significant. So far, our measurements were conducted in room temperatures and within moderately high pressures (1-10 bar). In future work, we will extend our investigation of SPM to higher pressures (up to 50 bar) and higher temperatures. As SPM depends on the number density other than absolute pressure of the gas medium, we would expect that high temperature measurement could be beneficial in terms of eliminating the SPM influence.

CHAPTER 7. CO_2-O_2 CPP FS CARS THERMOMETRY

N_2 is frequently used as target molecules for CARS measurements because of their relative abundance in combustion applications and because of their simple molecular structure. The CARS spectra of O_2 and triatomic molecules such as CO_2 are also important especially for oxy-fuel combustion studies [138-141] as well as in gasification processes [142]. The purpose of this study is to investigate the theoretical modelling and experimental applicability for CO_2-O_2 CARS for thermometry measurement.

7.1 CO_2 CPP Fs CARS Modelling

A linear triatomic molecule like CO_2 has three vibrational modes that are quantized by vibrational quantum number ν_1 (symmetric stretch), ν_2 (degenerate bending) and ν_3 (antisymmetric stretch). For the doubly degenerate bending mode ν_2, an extra angular momentum quantum number l is needed to further specify the quantum state. For CO_2, the unperturbed vibrational frequency $\nu_1 \approx 2\nu_2$. This gives rise to the Fermi-resonance effects in which the perturbed vibrational level energies are determined by the superposition of the wave functions of the two unperturbed modes. The ν_3 mode is not vibrationally Raman active since the first order derivative of the Raman polarizability along the vibrational axis is zero.

Following the phenomenological model developed for N_2 CPP fs CARS studies, the resonant polarization of CO_2 fs CARS process can be modeled through [41]

$$P_{res}(t) = \beta\left[\int_{-\infty}^{t} E_p(t')E^*_{St}(t')dt'\right] \times \sum_i \left\{\left(\frac{d\sigma}{d\Omega}\right)_i \cos(\omega_i t + \varphi)\exp(-\Gamma_i t)\right\} \tag{6.1}$$

where E_p and E^*_{St} denote the electric field amplitudes, ω_i is the transition frequency, and φ is the time-independent phase difference between the resonant and nonresonant polarization. The parameter Γ_i is the dephasing coefficient, which can be determined through the rotational collisional model as proposed by Lavorel et. al [97]. The Boltzmann population distribution is incorporated into the definition of Raman cross section according to convention of Tejeda et al. [101] as

$$\left(\frac{d\sigma}{d\Omega}\right)_{v\to v'} = \left(\frac{\pi}{\varepsilon_0}\right)^2 \frac{\left(v_0 + v - v'\right)^4}{Z\left(T\right)} g_v g_J \left(M_{vJ\to v'J'}\right)^2 \exp\left(-Av/T\right) \tag{6.2}$$

The depolarization ratio for CO_2 at 1388 cm^{-1} is 0.027, thus, we consider that Q branch transitions ($\Delta J = 0$) are dominant in the CARS process [100]. To the best to our knowledge, the *J*-dependent Raman cross sections are not known with sufficient detail. Therefore, we assume identical Raman cross sections for Q-branch transitions within each vibrational manifold. This is a reasonable assumption in vibrational CARS studies because the frequency difference among *Q* branch transitions is small as compared to the laser bandwidth. The vibrational frequencies v and v', and the vibrational and the rotational degeneracies g_v and g_J can be found in the literature [96]. The transition dipole moments $M_{vJ\to v'J'}$ for the different vibrational transitions were extracted from the tabulated data of Lemus et al. [99]. For CO_2, with increasing temperatures, a large number of vibrational levels must be included.

The effects of different PTDs on CO_2-O_2 CPP fs CARS can be understood by simulating the time evolution of the resonant polarizations of both species. Figure 7.1 compares the normalized amplitudes of the resonant polarization signals for CO_2 and O_2. The simulated resonant polarization signal of O_2 decays much faster than for CO_2 because of greater line spacing amongst *Q* branch transitions. This becomes even more obvious at higher temperatures where more ro-vibrational level populations are excited. The modulation pattern of CO_2 polarization at room temperature occurs because of the heterodyning of the CO_2 Fermi resonances. Also, as shown in Figure 7.1, the modulation pattern of CO_2 resonant response varies strongly with temperature. This indicates the potential for accurate temperature measurements using CO_2 CPP fs CARS.

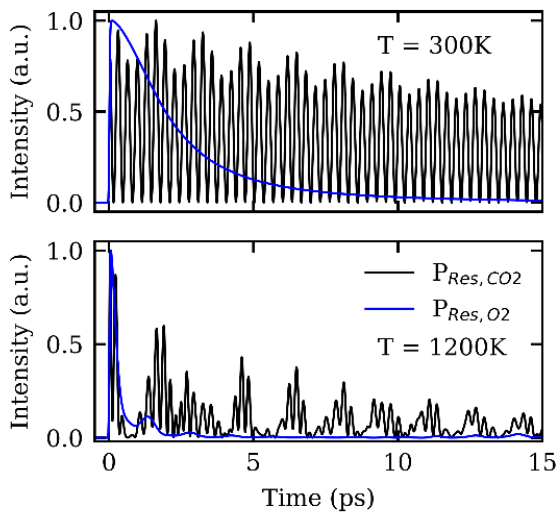

Figure 7.1 Simulated resonant polarization signals for CO_2 (black solid) and O_2 (blue solid) at 300K and 1200K. The modulation pattern in the resonant CO_2 spectrum is due to heterodyning between the Raman active symmetric stretch mode ν_1 and the bending mode $2\nu_2$.

7.2 CO_2 Concentration Measurement

CPP fs CARS spectra were first obtained at room temperature with varying CO_2/O_2 concentrations. The collisional time scale for CO_2 vibrational transitions, at room temperature and 1 bar, is on the order of few hundred picoseconds [17]. Therefore, the influence of collisions is negligible within the range of PTDs investigated in this work. Figure 7.2 shows a comparison between CPP fs CARS spectra for relative O_2/CO_2 concentration of 20%/80% (black solid) and 70%/30% (blue solid), respectively, for two different PTDs.

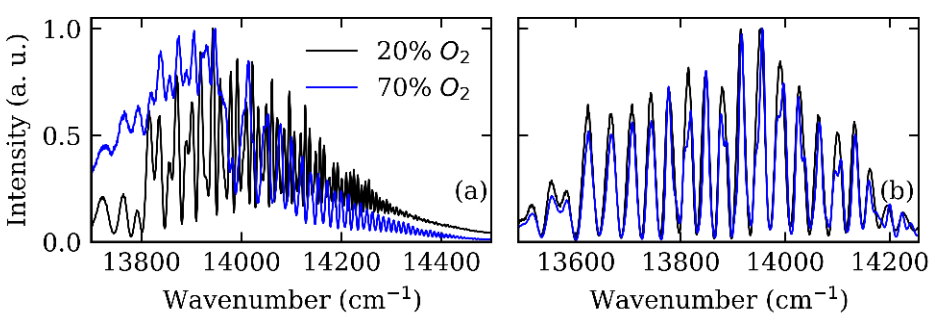

Figure 7.2 CO_2-O_2 CPP fs CARS spectra recorded at room temperature in O_2/CO_2 binary gas mixtures, for PTDs of (a) 0 ps, (b) 9 ps

For short PTDs, a change in the CO_2/O_2 concentration ratio significantly alters the interference pattern between CO_2 and O_2 spectra as well as the overall resonant/nonresonant interference pattern. This indicates that CO_2/O_2 CPP fs CARS, at a short PTD, is useful for CO_2/O_2 concentration measurements. Similar studies were performed by Richardson et al. [40] to extract relative concentration between N_2 and CO. For a PTD of 9 ps, on the other hand the O_2 interference is not evident for O_2 concentrations ranging from 20% to 70%.

Another interesting observation from Figure 7.2b is that at room temperature, the CO_2 CPP fs CARS spectrum is frequency modulated. This frequency modulation is different from the resonant/nonresonant modulation in N_2 CPP fs CARS studies because the nonresonant signal is suppressed by about 4-5 picoseconds of PTD. The frequency modulation in Figure 7.2b is related to the frequency difference of CO_2 Fermi resonances. In Figure 7.3, the blue dash and red dash represent the simulated CPP fs CARS spectrum for contributions from ν_1 and $2\nu_2$ modes only, while the oscillatory black curve is the overall resonant signal. Thus, the overall resonant signal is a result of heterodyning between the two resonant responses. With increasing temperatures, the heterodyne pattern also changes because more vibrational transitions are excited.

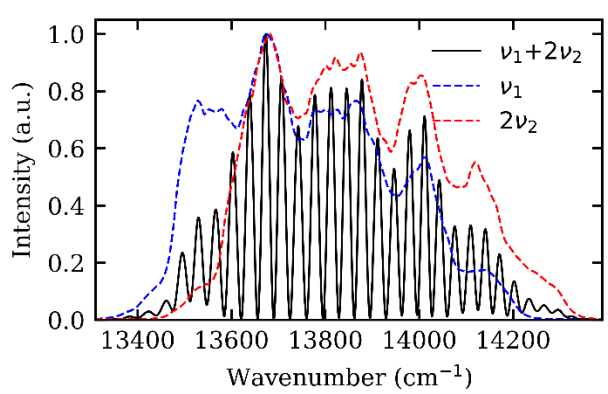

Figure 7.3. Simulated CO_2 CPP fs CARS spectrum at room temperature. The PTD was set to 9 ps in this simulation so that the CARS signal is dominated by the resonant contribution.

In previous CO/N_2 mixture experiments performed by Richardson et. al, the concentration information was associated with the fitted resonant scaling parameters of CO and N_2. Similarly, in this study, the spectral fitting results for the CO_2-O_2 CPP fs CARS spectrum are shown in Figure 7.4.

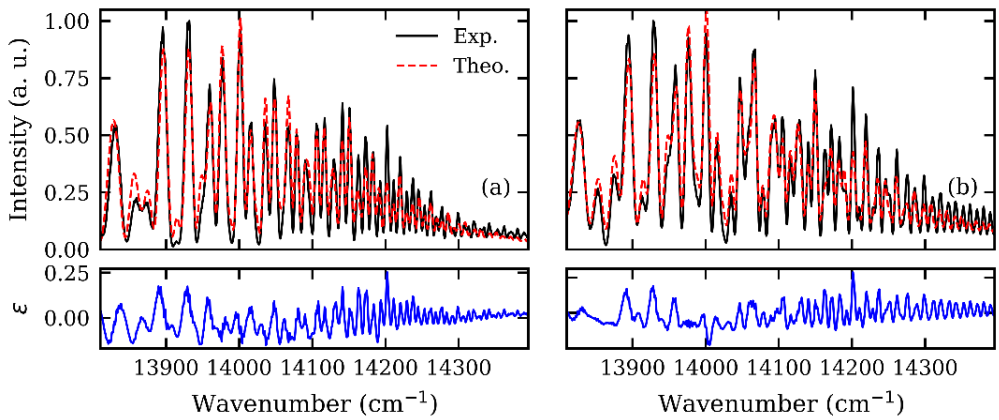

Figure 7.4 Comparison between experiment and theoretical calculations of CO_2-O_2 CPP fs CARS spectra for CO_2/O_2 binary gas mixtures at room temperature. The spectra are shown for concentrations of (a) 30% O_2, 70% CO_2 (b) 70% O_2, 30% CO_2. The PTD was 0 ps. The residuals are shown below.

Notice also for the previous discussion the measurement was performed for binary gaseous mixture of CO_2 and O_2 only. In practical combustion applications, there will be third party species such as H_2O, N_2, and CH_4. These species will not contribute to the resonant signal as the transition frequencies of those gaseous species are far from the transition frequency of CO_2. However, they will complicate the theoretical analysis for concentration measurements by affecting the overall nonresonant susceptibility. In general, for non-reacting binary gas mixtures the spectral fitting looks satisfactory.

Here we showed a brief theoretical treatment, which relates the CO_2 and O_2 mole-fraction to a simple scaling factor. C. Assuming that the resonant and nonresonant polarizations for each species scales linearly with its mole fraction ($P_{res,i} = \gamma X_i$, $P_{nonres,i} = \eta X_i$), we can write the resonant scaling factors β_{CO_2} and β_{O_2} as

$$\beta_{CO2} = \frac{\gamma_{CO_2} \cdot X_{CO_2}}{\eta_{CO_2} \cdot X_{CO_2} + \eta_{O_2} \cdot X_{O2} + \eta_0 \left(1 - X_{CO_2} - X_{O2}\right)} \tag{6.3}$$

$$\beta_{O2} = \frac{\gamma_{O_2} \cdot X_{O_2}}{\eta_{CO_2} \cdot X_{CO_2} + \eta_{O_2} \cdot X_{O2} + \eta_0 \left(1 - X_{CO_2} - X_{O2}\right)} \tag{6.4}$$

$$\frac{\beta_{O_2}}{\beta_{CO_2}} = \frac{\gamma_{O_2}}{\gamma_{CO_2}} \cdot \frac{X_{O_2}}{X_{CO_2}} \tag{6.5}$$

The ratio of the resonant scaling parameters between CO_2 and O_2 is a function of CO_2 and O_2 concentrations. In the case of a CO_2-O_2 binary mixture, we can further simplify Eq. (5) as

$$X_{O_2} = \frac{1}{1 + C \cdot \frac{\beta_{CO_2}}{\beta_{O_2}}} \tag{6.6}$$

The resonant scaling parameters β_{CO_2} and β_{O_2} can be obtained from the spectral fitting code. The relation between $\beta_{CO_2} / \beta_{O_2}$ and X_{O_2} is presented in Figure 7.5. The fitting curve is based on the relation shown in Eq.(6) while the only floating parameter is the species specific constant $C = \gamma_{O_2} / \gamma_{CO_2}$. The difference between the experimentally measured O_2 concentration and the theoretical calculation is in general less than ±10% (mostly within ±5%). Note also that the scaling parameter C will change as a function of temperature.

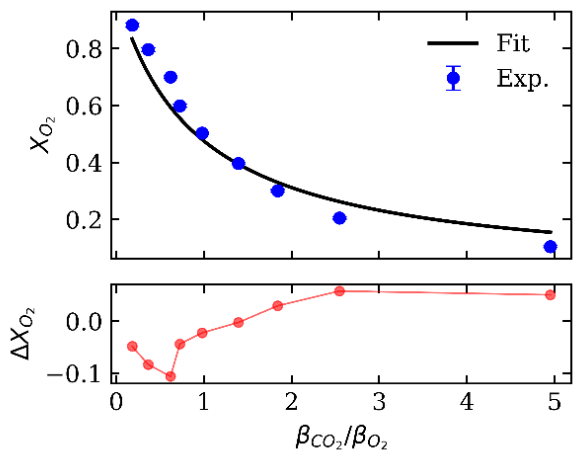

Figure 7.5 O_2 concentration as a function of the ratio of resonant scaling parameters between CO_2 and O_2. The fitted curve is based on Eq. (6), the residual is shown below

Efforts were made to investigate the capability of relative CO_2/O_2 concentration measurement when a third-party species is involved. The master equation is modified according to Eq. (6.5) as

$$\frac{X_{O_2}}{X_{CO_2}} = p_1 \frac{\beta_{O_2}}{\beta_{CO_2}} + p_0 \tag{6.7}$$

where p_1 and p_0 are the linear and zero order polynomial fitting coefficient. The experimental measurements were like the binary CO_2-O_2 gas case except N_2 was used as the buffer gas. Notice in Eq. (6.7), there is a fitting uncertainty regarding to the measurement uncertainty in X_{O_2} and X_{CO_2} especially when the values are small. More precisely, the concentration measurement uncertainty comes from the volumetric flow rate measurement as

$$X_{O_2} = \frac{V_{O_2}}{V_{O_2} + V_{CO_2}} \tag{6.8}$$

$$\sigma_{X_{O_2}} = \sqrt{\left[\frac{V_{CO_2}}{\left(V_{CO_2} + V_{O_2}\right)^2}\right]^2 \sigma^2{}_{V_{O_2}} + \left[\frac{V_{O_2}}{\left(V_{CO_2} + V_{O_2}\right)^2}\right]^2 \sigma^2{}_{V_{CO_2}}} \tag{6.9}$$

where V and σ denote the volumetric flow rate and the magnitude of uncertainty respectively. The flow rate uncertainty can be determined by experimental measurements and by accounting for the instrument function. According to the rule of propagation of uncertainty, the overall fitting uncertainty is specified as

$$\sigma_{X_{O_2}/X_{CO_2}} = \sqrt{\left[\frac{1}{V_{CO_2}{}^2}\right]^2 \sigma^2{}_{V_{O_2}} + \left[\frac{1}{V_{O_2}{}^2}\right]^2 \sigma^2{}_{V_{CO_2}}} \tag{6.10}$$

The fitting uncertainty was then used as weights in the fitting routine to reduce the bias. Accordingly, the relative fitted CO_2/O_2 concentration as compared to the experimental measurement was shown in Figure 7.6. Obviously, with the uncertainty-weighted fitting, the agreement between the experiment to the fitting curve is better for most of the data points. While the unweighted fitting has much larger error especially when CO_2 concentration is low

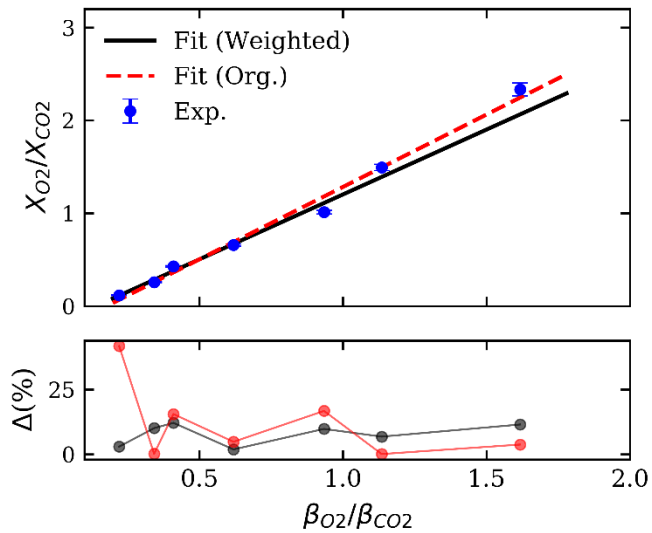

Figure 7.6 Relative O_2\CO_2 concentration as a function of the ratio of resonant scaling parameters between CO_2 and O_2. The fitting results from uncertainty-weighted fitting and unweighted fitting were both displayed.

7.3 Hencken Burner Flame Thermometry

Near-adiabatic hydrogen-air non-premixed flames, diluted with CO_2, were established using a Hencken burner. The flow rate of CO_2 diluent was fixed at 30% of the volumetric flow rate of air and the equivalence ratio ϕ was varied between 0.14 and 0.58. Assuming complete combustion, the CO_2 mole fractions in the combustion product were approximately 30% for all the flames investigated while the O_2 mole fraction decreased from 14% to 7% with increasing equivalence ratios. As discussed previously, the O_2 interference can be eliminated from the CO_2 CPP fs CARS spectrum with sufficiently long PTDs. The CO_2 CPP fs CARS measurements are compared against N_2 CPP fs CARS measurements for identical flame conditions. For the CO_2 CPP fs CARS measurements, we used PTDs ranging from 1.0 ps to 7.2 ps. For the N_2 CPP fs CARS measurements, a PTD near 1 ps was chosen since the N_2 CARS signal intensity decreased too much for longer PTDs. A comparison of the CO_2-O_2 CPP fs CARS spectra obtained at 630 K, 795 K and 1274 K for PTDs of 1.0 ps and 7.2 ps is shown in Figure 7.7. For the short PTD case (Figure 7.7a), satisfactory spectral fitting requires the inclusion of both CO_2 and O_2 resonant responses as well as the nonresonant background. However, for the 7.2 ps PTD case, only the resonant response of CO_2 is needed for reasonable spectral fitting. Thus, CO_2 thermometry will be uniquely advantageous in

flames with a large and unsteady non-resonant contribution such as in turbulent spray or sooty flames [143].

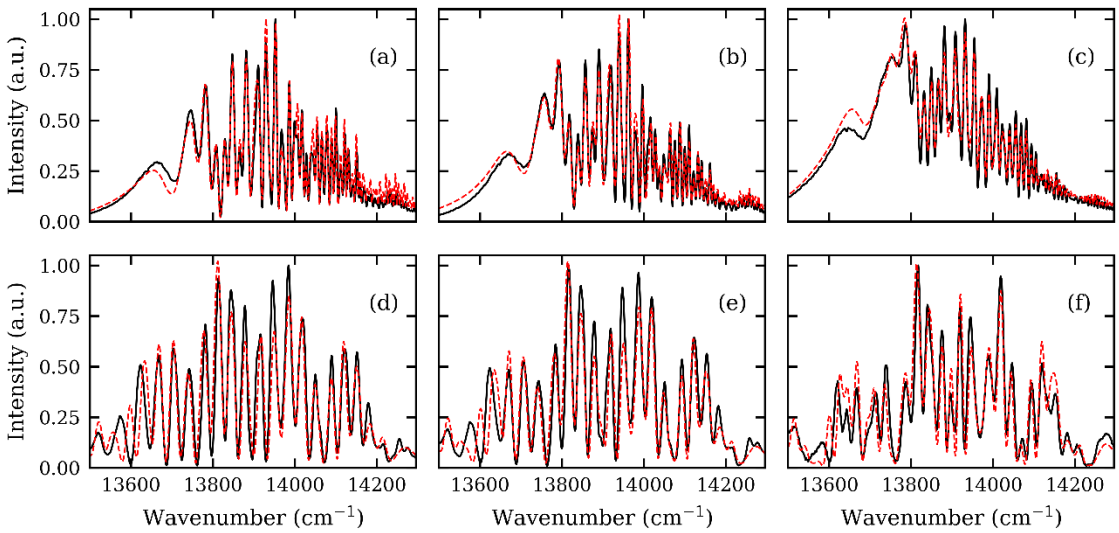

Figure 7.7 The comparison between the experimental (black solid) and theoretical calculation of the CO_2/O_2 CPP fs CARS spectrum obtained at several different flame conditions and PTD settings. The experimental data were all averaged over 2000 shots of measurements. (a), (b), (c): $\tau_{CPP} = 1.0$ ps, $T_{adb} =$ 630 K, 795K, 1274K; (d), (e), (f): $\tau_{CPP} = 7.2$ ps, $T_{adb} =$ 630 K, 795K, 1274K.

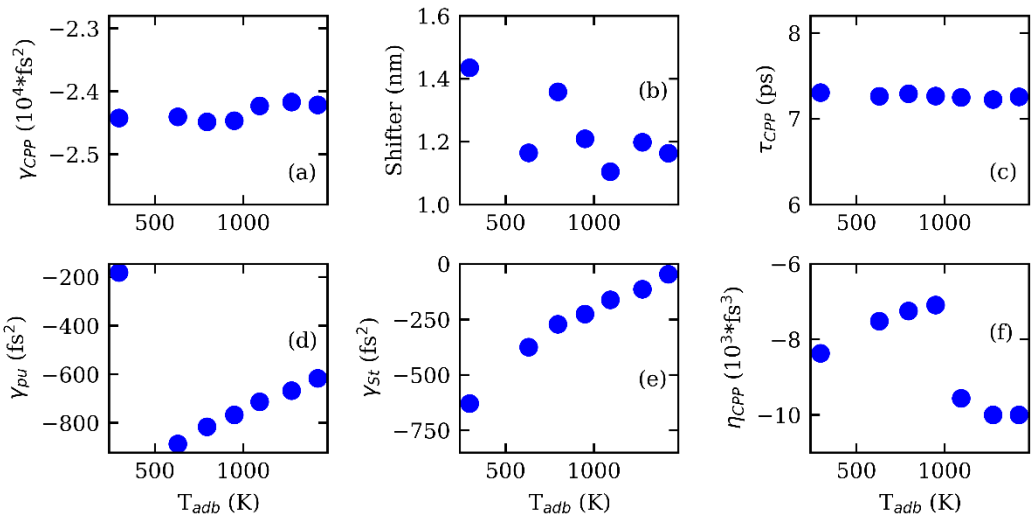

Figure 7.8. Sorted fitted laser parameters from the CO_2 CPP fs CARS measurements with PTD of about 7 ps. For each laser parameter, its value is compared among the spectral fitting results obtained from different flame conditions.

Figure 7.8 compares key laser parameters at various temperatures at a PTD of 7ps. Laser parameters such as quadratic phase of probe pulse and, PTD are quite consistent because those parameters are directly determined by the convolution between the probe electric field and the CO_2 resonant polarization response. While the fitted laser parameter such as Stokes delay and pump/Stokes quadratic phase varies significantly. This indicates that CO_2 CPP fs CARS signal, at long PTDs as compared to short PTDs, is less susceptible to variation in the Stokes delay. This is explained by the fact that the convoluted bandwidth between the pump and Stokes pulses (~400 cm^{-1}) is much greater than the frequency span of the CO_2 ro-vibrational transitions. Furthermore, since the nonresonant signal is suppressed at long PTDs, an uncertainty in Stokes delay does not affect the resonant-nonresonant modulation pattern. The aforementioned explanation can also be verified through Figure 7.9 which, shows the recorded CPP fs CARS spectrum at a PTD of 8.4 ps with varying Stokes delay.

We found that the detuning of Stokes delay over a moderate range affects only the absolute signal strength and does not affect the shape of the CPP fs CARS spectrum. Other laser parameters such as the quadratic spectral phase of pump and Stokes pulses, similar to the Stokes time delay, do not affect the shape of the CPP fs CARS signal within a moderate range of variability. This is explained by the fact that the convoluted bandwidth between the pump and Stokes pulses (~400

cm^{-1}) is much greater than the frequency span of the CO_2 ro-vibrational transitions. Furthermore, since the nonresonant signal is suppressed at long PTDs, an uncertainty in Stokes delay does not affect the resonant-nonresonant modulation pattern. Therefore, only 7 laser parameters are necessary to accurately fit the CO_2 CPP fs CARS at long PTDs while 12 laser parameters are needed to fit the spectra for shorter PTD cases. The discussion about the influence of fitted laser parameters on the calculated N_2 CPP fs CARS spectrum was reported elsewhere [41, 54]. This reduction of laser parameters for fitting CO_2 spectra at longer PTDs improves the numerical efficiency and the accuracy of the CARS spectral fitting code.

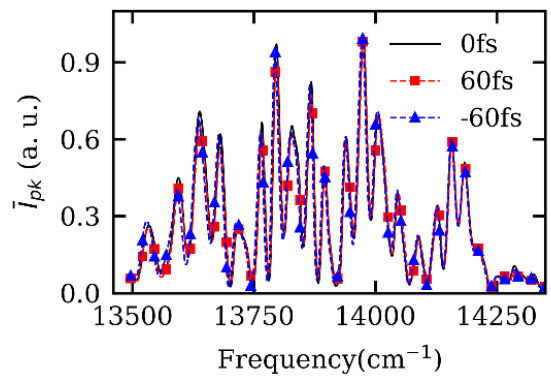

Figure 7.9 CO_2 CPP fs CARS spectrum with different Stokes delays. The probe time delay was about 8.4 ps and the adiabatic flame temperature was about 840 K

To investigate the use of the CO_2 CPP fs CARS technique for temperature measurements, we compared CO_2 CARS thermometry with N_2 CPP fs CARS thermometry. Figure 7.10 and Figure 7.11 show fits to the single-shot CO_2 and N_2 CPP fs CARS spectra, respectively. We first used the error-weighted fitting scheme to determine the flame temperature [42]. Briefly, each single-shot spectrum was fit using the laser parameters extracted from different calibration flames. The final temperature was determined based on the fitting errors from different laser parameters.

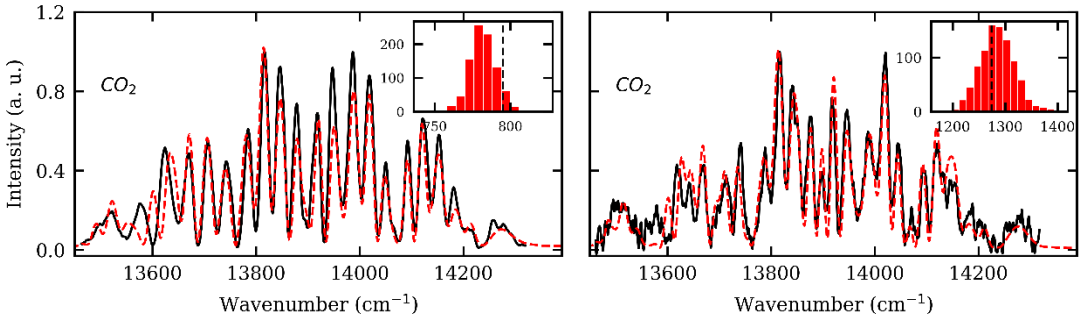

Figure 7.10 Comparison between the experiment and single shot fitting result for CO_2 CPP fs CARS spectrum obtained at adiabatic flame temperature of about 795 K (left) and 1274 K (right). For all the flame measurements, the concentrations of CO_2 and N_2 in the combustion product were about 30% and 53% respectively, the probe time delay was about 7.2 ps.

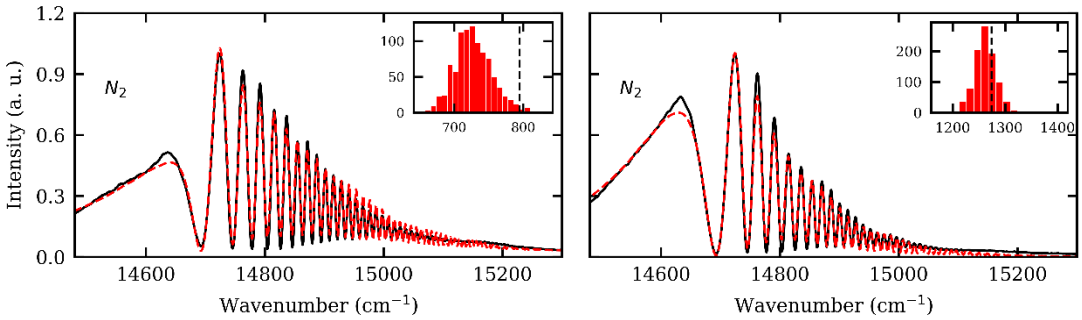

Figure 7.11. Comparison between the experiment and single shot fitting result for N_2 CPP fs CARS spectrum obtained at adiabatic flame temperature of about 795K (left) and 1274 K (right). The probe time delay was about 1 ps

Satisfactory single-shot spectral fits were obtained for both N_2 and CO_2 CPP fs CARS spectra. For the CO_2 CPP fs CARS spectrum, the slight disagreement between the theory and experiment at the low frequency end is attributed to an imperfect instrument response function for frequency to pixel mapping. Notice, in Figure 7.11, that for a flame temperature around 1300 K, the N_2 CPP fs CARS spectrum has a much better signal-to-noise ratio (SNR) as compared to the CO_2 CPP fs CARS spectrum. This is due to the abundance of N_2 in the combustion products and also because the nonresonant background contributes to the overall N_2 CARS signal strength. A more detailed summary of the flame thermometry obtained from N_2 CPP fs CARS and CO_2 CPP fs CARS measurements is shown in Table 7.1. In terms of the differences between the fitted temperature as compared to the adiabatic flame temperature, both techniques demonstrate good

temperature measurement accuracy. For low temperature measurements (below 1200 K), the performance of CO_2 thermometry is significantly better than N_2 thermometry. At lower temperatures, the temperature measurement precision for N_2 CPP fs CARS measurement is within 4%, while for CO_2 the measurement precision is close to 1% for temperatures below 1100 K. The precision of fs CARS CO_2 thermometry is probably limited by the flame stability of the Hencken burner [9]. This finding is consistent with our previous discussions that because CO_2 CPP fs CARS spectra with long PTDs are free of nonresonant interferences, and CO_2 has lower rovibrational transition frequencies, it will exhibit better temperature sensitivity than N_2 below 1000 K. The highest temperature in this study is limited by the degradation of SNR for CO_2 CPP fs CARS.

Table 7.1. Summary of the H_2-Air-CO_2 Hencken burner flame thermometry obtained from CO_2 and N_2 CPP fs CARS measurement at the same flame conditions. The probe time delay for CO_2 CPP fs CARS measurement was about 7.2 ps and the probe time delay for N_2 CPP fs CARS measurement was about 1.0 ps. 2000 single-shot measurements were summarized.

Performance of CPP-fs-CARS thermometry					
		N_2		CO_2	
Equiv. ϕ	$T_{ad.}$ (K)	$(T_{avg}-T_{ad.})/T_{ad.}$	σ/T_{avg}	$(T_{avg}-T_{ad.})/T_{ad.}$	σ/T_{avg}
0.14	630	-3.2%	2.8%	0.6%	1.1%
0.22	795	-8.9%	3.8%	-4.3%	1.2%
0.30	949	4.1%	3.5%	1.5%	1.1%
0.38	1093	6.8%	2.4%	-0.6%	1.4%
0.49	1274	-1.1%	1.6%	-0.5%	2.9%
0.58	1421	5.8%	1.6%	-5.3%	4.9%

For CO_2 CPP fs CARS with long PTDs, the suppression of the nonresonant signals and O_2 interferences obviates the necessity to include laser parameters such as resonant/nonresonant scaling factors into the single shot fitting code. Furthermore, the consistency of the CO_2 CPP fs CARS spectrum with variation in laser parameters such as Stokes delay, as shown in Figure 7.9, allows accurate CO_2 CPP fs CARS thermometry with a single set of laser parameters. A comparison of flame thermometry performed using different sets of laser parameters is shown in Figure 7.12. As expected, between 295 K and 1420 K, the extracted temperatures determined using different sets of laser parameters are nearly identical.

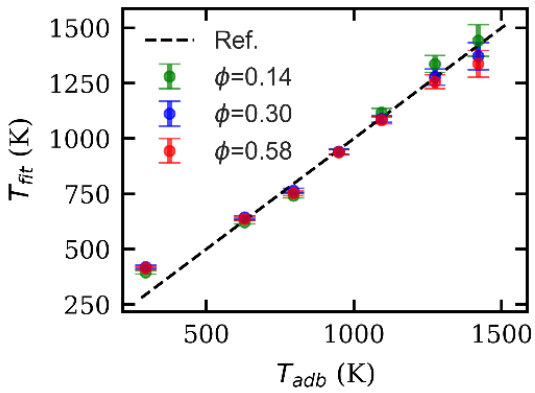

Figure 7.12 CO_2 CPP fs CARS thermometry obtained by using single set of laser parameters for spectral fitting. The laser parameters were obtained from different flame conditions with equivalence ratios of 0.14, 0.30 and 0.58 respectively

7.4 Conclusion

In this study, we have investigated the potential of CO_2 CPP fs CARS for flame thermometry. A phenomenological model of CO_2 CPP fs CARS was developed and was verified in various CO_2/O_2 mixtures as well as at different flame temperatures. Our model assumes that the CO_2 Q-branch Raman cross-section is independent of the rotational quantum number and only dependent on the specific vibrational mode. The aforementioned assumption was validated by the good spectral fits obtained for single-shot CO_2/O_2 spectra. We showed that at large PTDs one can suppress the O_2 resonant interference and the nonresonant signal interferences in the CO_2 spectrum. Therefore, the CO_2 CPP fs CARS spectrum obtained at long PTDs is dominated by the resonant contribution of CO_2. Comparison between flame thermometry obtained from CO_2 and N_2 CPP fs CARS measurements shows that CO_2 is well-suited for temperature measurements below 1200 K. Another advantage of CO_2 CPP fs CARS at long PTDs is that it enables accurate thermometry with only a single set of laser parameters. The consistency of the fitted flame temperatures with different sets of laser parameters indicate the accuracy of this technique for thermometry. The verification of the CO_2 model at higher temperatures, the improvement of the detection sensitivity, applications of CO_2 fs CARS thermometry to canonical flames and the extraction of CO_2/O_2 concentrations at flame conditions will be the focus of our future work.

CHAPTER 8. H_2 CPP FS CARS THERMOMETRY

We have shown CO_2 as a promising candidate for CARS diagnostics for oxy-fuel combustion studies. The limitation, however, is the inability to perform temperature measurement above 1800 K due to the lack of reliable CO_2 Raman polarizability information. (So far in this thesis, the highest temperature with accurate CO_2 CARS thermometry measurement is 1420 K.) Other common gaseous species that can be abundant in many oxy-fuel combustion applications include CH_4, H_2, and H_2O etc. The purpose of this study is to investigate H_2 for CPP fs CARS thermometry measurement so that we can have alternative options in high pressure combustion diagnostic studies.

8.1 Modelling of H_2 CPP Fs CARS

The modelling of H_2 CPP fs CARS is similar to N_2 CPP fs CARS. For H_2, due to the light molecular weight and much stronger rotational and vibrational coupling effects, the Herman-Wallis correction coefficient is more important than N_2 in terms of accurate CPP fs CARS modelling.

One of the most commonly used form of Herman-Wallis correction factor was proposed by James and Klemperer et. al[144]

$$F_{JK} = 1 - 3\gamma^2 J\left(J+1\right)/2 \tag{7.1}$$

parameter γ denotes the rovibrational coupling and can be given as

$$\gamma = 2B_e / \omega_e \tag{7.2}$$

where B_e and ω_e are the rotational and vibrational constant respectively. In Marrocco's study[145], F_{JK} was compared with other forms of Herman-Wallis factors in affecting the flame thermometry accuracy. A summary of those Herman-Wallis factors is shown in

Table 8.1 and Figure 8.1.

Table 8.1 Summary of the Herman-Wallis correction factors for H_2

Expression	Parameters for H2	Reference
$F_{JK} = 1 - 3\gamma^2 J(J+1)/2$	$\gamma = 0.02765$	James and Klemperer[144]
$F_{LBY} = \left[1 - 3\gamma^2 (a_1 + 1) J(J+1)/4\right]^2$	$a_1 = -1.6$	Luthe et. al[146]
$F_{TB} = 1 - \left[3(a_1+1)/2 - 4p_2/p_1\right]\gamma^2 J(J+1)$	$p_2/p_1 = 0.271$	Tipping and Bouanich[125]

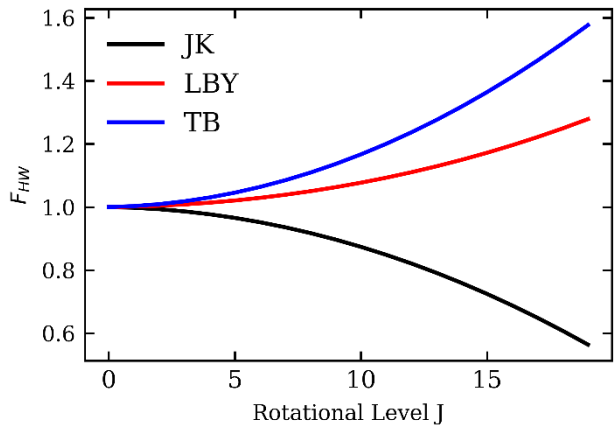

Figure 8.1 Comparisons of different forms of Herman-Wallis correction factors.

The differences among the three forms of Herman-Wallis correction factors are greater for higher rotational levels. In Marrocco's studies [145], the extracted flame thermometry was compared across temperature range from 300K to 3000 K when different forms of Herman-Wallis factors were applied. It was found that F_{TB} agreed best with the calibration temperature so it will be used in this thesis.

Another challenge for H_2 CPP fs CARS modelling is its linewidth model. Because of its low molecular weight, the Doppler linewidth can become comparable to its collisional linewidth even near atmospheric pressures. H_2 linewidth can be modelled as a summation of collisional linewidth and Doppler linewidth as[147]

$$\Gamma_J = \frac{2\pi D_0 \omega_J^2}{c\rho} + \rho\gamma_J \tag{7.3}$$

where $D_0 = 0.01176T^{0.8314}$ cm^2-amagat/s is the diffusion coefficient for H_2; ω_J is the transition frequency; c is the speed of light; ρ is the gas number density in amagat and γ_J is the collisional linewidth as described in previous chapters. It should be mentioned here that as best to our knowledge, the accurate experimental validation of the collisional linewidth for H_2 has only been reported up to Q(5) transition[148]. Thus in our treatment, for higher ro-vibrational transitions, the collisional linewidths are assumed to be identical to Q(5) transition.

One interesting aspect of H_2 CARS is that its rotational transitions are very well separated. This is alike the scenario as in CO_2 CARS studies where its Fermi-resonance can cause heterodyne beating. Thus, we can also use a relatively long probe delay for H_2 CARS in order to suppress the nonresonant interferences.

8.2 Hencken Burner Flame Measurement.

Preliminary H_2 CPP fs CARS studies have been performed for H_2-Air flame over the Hencken burner with varying equivalence ratios from 1.0 to 2.0. Unfortunately, due to the low heat capacity of H_2, the adiabatic flame temperature only ranges from 2092 K to 2380 K. The experimental measurements and the corresponding spectral fitting results are shown below

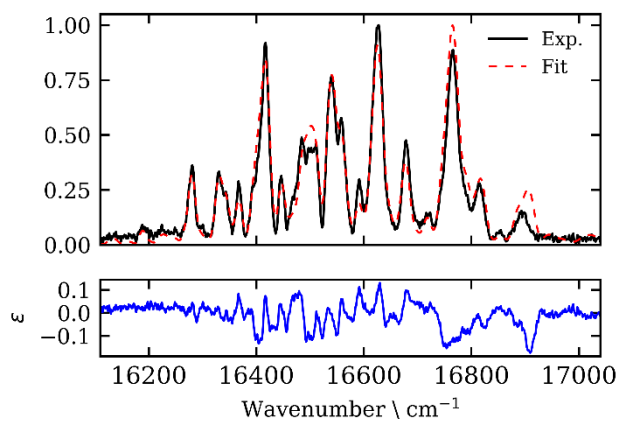

Figure 8.2 Experimentally measured H_2 CPP fs CARS spectrum as compared to its theoretical calculation from the spectral fitting code. The adiabatic flame temperature is 2379 K, the probe time delay is about 9 ps.

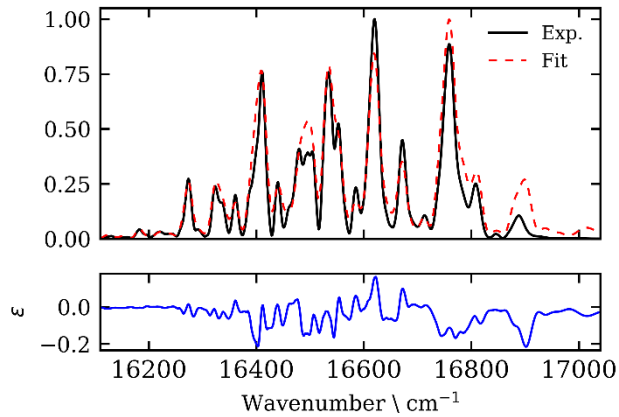

Figure 8.3 Experimentally measured H_2 CPP fs CARS spectrum as compared to its theoretical calculation from the spectral fitting code. The adiabatic flame temperature is 2092 K, the probe time delay is about 9 ps.

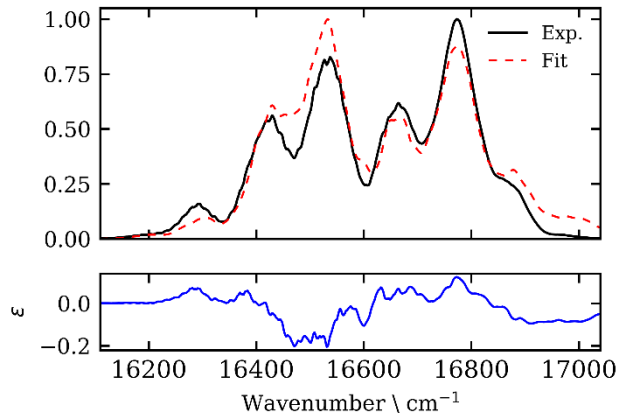

Figure 8.4 Experimentally measured H_2 CPP fs CARS spectrum as compared to its theoretical calculation from the spectral fitting code. The adiabatic flame temperature is 295 K, the probe time delay is about 9 ps.

The probe timed delay was set up 9 ps, thus the measured CPP fs CARS signals are only due to the resonant responses of H_2. The agreement between the experiment and the theoretical calculation is overall satisfactory. The measurement at 2379 K adiabatic flame temperature matches best with the spectral fitting result. While the room temperature case the agreement is relatively poor. While it is possible that the mismatch between the theory and experiment originates from the modelling aspects. Another possibility is that the ultrafast pulse in H_2 might also exhibit certain extent of SPM which is most significant at higher gas number densities (low temperature).

Meanwhile, the difference of the H_2 CPP fs CARS spectrum remains small between the 2092 K and 2379 K adiabatic flame temperature cases. To validate the accuracy and precision of H_2 CPP fs CARS for thermometry measurement, the extension of temperature measurement range is desired.

8.3 Conclusion

Some preliminary H_2 CPP fs CARS measurements have been performed over Hencken burner for the fuel-rich condition. The spectral fitting code that incorporates the Herman-Wallis correction factor and the H_2 linewidth model was developed. The agreement between the experimental measurement and the theoretical calculation is satisfactory especially for the high temperature case. The current experiment is limited by the temperature range achievable through the H_2-Air Hencken burner setup. The extension to lower temperature range measurement can be made available by using the high-pressure high temperature cell, and the higher temperature measurement can be made possible by using synthetic air or even pure O_2 as the oxidizer. The development of H2 CPP fs CARS technique might provide options for our future rocket combustion diagnostic studies especially in the high temperature regime.

CHAPTER 9. HIGH-PRESSURE HIGH TEMPERATURE (HPHT) GAS CELL MEASUREMENT

CPP fs CARS spectrum of CO_2, and O_2 have been performed in a high-pressure high-temperature (HPHT) gas cell. The measurements are performed at temperatures below 1000 K and for pressure range from 1 to 25 bar. In this chapter, both the experimental measurement results and the spectral modelling aspects of high-pressure CARS spectra are presented.

9.1 CO_2 Linewidth Modelling at High Pressure

In frequency domain, the spectral lines for CO_2 Q-branch transitions within a vibrational manifold are tightly spaced. The average frequency spacing is in the order of 0.025 cm^{-1} whereas it is about 0.25 cm^{-1} for N_2. The collisional line-mixing is still important for CO_2 because the collisional energy transfer rate is almost twice that of N_2. Besides, unlike many simple diatomic molecules like N_2 and O_2 where the vibrational dephasing rate can be neglected in a moderate pressure range, the inclusion of vibrational line broadening and line shifting is important for CO_2 especially at high pressures. To better incorporate the collisional line-mixing effects and the vibrational dephasing effect, we can use *G*-matrix method as it is mentioned in Chapter 3.

$$\mathbf{G} = -\omega\mathbf{I} + \mathbf{\Omega}_{J0} + \sigma_v\mathbf{I} + i\Gamma_J - i\gamma_v\mathbf{I} \tag{7.4}$$

$\mathbf{\Omega}_{J0}$ and Γ_J are the rotational frequency matrix and the rotational relaxation matrix as mentioned in Chapter 3. While σ_v and γ_v denote the vibrational linewidth and vibrational frequency shift respectively and they are number density dependent.

First, we investigate the effects of collisional line mixing on frequency resolved CO_2 CARS profile, the simulation results are shown in Figure 9.1 and Figure 9.2. At 0.05 atm, the differences remain small between the two simulation results. At 0.5 atm, the linewidth of the entire Q-branch transition is obviously by including the collisional line mixing effects than using the individual line approximation. From the relative strength of each Q-branch transition it can also be found that the rotational collisions have enabled the transitions in favor of lower wavenumbers.

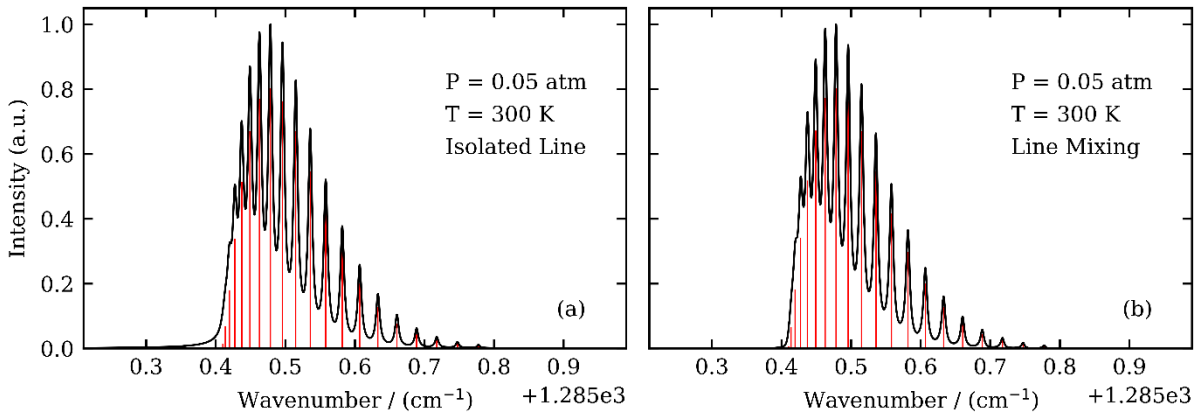

Figure 9.1 Simulation of the $2\nu_2$ Q-branch of CO_2 vibrational transition at 0.05 atm with (b) and without (a) the inclusion of collisional line mixing effects. The red lines denote the relative strength of each individual Q-branch transition. (Only the Lorenzian contribution is labeled, the dispersive contribution is not labeled but is included in the calculation.)

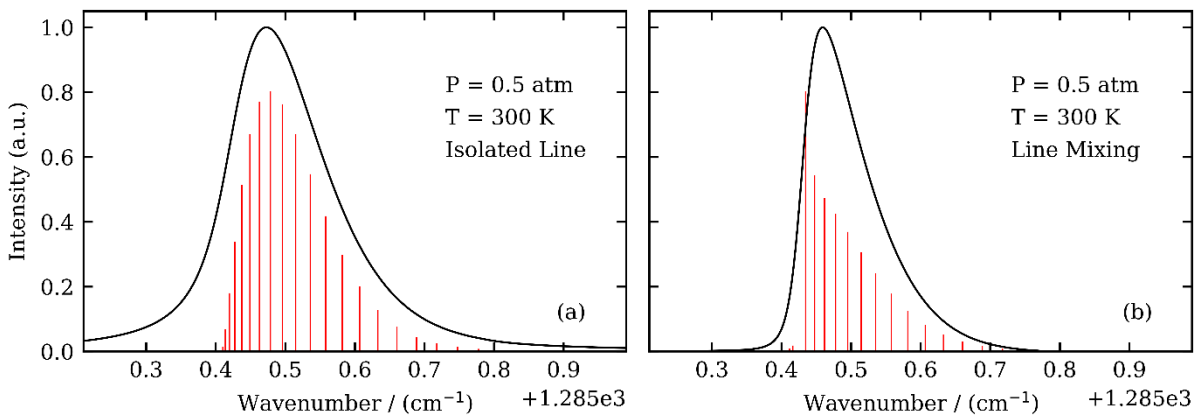

Figure 9.2 Simulation of the $2\nu_2$ Q-branch of CO_2 vibrational transition at 0.5 atm with (b) and without (a) the inclusion of collisional line mixing effects. The red lines denote the relative strength of each individual Q-branch transition. (Only the Lorenzian contribution is labeled, the dispersive contribution is not labeled but is included in the calculation.)

Same calculations are performed for higher pressures, as shown in Figure 9.3 and Figure 9.4 we compare the results with and without the inclusion of vibrational dephasing. In this study, for $2\nu_2$ transition, the vibrational dephasing coefficients are given as $\sigma_v = -12.2\times10^{-3}$ cm^{-1}amagat^{-1}, $\gamma_v = 5.3\times10^{-3}$ cm^{-1}amagat^{-1}[97]. The vibrational linewidth is already comparable to the linewidth

caused by rotational collisions at 5 atm. Meanwhile, it is evident that the rotational collisions will cause only few transitions dominant at higher pressures.

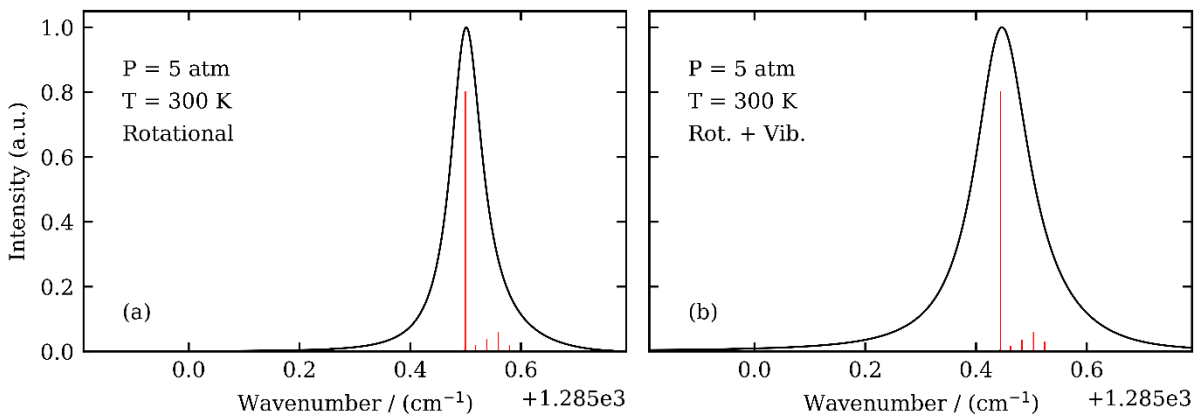

Figure 9.3 Simulation of the $2\nu_2$ Q-branch of CO_2 vibrational transition at 5 atm with (b) and without (a) the inclusion of vibrational broadening and line shifting.

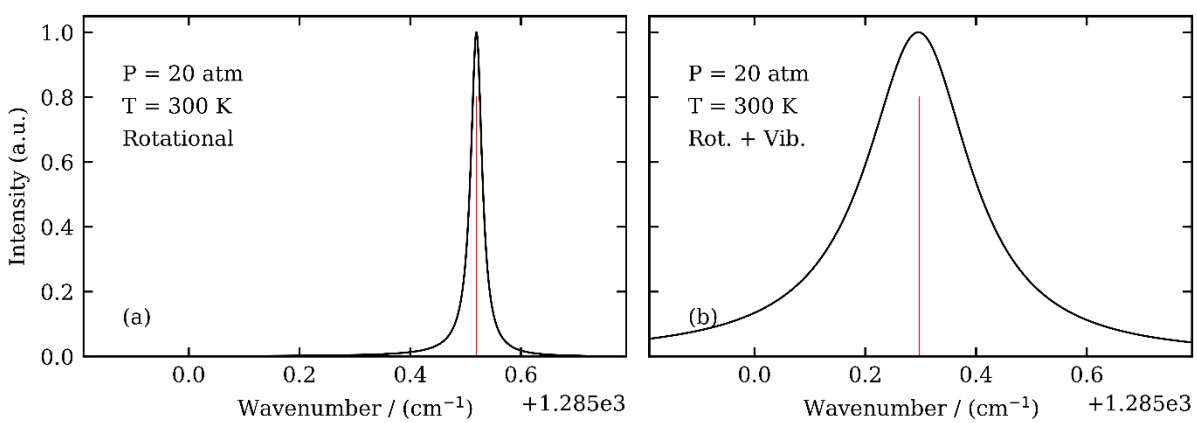

Figure 9.4 Simulation of the $2\nu_2$ Q-branch of CO_2 vibrational transition at 20 atm with (b) and without (a) the inclusion of vibrational broadening and line shifting.

Similar studies can be performed for ν_1 band of CO_2 Q-branch transitions. For ν_1 band of vibrational transition, the Q-branch rotational lines are even more tightly spaced (the average frequency spacing is about 0.0005 cm^{-1}). For gas number density above 1 amagat, the linewidth of the ν_1 band is determined by vibrational dephasing. The vibrational dephasing coefficients are given as $\sigma_v = -8.1\times10^{-3}$ $cm^{-1}amagat^{-1}$, $\gamma_v = 3.1\times10^{-3}$ $cm^{-1}amagat^{-1}$[149].As shown in Figure 9.5,

at 20 atm, the simulated Q-branch linewidth for ν_1 band is also narrower than $2\nu_2$ band because the smaller vibrational broadening coefficient.

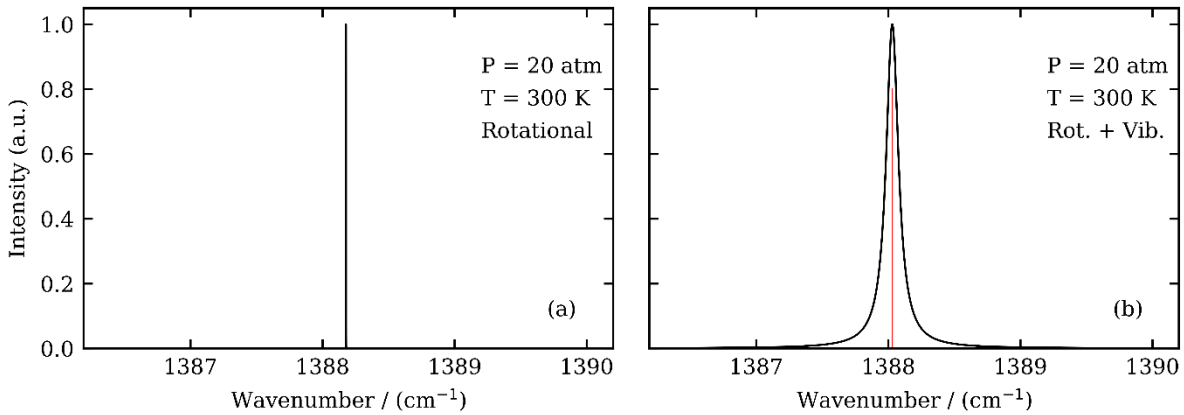

Figure 9.5 Simulation of the ν_1 Q-branch of CO_2 vibrational transition at 20 atm with (b) and without (a) the inclusion of vibrational broadening and line shifting.

For CO_2 CPP fs CARS, the effects of collisional narrowing and vibrational dephasing are less significant because the laser-matter interaction timescale is relatively short. However, when long probe delay is used, as is the case for our experiment, the inclusion of the accurate linewidth model is necessary especially for high pressure conditions. The behavior of collisional narrowing of O_2 CARS is very similar to N_2 and is thus omitted here. The MEG law is used to model the collisional transfer rate and the coefficients are obtained from literature[150, 151].

9.2 Measurements in the HPHTC

9.2.1 CO_2 at Room Temperature and Elevated Pressures

Our previous studies have shown that CO_2 can cause more significant ultrashort pulse self-phase modulation than gaseous species like N_2, O_2 and CH_4. The most straightforward approach to mitigate SPM is by reducing the laser intensity; however, the tradeoff is the reduction of CARS signal intensity. To determine the optimal laser intensity for the high-pressure experiment, similar laser power spectrum measurements are performed for high pressure CO_2 gas medium.

With 40 μJ of laser energy for both pump and Stokes pulses, we start observing SPM becoming obvious above 15 amagat gas number density. While the laser spectrum is recorded right after the HPHT cell, the real SPM at the probe volume could be exaggerated. For a sanity check, we record CO_2 CPP fs CARS spectrum with this power setting, and they are shown in Figure 9.6 and Figure 9.7.

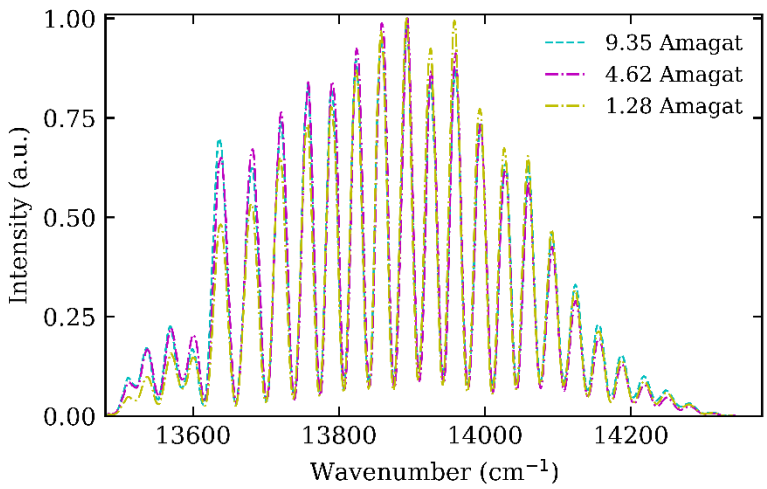

Figure 9.6 CO_2 CPP fs CARS spectrum recorded from 1.28 amagat to 9.35 amagat (room temperature). The pump and the Stokes energies are both 40 μJ.

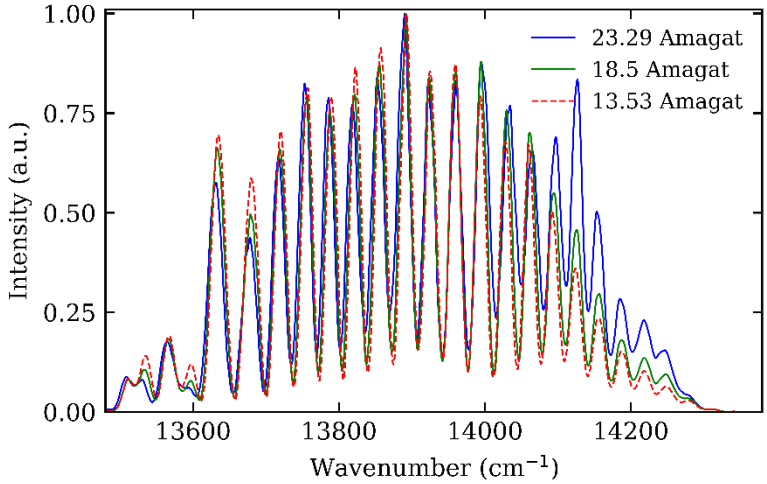

Figure 9.7 CO_2 CPP fs CARS spectrum recorded from 13.53 amagat to 23.29 amagat (room temperature). The pump and the Stokes energies are both 40 μJ.

As shown in Figure 9.6, with moderately high gas number density range, the spectral modulation of the CPP fs CARS spectrum is not as significant as it was shown in Figure 9.7. We find that the change of CARS spectrum is especially evident from 18.5 amagat to 23.29 amagat. From the CCD camera, the image mode data of the CO_2 CPP fs CARS spectrum is shown in Figure 9.8. For gas number densities above 13.53 amagat, the image mode CPP fs CARS signal start to get distorted and shift towards top pixels. For 23.29 amagat, a separate signal image is found generated below the main signal image. This indicates the spatial profile of the laser beam or the spatial overlapping among the pump, Stokes and probe beams has changed for high gas number density case. One possible explanation is due to the self-focusing of the ultrashort pulse in the high-pressure gas medium. And the approach to reduce self-focusing is very similar to the way of mitigating SPM, i.e., by reducing the laser intensity further.

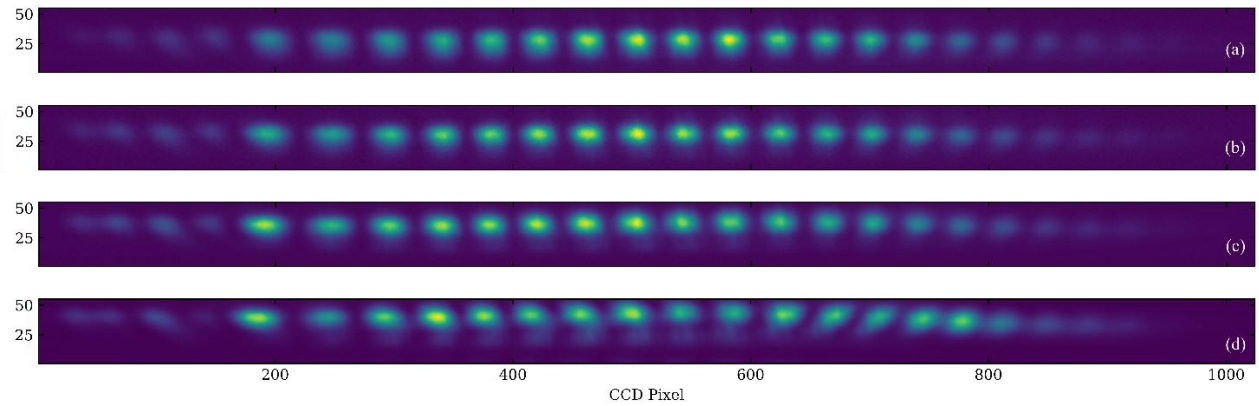

Figure 9.8 CCD image of the CO_2 CPP fs CARS signal at (a) 1.28 amagat, (b) 9.35 amagat, (c) 13.53 amagat and (d) 23.29 amagat. The horizontal CCD pixel number denotes wavelength axis. For our experimental CPP fs CARS spectrum acquisition, a full binding of the vertical pixels is performed. The pump and the Stokes energies are both 40 μJ.

In Figure 9.9 and Figure 9.10 we show the CPP fs CARS spectrum for 20 μJ pump and Stokes pulse energies. The spectral modulation as a factor of gas number density become less significant as compared to previous 40 μJ pump and Stokes energies. For 23.29 amagat, however, the distortion of the CPP fs CARS spectrum is still obvious.

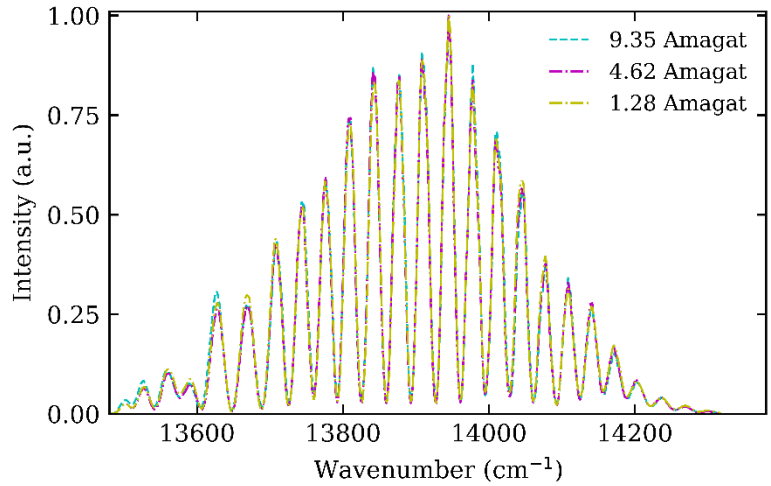

Figure 9.9 CO_2 CPP fs CARS spectrum recorded from 1.28 amagat to 9.35 amagat (room temperature). The pump and the Stokes energies are both 20 μJ.

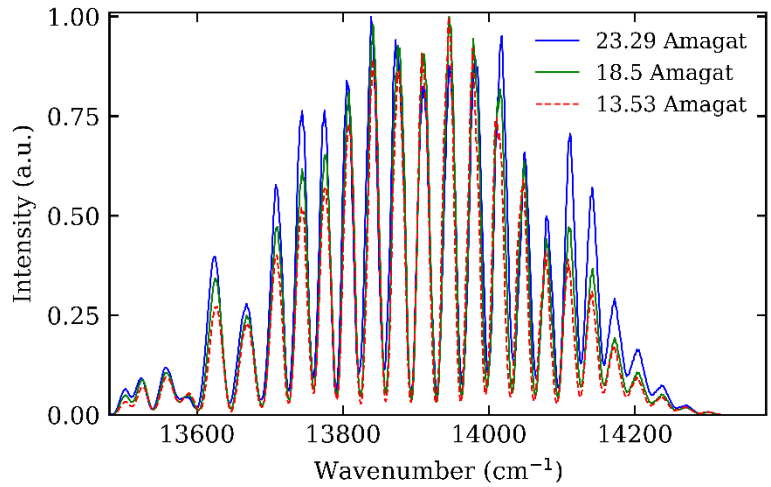

Figure 9.10 CO_2 CPP fs CARS spectrum recorded from 13.53 amagat to 23.29 amagat (room temperature). The pump and the Stokes energies are both 20 μJ.

Similarly, the CCD image of the CARS signal with this reduced laser energy settings is as shown in Figure 9.11. The elevation and distortion of the CPP fs CARS image is less obvious as compared to Figure 9.8. Though further reduction of the laser intensity is possible, this could reduce the signal intensity at lower gas number density. On the other hand, since the measurements shown above are all performed at room temperature, for higher temperatures, with gas number densities

below 20 amagat, the pressure range being investigated could be much higher than 20 bar. Alternatively, we could dynamically adjust the laser power during experiment. I.e., for low gas number densities where SPM and self-focusing is less significant, a higher laser power can be used to increase the CARS intensity, for high gas number density where CARS signal strength is sufficiently strong, a low laser power can be used.

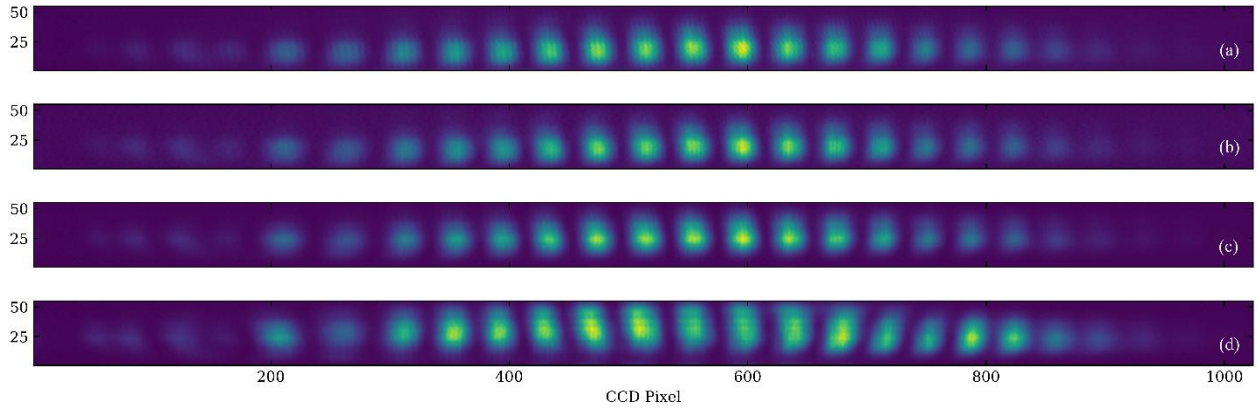

Figure 9.11 CCD image of the CO_2 CPP fs CARS signal at (a) 1.28 amagat, (b) 9.35 amagat, (c) 13.53 amagat and (d) 23.29 amagat. The horizontal CCD pixel number denotes wavelength axis. For our experimental CPP fs CARS spectrum acquisition, a full binding of the vertical pixels was performed. The pump and the Stokes energies were both 20 μJ.

When the spatial overlap of the pump, Stokes and probe beams are unchanged during pressure variation, the CARS signal intensity scales quadratically with the gas number density (without saturating the transitions). As shown in Figure 9.12, for 40 μJ pump and Stokes energy case, the quadratic correlation between the CARS intensity and the gas number density is no longer true, the signal intensity even started to decrease from 18.5 amagat to 23.3 amagat. The depletion of the Raman transitions is less likely the cause because it could appear more obvious at lower gas number densities if it were. On the other hand, the quadratic relationship is found quite good for 20 μJ pump and Stokes energy case, which implies the laser energies suitable for the experimental measurements.

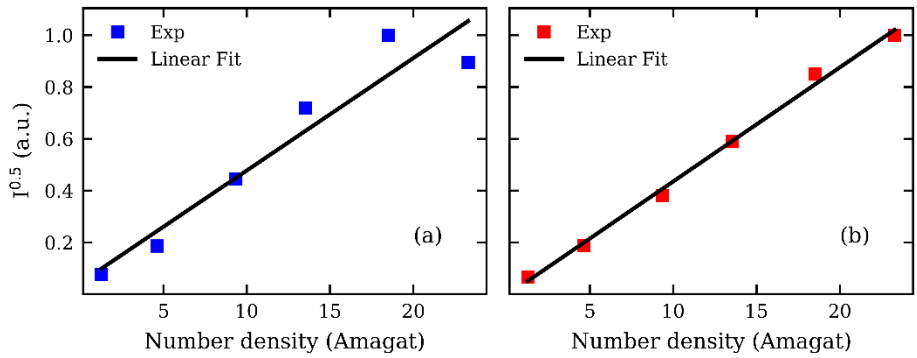

Figure 9.12 Normalized square root of the CO_2 CPP fs CARS signal intensity as versus to the gas number density for (a) 40 μJ pump and Stokes laser energies and (b) 20 μJ pump and Stokes laser energies.

9.2.2 CO_2-O_2 Mixtures at Room Temperature and Elevated Pressures

The CO_2-O_2 CPP fs CARS spectrum has been measured for 40% of CO_2 and 60% of O_2 in the high-pressure gas cell and the results are shown in Figure 9.13. Surprisingly, even with the same mixture concentration, the CPP fs CARS spectrum seems to be dependent upon the total gas number density. The probe delay of the experimental measurements is about 6 ps, according to our previous discussions on the dephasing rate difference between CO_2 and O_2 in Chapter 7, the CO_2 CARS signal will dominate as O_2 CARS signal decays much faster. However, this difference of the frequency spread dephasing rate between CO_2 and O_2 cannot explain why at low gas number densities the relative strength of O_2 CPP fs CARS signal becomes stronger since the probe delay is kept identical during the experimental measurements. Neither can this relative CARS intensity variation be explained within the framework of SPM or self-focusing as we have tuned the laser energy to suppress it. And without saturating the Raman transitions, both the O_2 and CO_2 CPP fs CARS strength should scale quadratically with gas number densities. One possible explanation is that the collisional narrowing for CO_2 is much more significant than O_2. At high pressures, the overall bandwidth of CO_2 rovibrational transitions is narrower than O_2 at high gas number densities than at low gas number densities. The difference of frequency spread dephasing rate between CO_2 and O_2 is thus even more significant at high gas number densities than at low gas number densities.

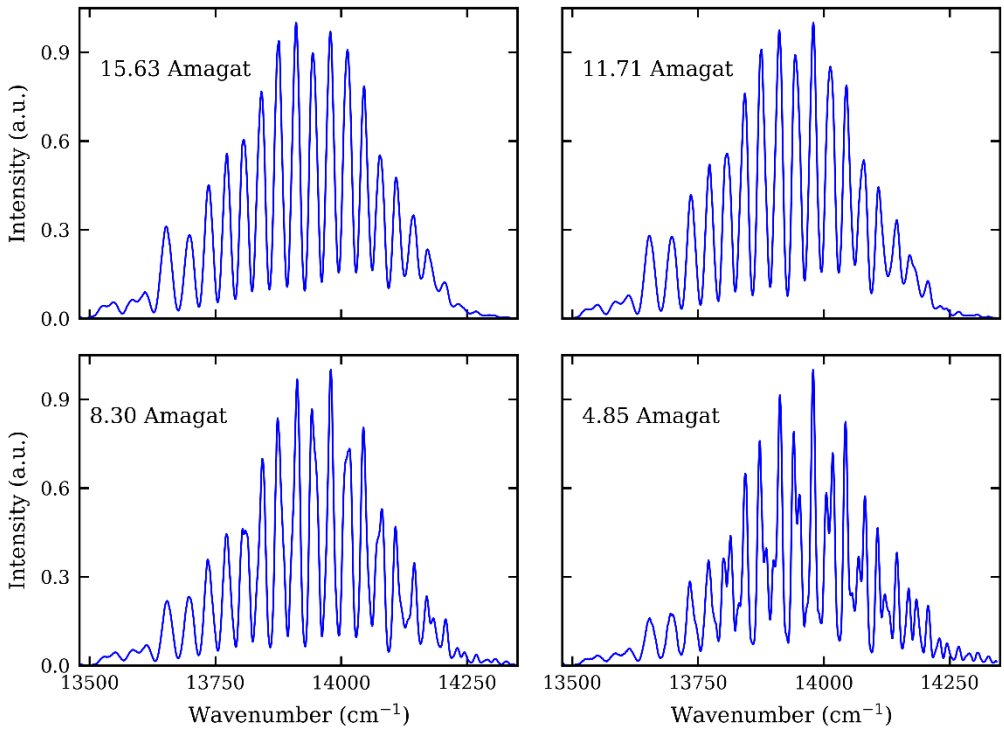

Figure 9.13 CO_2-O_2 CPP fs CARS spectrum with 60% of O_2 and 40% of CO_2. The measurements are performed at room temperature and the probe time delay is about 6 ps.

9.2.3 CO_2 at High Pressure and High Temperatures

CO_2 CPP fs CARS measurements at elevated temperatures are performed in the high-pressure gas cell, the preliminary measurements below 500 K are shown in Figure 9.14. The measurements are performed by first pressurizing the gas cell at room temperature, the inlet and outlet ports are then closed while the external heating starts, thus the gas number density can be kept constant throughout the heating process. The temperature dependent variation is obvious despite the fact that vibrational CARS are not typically used for low temperature thermometry measurement (below 1200 K). On the other hand, the obstacles that hinder higher temperature measurements right now are the strong background caused by the pump beam scattering. As shown in Figure 9.15, the pump beam scattering seems to become more significant at higher temperatures. The cause of this background scattering is still unclear, one possibility is the excess heating causes the physical property of the glass windows to change so that the pump beam diffraction on the windows material becomes more severe at higher temperatures. To get around the background from the pump beam scattering, one approach is to increase the optical pathlength for the CARS signal collection after

the collimating lens. This is because the CARS signal is laser like while the scattering light is spatially incoherent and will diminish eventually. Alternatively, one can switch to a laser configuration where the CARS signal wavelength is different from the pump.

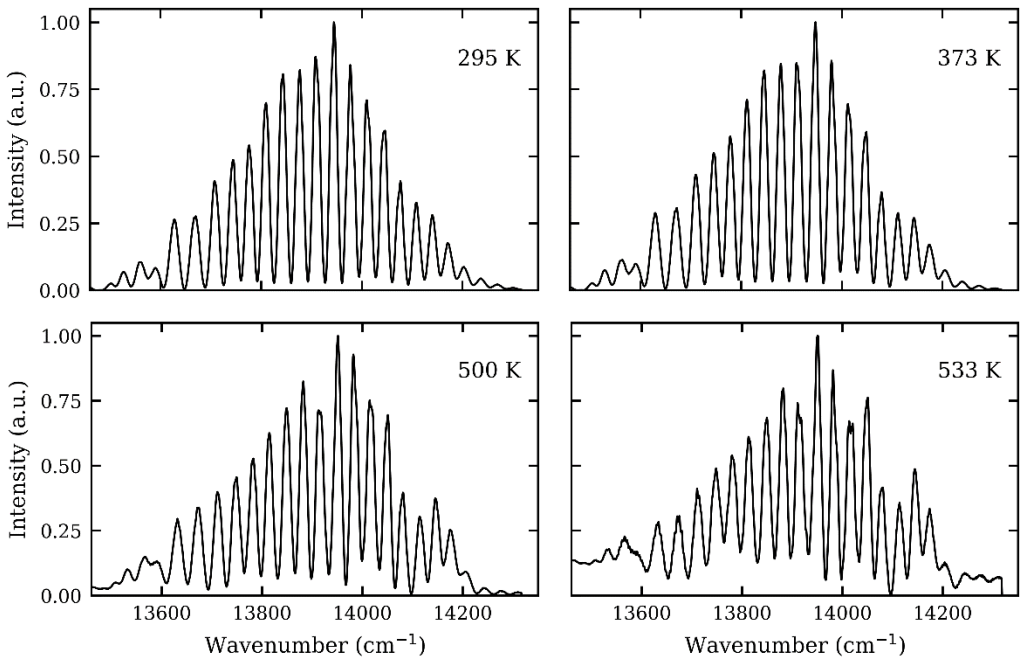

Figure 9.14 CO_2 CPP fs CARS measurements in the high pressure gas cell with different temperatures. The gas number density is kept constant as 2.0 amagat. The probe delay is about 7 ps for all the cases.

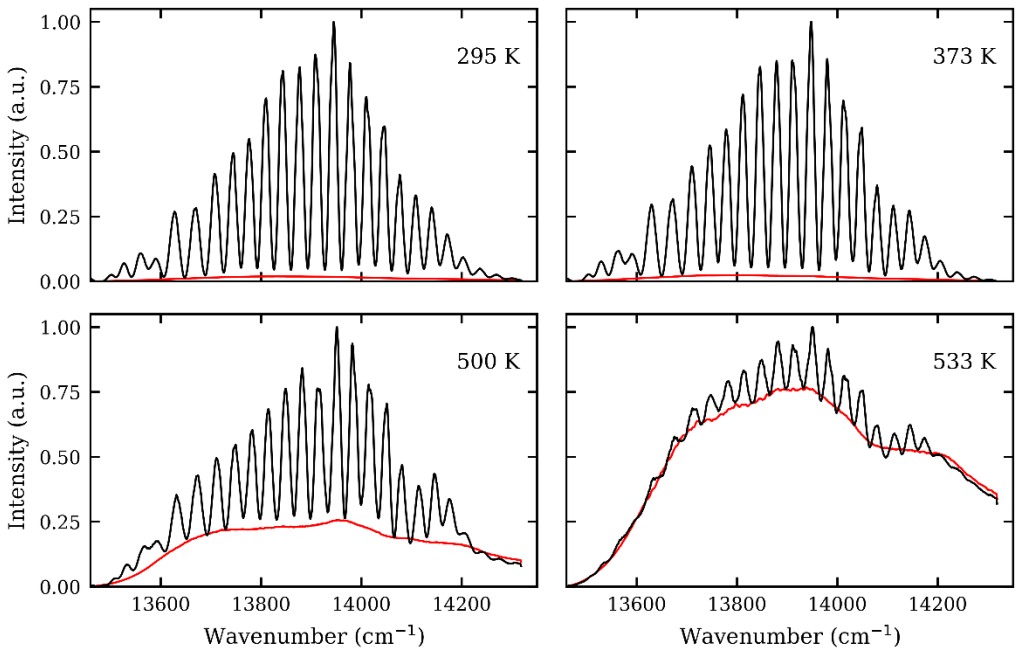

Figure 9.15 CO_2 CPP fs CARS (without background subtraction) measurements in the high pressure gas cell with different temperatures. The background is also shown for comparison (red lines), both the CARS spectrum and the background are normalized to the maximum signal intensity. The gas number density is kept constant as 2.0 amagat. The probe delay is about 7 ps for all the cases.

9.3 Spectral Fitting Results

To fit the experimentally measured CO_2 CPP fs CARS spectrum for high gas number densities, the inclusion of collisional line mixing and vibrational dephasing is critical. A simulation of the CO_2 CPP fs CARS spectrum with and without the line mixing model and the vibrational dephasing are shown below.

As shown in Figure 9.16 and Figure 9.17, when the collisional line mixing effects and vibrational dephasing are considered, the differences of the simulated CO_2 CPP fs CARS spectrum between low and high gas number densities cases are relatively small. This also agrees with our experimental observations.

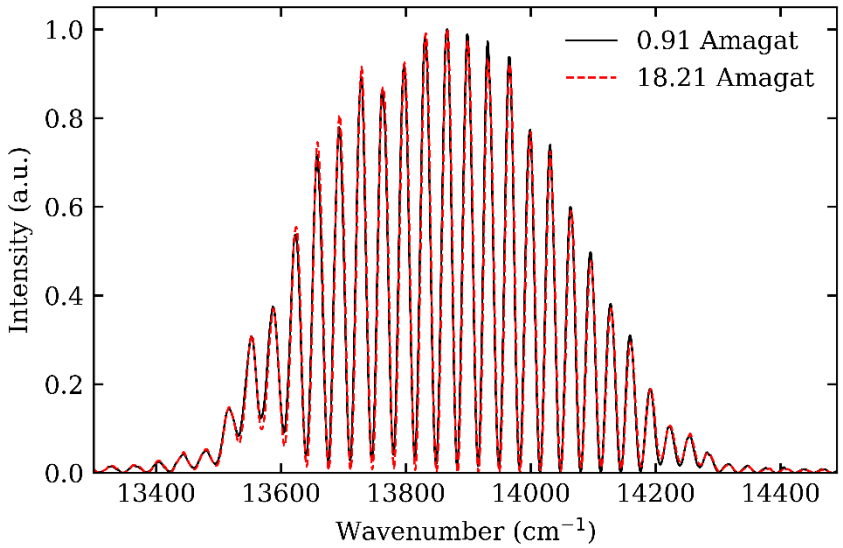

Figure 9.16 Simulated CO_2 CPP fs CARS spectrum at room temperature and for low (0.91 amagat) and high (18.21 amagat) gas number densities. The PTD is 6 ps, the collisional line mixing model and vibrational dephasing is considered in the simulation.

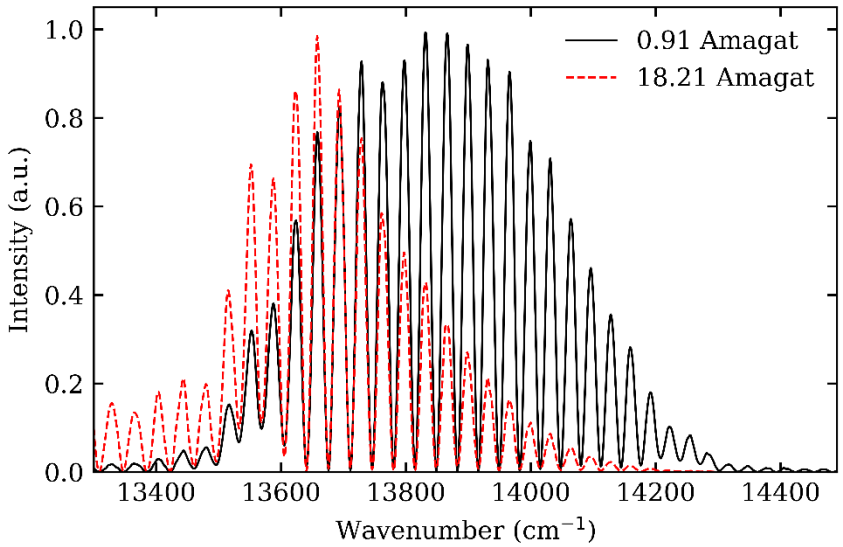

Figure 9.17 Simulated CO_2 CPP fs CARS spectrum at room temperature and for low (0.91 amagat) and high (18.21 amagat) gas number densities. The PTD is 6 ps, separate line approximation is made, and vibrational dephasing is not included.

For room temperature measurement, we decided the highest gas number density that is free of SPM is about 18.6 amagat, the comparison between the experimental measurement spectrum and the theoretical calculation that enables collisional line mixing is as shown in Figure 9.18.

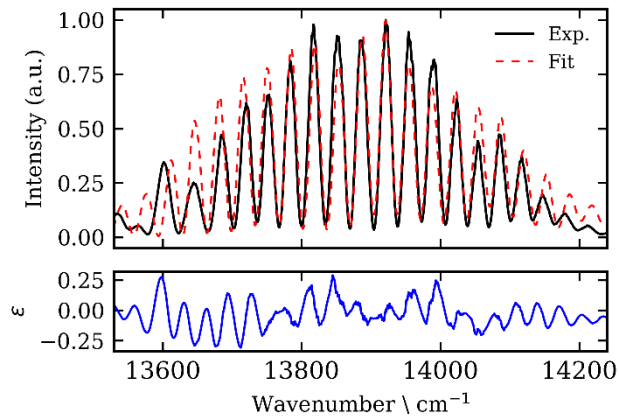

Figure 9.18 Comparison between the measured CO_2 CPP fs CARS spectrum at 18.6 amagat (room temperature) and the theoretical calculation that enables collisional line mixing.

The agreement between the experiment and theoretical calculation is less satisfactory at both high and low frequencies. Similar disagreement has also been found in our previous atmospheric pressure measurements. Thus, we believe this slight mismatch is less an issue of collisional effects. One possibility is the frequency to pixel mapping is not perfect, as shown in Figure 9.19, three atomic lines are all above 13800 cm^{-1}, the frequency to pixel mapping is assumed to be linear in between the atomic lines, while extrapolation is used for pixels beyond the range of atomic line positions. This extrapolation and even the linear interpolation itself will introduce some uncertainty. Another possible cause of this disagreement could be because the measurement laser power spectrum is not accurate enough. Though, we reduced the laser energy enough to avoid SPM inside the high-pressure gas medium, the windows material can still cause certain degree of SPM.

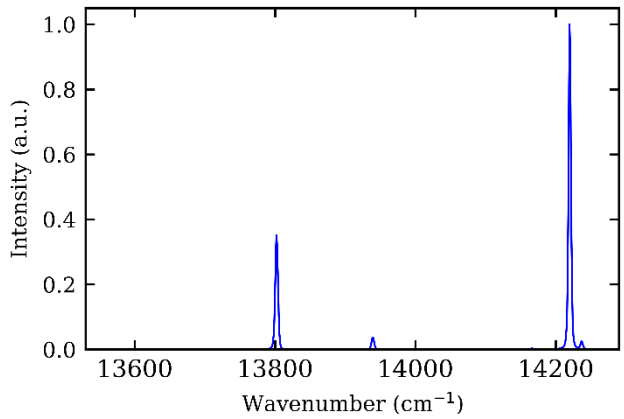

Figure 9.19 Neon lamp calibration spectrum for the CO_2 CPP fs CARS measurement.

9.4 Conclusions

CPP fs CARS measurements have been performed for CO_2 and CO_2-O_2 in the HPHTC. Laser intensity is controlled to suppress the SPM and laser pulse self-focusing by checking the measured laser power spectrum as well as the image mode CARS signal on the CCD camera. We find that the while nonlinear optical effects like SPM are suppressed, the CPP fs CARS spectrum in pure CO_2 is relatively stable from 1 to 20 amagat gas number density at 298 K. Our frequency domain analysis as well as the spectral fitting results indicate that the inclusion of collisional narrowing is critical in accurately modelling the high-pressure CO_2 CPP fs CARS data. For the high-pressure CO_2-O_2 CPP fs CARS measurements, we find that the relative intensity between CO_2 and O_2-CARS signal is gas number density dependent, and this might still can be explained within the framework of the strong collisional narrowing in CO_2. Finally, our preliminary CO_2 vibrational CARS measurements in the heated gas cell indicate the potential for its thermometry extraction even below 500 K. To suppress the pump beam scattering background and to enable even higher temperature measurements in the future, a degenerate pump probe setup can be used in the future so that the CARS frequency can be separated out from the three laser beams.

CHAPTER 10. CONCLUSIONS AND FUTURE WORK

10.1 Summary and Impact.

The work presented in this dissertation has focused on developing CPP fs CARS measurements for high pressure systems especially associated with high pressure rocket combustion applications. The major contributions of this thesis research include:

1. Characterization of frequency chirp on the ultrafast pulse, and the inclusion of frequency chirp and the resultant Raman excitation efficiency profile in the spectral fitting code.
2. Investigation and suppression of self-phase modulation effects associated with ultrafast laser propagation in the high-pressure gas medium.
3. Development and parallelization of the time-dependent densitymatrix code for theoretical analysis. The parallelization of the spectral fitting code.
4. Modelling of CO_2 CPP fs CARS, the development CO_2 CPP fs CARS technique for thermometry measurement and for relative CO_2-O_2 concentration extraction.
5. First-time high-pressure CO_2-O_2 fs CARS measurement, the incorporation of collisional narrowing model especially for CO_2 at high pressure.

The effects of moderate frequency chirp for the pump and Stokes pulses on CPP fs CARS temperature measurements were investigated both theoretically, by computing the CPP fs CARS spectra by solution of the time-dependent density matrix equations, and experimentally by inserting disks of SF11 glass in the beam paths of the CARS input beams. A major conclusion of the study is that transmission of the beams through thick glass windows will not significantly affect temperature measurement accuracy and precision. One major effect of moderate pump/Stokes chirp is that the spectrum of the nonresonant background narrows significantly, and the influence of the nonresonant background spectrum can be minimized in the temperature sensitive region of the spectrum. The envelope of Raman excitation efficiency also narrows due to moderate pump/Stokes chirp, and this effect must be incorporated in phenomenological models used to fit CPP fs CARS spectra.

The effects of SPM on CPP fs CARS measurements were evaluated at high pressures and with varying laser energies. We found that with sufficiently high laser energy, SPM can become significant and result in modulation of CPP fs CARS spectra even at moderate pressures. SPM effects were also evaluated for several different gaseous species including CO_2, O_2 and CH_4, it was found that N_2 exhibits least amount of SPM while CO_2 has strongest SPM among those molecules being studied. The modulated laser spectrum due to SPM in high pressure N_2 gas was successfully modeled, and the extracted nonlinear refractive index agreed with the literature reported values. However, one of the major conclusion of this study is that it is preferable to eliminate SPM effects by reducing the laser intensity rather than to try to incorporate it into the CARS modelling since its influence can be much more complex and even intractable especially when several gaseous species are to be involved. This study provides the guidelines for picking up the optimum laser intensities for high pressure fs CARS measurements.

CO_2 CPP fs CARS technique was developed for thermometry measurement. A phenomenological model of CO_2 CPP fs CARS was developed and was verified in various CO_2/O_2 mixtures as well as at different flame temperatures. Because the rotational transitions within a vibrational manifold of CO_2 are tightly spaced, and because the CO_2 molecule has a special Fermi-resonance structure, the time domain resonance signal of CO_2 is oscillatory and has a long dephasing time scale than O_2. Though the vibrational transition frequency of O_2 is very close to CO_2, we showed that at large probe delays one can suppress the O_2 resonant interference and the nonresonant signal interferences in the CO_2 spectrum. Therefore, the CO_2 CPP fs CARS spectrum obtained at long probe delays is dominated by the resonant contribution of CO_2. Comparison between flame thermometry obtained from CO_2 and N_2 CPP fs CARS measurements shows that CO_2 is well-suited for temperature measurements below 1200 K. Another advantage of CO_2 CPP fs CARS at long probe delays is that it enables accurate thermometry with only a single set of laser parameters.

CPP fs CARS measurements were performed for CO_2 and CO_2-O_2 in the HPHTC. We found that while nonlinear optical effects like SPM were suppressed, the CPP fs CARS spectrum in pure CO_2 was relatively unchanged from 1 to 20 amagat gas number density at 298 K. Our frequency domain analysis as well as the spectral fitting results indicated that the inclusion of collisional narrowing is critical in accurately modelling the high-pressure CO_2 CPP fs CARS data. For the high-pressure CO_2-O_2 CPP fs CARS measurements, we found that the relative intensity between

CO_2 and O_2 CARS signal is gas number density dependent, and this might still can be explained within the framework of the strong collisional narrowing in CO_2. Finally, our preliminary CO_2 vibrational CARS measurements in the heated gas cell indicate the potential for its thermometry extraction even below 500 K.

In addition to the development of CPP fs CARS technique as summarized above, a time resolved densitymatrix equation (Liouville's equation) code was developed and parallelized. The parallelized code also enables the easy incorporation of collisional narrowing effects through thread communication of population and coherence information. This densitymatrix code has been used in this study to calculate the Raman excitation efficiency change due to moderate amount of pump and Stokes chirp, and it has also been used to verify the collisional line-mixing calculation from *G*-matrix approach. The spectral fitting code has also been parallelized for higher numerical efficiency.

10.2 Suggested Directions of Future Work

The experimental study of CPP fs CARS measurements in the HPHTC has so far been applied for CO_2 and O_2 for pressure range from 1-25 atm and for temperature range from 295-500 K. The extension of pressure and temperature range will be of practical interests as the cell was designed for pressure range from 1-100 atm and temperature range from 295-1000 K. Together with our previous CO_2 CARS studies over the Hencken burner, one of the objective of the CO_2 CARS study is to establish its accurate thermometry measurement from 295 K to about 1700K and for gas number density of up to 20 amagat. This will provide more useful information for the diagnostic studies for rocket combustion relevant applications. Right now, one of the major obstacles for higher temperature measurement inside the HPHTC is the strong background caused by the pump beam scattering. Though the mechanism of this temperature-dependent pump scattering is yet not clear. One way to get around with it is to use a degenerate pump probe laser setup so that the CARS signal frequency can be separated from the pump frequency. In addition, investigations need to be made for CO_2-O_2 mixture measurements especially for the HPHTC as our preliminary studies indicate that the relative strength of CO_2 and O_2 CARS signal can be pressure dependent. Possible solutions might include using even longer probe delays to fully suppress O_2 interference from CO_2 measurement, or we can incorporate this pressure dependence of the relative CARS signal strength into the theoretical model so that pressure information can be extracted. Meanwhile, the targe species for CARS measurements can be extended to H_2, CH_4 and even H_2O. For H_2 CARS, the

theoretical model for phenomenological modelling has already been developed, some experimental measurements have also been performed in an atmospheric-pressure laminar flame established over a Hencken burner. The main objective of the H_2 CPP fs CARS studies will be focused on its application in high temperature thermometry measurement because its vibrational frequency is much higher than CO_2 and O_2. H_2O CARS might need to be considered together with H_2 CARS studies as their vibrational frequencies are also close and H_2O is naturally abundant in H_2-O_2 flames. Similarly, CH_4 CPP fs CARS studies can be of practical interests for CH_4-O_2 combustion studies as it provides an alternative solution to CO_2 CPP fs CARS. The monitoring and suppression of SPM in different gaseous species and different test conditions should also be made alongside with those measurements.

In the meantime, while those fundamental CPP fs CARS studies in the HPHTC or other canonical combustion systems are performed. Investigations of those CARS technique inside the rocket combustion chamber can be performed simultaneously. The envisioned challenges associated with the experimental studies include the strong background caused by the flame luminescence, beam steering caused by the turbulent flow or oscillatory chamber cavity, and complex composition of gaseous species in the probe volume etc. One possible way to get rid of the strong background noise is to polarization suppression since the CARS signal is highly polarized. Alternatively, one can control the pockel cell frequency to 2.5 kHz while the CCD camera is still kept at 5 kHz so that each single shot of CARS acquisition can be followed by an acquisition of background noise. The possible strong beam steering can be overcome by using other phase matching schemes, for example, by using co-annular CARS geometry the spatial overlap among three laser beams will be less susceptible to beam steering. The complex composition in the probe volume is associated more with the choice of choosing the proper target species. Overall, several combinations of gaseous species can be made for CARS measurement, e.g., CO_2-O_2 CARS, H_2-H_2O CARS and CH_4 CARS etc.

In brief, the future work can focus on developing and refining the current CO_2-O_2 CPP fs CARS technique in the HPHTC measurement. And the measurement species can be extended to other relevant species such as H_2, CH_4, and H_2O. The investigations and applications of those CARS techniques to the high-pressure rocket combustion can be the final goal of this research studies.

REFERENCES

1. P. D. Maker, and R. W. Terhune, "Study of Optical Effects Due to an Induced Polarization Third Order in the Electric Field Strength," Physical Review **137**, A801-A818 (1965).

2. A. C. Eckbreth, "BOXCARS: Crossed-beam phase-matched CARS generation in gases," Appl Phys Lett **32**, 421-423 (1978).

3. A. C. Eckbreth, and R. J. Hall, "CARS thermometry in a sooting flame," Combustion and Flame **36**, 87-98 (1979).

4. R. J. Hall, J. F. Verdieck, and A. C. Eckbreth, "Pressure-Induced Narrowing of the Cars Spectrum of N-2," Opt Commun **35**, 69-75 (1980).

5. D. A. Greenhalgh, F. M. Porter, and W. A. England, "The application of coherent anti-Stokes Raman scattering to turbulent combustion thermometry," Combustion and Flame **49**, 171-181 (1983).

6. R. P. Lucht, R. E. Teets, R. M. Green, R. E. Palmer, and C. R. Ferguson, "Unburned gas temperatures in an internal combustion engine. I: CARS temperature measurements," Combustion science and technology **55**, 41-61 (1987).

7. A. Ferrario, M. Garbi, C. E. D. S. G. L. T. G. A. Malvicini, and C. Giuliano, "Real-time CARS spectroscopy in a semi- industrial furnace," in *Conference on Lasers and Electro-Optics*(Optical Society of America, Baltimore, Maryland, 1983), p. WD2.

8. N. Lallemant, F. Breussin, R. Weber, T. Ekman, J. Dugue, J. M. Samaniego, O. Charon, A. J. Van den Hoogen, J. Van der Bemt, W. Fujisaki, T. Imanari, T. Nakamura, and K. Iino, "Flame structure, heat transfer and pollutant emissions characteristics of oxy-natural gas flames in the 0.7-1 MW thermal input range," J. Inst. Energy **73**, 169-182 (2000).

9. R. D. Hancock, K. E. Bertagnolli, and R. P. Lucht, "Nitrogen and hydrogen CARS temperature measurements in a hydrogen/air flame using a near-adiabatic flat-flame burner," Combustion and Flame **109**, 323-331 (1997).

10. W. Kreutner, W. Stricker, and T. Just, "Comparison of Spontaneous Raman and CARS Measurements in a Laminar Flame at Atmospheric Pressure," Appl. Spectrosc. **41**, 98-106 (1987).

11. W. M. Tolles, and R. D. Turner, "A Comparative Analysis of the Analytical Capabilities of Coherent Anti-Stokes Raman Spectroscopy (CARS) Relative to Raman Scattering and Absorption Spectroscopy," Appl. Spectrosc. **31**, 96-103 (1977).

12. A. Lawitzki, I. Plath, W. Stricker, J. Bittner, U. Meier, and K. Kohse-Höinghaus, "Laser-induced fluorescence determination of flame temperatures in comparison with CARS measurements," Applied Physics B **50**, 513-518 (1990).

13. A. C. Eckbreth, and T. J. Anderson, "Dual broadband CARS for simultaneous, multiple species measurements," Appl Optics **24**, 2731-2736 (1985).

14. R. P. Lucht, "Three-laser coherent anti-Stokes Raman scattering measurements of two species," Opt Lett **12**, 78-80 (1987).

15. S. Roy, T. R. Meyer, M. S. Brown, V. N. Velur, R. P. Lucht, and J. R. Gord, "Triple-pump coherent anti-Stokes Raman scattering (CARS): temperature and multiple-species concentration measurements in reacting flows," Opt Commun **224**, 131-137 (2003).

16. C. C. Hayden, and D. W. Chandler, "Femtosecond time-resolved studies of coherent vibrational Raman scattering in large gas-phase molecules," The Journal of Chemical Physics **103**, 10465-10472 (1995).

17. S. Meyer, M. Schmitt, A. Materny, W. Kiefer, and V. Engel, "A theoretical analysis of the time-resolved femtosecond CARS spectrum of I2," Chem Phys Lett **281**, 332-336 (1997).

18. A. Materny, T. Chen, M. Schmitt, T. Siebert, A. Vierheilig, V. Engel, and W. Kiefer, "Wave packet dynamics in different electronic states investigated by femtosecond time-resolved four-wave-mixing spectroscopy," Applied Physics B **71**, 299-317 (2000).

19. H.-M. Frey, P. Beaud, T. Gerber, B. Mischler, P. P. Radi, and A. P. Tzannis, "Femtosecond nonresonant degenerate four-wave mixing at atmospheric pressure and in a free jet," Applied Physics B **68**, 735-739 (1999).

20. T. Lang, K.-L. Kompa, and M. Motzkus, "Femtosecond CARS on H 2," Chem Phys Lett **310**, 65-72 (1999).

21. T. Lang, M. Motzkus, H. M. Frey, and P. Beaud, "High resolution femtosecond coherent anti-Stokes Raman scattering: Determination of rotational constants, molecular anharmonicity, collisional line shifts, and temperature," The Journal of Chemical Physics **115**, 5418-5426 (2001).

22. P. Beaud, H. M. Frey, T. Lang, and M. Motzkus, "Flame thermometry by femtosecond CARS," Chem Phys Lett **344**, 407-412 (2001).

23. R. P. Lucht, S. Roy, T. R. Meyer, and J. R. Gord, "Femtosecond coherent anti-Stokes Raman scattering measurement of gas temperatures from frequency-spread dephasing of the Raman coherence," Appl Phys Lett **89** (2006).

24. S. Roy, P. J. Kinnius, R. P. Lucht, and J. R. Gord, "Temperature measurements in reacting flows by time-resolved femtosecond coherent anti-Stokes Raman scattering (fs-CARS) spectroscopy," Opt Commun **281**, 319-325 (2008).

25. T. Lang, and M. Motzkus, "Single-shot femtosecond coherent anti-Stokes Raman-scattering thermometry," JOSA B **19**, 340-344 (2002).

26. A. Bohlin, B. D. Patterson, and C. J. Kliewer, "Communication: Simplified two-beam rotational CARS signal generation demonstrated in 1D," The Journal of Chemical Physics **138**, 081102 (2013).

27. A. Bohlin, and C. J. Kliewer, "Communication: Two-dimensional gas-phase coherent anti-Stokes Raman spectroscopy (2D-CARS): Simultaneous planar imaging and multiplex spectroscopy in a single laser shot," The Journal of Chemical Physics **138**, 221101 (2013).

28. A. Hosseinnia, M. Ruchkina, P. Ding, P.-E. Bengtsson, and J. Bood, "Simultaneous temporally and spectrally resolved Raman coherences with single-shot fs/ns rotational CARS," Opt Lett **45**, 308-311 (2020).

29. A. M. Weiner, "Femtosecond pulse shaping using spatial light modulators," Review of Scientific Instruments **71**, 1929-1960 (2000).

30. J. D. Miller, M. N. Slipchenko, T. R. Meyer, H. U. Stauffer, and J. R. Gord, "Hybrid femtosecond/picosecond coherent anti-Stokes Raman scattering for high-speed gas-phase thermometry," Opt Lett **35**, 2430-2432 (2010).

31. J. D. Miller, M. N. Slipchenko, and T. R. Meyer, "Probe-pulse optimization for nonresonant suppression in hybrid fs/ps coherent anti-Stokes Raman scattering at high temperature," Opt Express **19**, 13326-13333 (2011).

32. H. U. Stauffer, J. D. Miller, S. Roy, J. R. Gord, and T. R. Meyer, "Communication: Hybrid femtosecond/picosecond rotational coherent anti-Stokes Raman scattering thermometry using a narrowband time-asymmetric probe pulse," The Journal of Chemical Physics **136**, 111101 (2012).

33. M. Scherman, M. Nafa, T. Schmid, A. Godard, A. Bresson, B. Attal-Tretout, and P. Joubert, "Rovibrational hybrid fs/ps CARS using a volume Bragg grating for N2 thermometry," Opt Lett **41**, 488-491 (2016).

34. S. P. Kearney, and D. J. Scoglietti, "Hybrid femtosecond/picosecond rotational coherent anti-Stokes Raman scattering at flame temperatures using a second-harmonic bandwidth-compressed probe," Opt Lett **38**, 833-835 (2013).

35. J. D. Miller, C. E. Dedic, S. Roy, J. R. Gord, and T. R. Meyer, "Interference-free gas-phase thermometry at elevated pressure using hybrid femtosecond/picosecond rotational coherent anti-Stokes Raman scattering," Opt Express **20**, 5003-5010 (2012).

36. C. E. Dedic, J. D. Miller, and T. R. Meyer, "Dual-pump vibrational/rotational femtosecond/picosecond coherent anti-Stokes Raman scattering temperature and species measurements," Opt Lett **39**, 6608-6611 (2014).

37. T. Lang, and M. Motzkus, "Single-shot femtosecond coherent anti-Stokes Raman-scattering thermometry," J Opt Soc Am B **19**, 340-344 (2002).

38. S. Roy, W. D. Kulatilaka, D. R. Richardson, R. P. Lucht, and J. R. Gord, "Gas-phase single-shot thermometry at 1 kHz using fs-CARS spectroscopy," Opt Lett **34**, 3857-3859 (2009).

39. D. R. Richardson, R. P. Lucht, S. Roy, W. D. Kulatilaka, and J. R. Gord, "Single-laser-shot femtosecond coherent anti-Stokes Raman scattering thermometry at 1000 Hz in unsteady flames," P Combust Inst **33**, 839-845 (2011).

40. D. R. Richardson, R. P. Lucht, W. D. Kulatilaka, S. Roy, and J. R. Gord, "Chirped-probe-pulse femtosecond coherent anti-Stokes Raman scattering concentration measurements," Journal of the Optical Society of America B **30**, 188-196 (2013).

41. D. R. Richardson, R. P. Lucht, W. D. Kulatilaka, S. Roy, and J. R. Gord, "Theoretical modeling of single-laser-shot, chirped-probe-pulse femtosecond coherent anti-Stokes Raman scattering thermometry," Appl Phys B-Lasers O **104**, 699-714 (2011).

42. L. M. Thomas, A. Satija, and R. P. Lucht, "Technique developments and performance analysis of chirped-probe-pulse femtosecond coherent anti-Stokes Raman scattering combustion thermometry," Appl Optics **56**, 8797-8810 (2017).

43. M. Gu, A. Satija, and R. P. Lucht, "Impact of moderate pump–Stokes chirp on femtosecond coherent anti-Stokes Raman scattering spectra," J Raman Spectrosc **51**, 115-124 (2020).

44. D. R. Richardson, D. Bangar, and R. P. Lucht, "Polarization suppression of the nonresonant background in femtosecond coherent anti-Stokes Raman scattering for flame thermometry at 5 kHz," Opt Express **20**, 21495-21504 (2012).

45. S. R. Engel, J. D. Miller, C. E. Dedic, T. Seeger, A. Leipertz, and T. R. Meyer, "Hybrid femtosecond/picosecond coherent anti-Stokes Raman scattering for high-speed CH4/N2 measurements in binary gas mixtures," J Raman Spectrosc **44**, 1336-1343 (2013).

46. S. P. Kearney, and P. M. Danehy, "Pressure measurements using hybrid femtosecond/picosecond rotational coherent anti-Stokes Raman scattering," Opt Lett **40**, 4082-4085 (2015).

47. C. D. Slabaugh, C. N. Dennis, I. Boxx, W. Meier, and R. R. Lucht, "5 kHz thermometry in a swirl-stabilized gas turbine model combustor using chirped probe pulse femtosecond CARS. Part 2. Analysis of swirl flame dynamics," Combustion and Flame **173**, 454-467 (2016).

48. C. N. Dennis, C. D. Slabaugh, I. G. Boxx, W. Meier, and R. P. Lucht, "5 kHz thermometry in a swirl-stabilized gas turbine model combustor using chirped probe pulse femtosecond CARS. Part 1: Temporally resolved swirl-flame thermometry," Combustion and Flame **173**, 441-453 (2016).

49. L. M. Thomas, A. Lowe, A. Satija, A. R. Masri, and R. P. Lucht, "Five kHz thermometry in turbulent spray flames using chirped-probe pulse femtosecond CARS, part I: Processing and interference analysis," Combustion and Flame **200**, 405-416 (2019).

50. A. Lowe, L. M. Thomas, A. Satija, R. P. Lucht, and A. R. Masri, "Five kHz thermometry in turbulent spray flames using chirped-probe-pulse femtosecond CARS, part II: Structure of reaction zones," Combustion and Flame **200**, 417-432 (2019).

51. S. P. Kearney, and D. R. Guildenbecher, "Temperature measurements in metalized propellant combustion using hybrid fs/ps coherent anti-Stokes Raman scattering," Appl Optics **55**, 4958-4966 (2016).

52. S. P. Kearney, "Hybrid fs/ps rotational CARS temperature and oxygen measurements in the product gases of canonical flat flames," Combustion and Flame **162**, 1748-1758 (2015).

53. C. E. Dedic, T. R. Meyer, and J. B. Michael, "Single-shot ultrafast coherent anti-Stokes Raman scattering of vibrational/rotational nonequilibrium," Optica **4**, 563-570 (2017).

54. D. R. Richardson, H. U. Stauffer, S. Roy, and J. R. Gord, "Comparison of chirped-probe-pulse and hybrid femtosecond/picosecond coherent anti-Stokes Raman scattering for combustion thermometry," Appl Optics **56**, E37-E49 (2017).

55. S. P. Kearney, D. J. Scoglietti, and C. J. Kliewer, "Hybrid femtosecond/picosecond rotational coherent anti-Stokes Raman scattering temperature and concentration measurements using two different picosecond-duration probes," Opt Express **21**, 12327-12339 (2013).

56. M. L. Koszykowski, R. L. Farrow, and R. E. Palmer, "Calculation of Collisionally Narrowed Coherent Anti-Stokes Raman-Spectroscopy Spectra," Opt Lett **10**, 478-480 (1985).

57. L. A. Rahn, R. E. Palmer, M. L. Koszykowski, and D. A. Greenhalgh, "Comparison of Rotationally Inelastic-Collision Models for Q-Branch Raman-Spectra of N-2," Chem Phys Lett **133**, 513-516 (1987).

58. M. L. Koszykowski, L. A. Rahn, R. E. Palmer, and M. E. Coltrin, "Theoretical and Experimental Studies of High-Resolution Inverse Raman-Spectra of N-2 at 1-10-Atm," J Phys Chem-Us **91**, 41-46 (1987).

59. T. Bouché, T. Dreier, B. Lange, J. Wolfrum, E. U. Franck, and W. Schilling, "Collisional narrowing and spectral shift in coherent anti-stokes Raman spectra of molecular nitrogen up to 2500 bar and 700 K," Applied Physics B **50**, 527-533 (1990).

60. A. E. DePristo, S. D. Augustin, R. Ramaswamy, and H. Rabitz, "Quantum number and energy scaling for nonreactive collisions," The Journal of Chemical Physics **71**, 850-865 (1979).

61. L. Bonamy, J. Bonamy, D. Robert, B. Lavorel, R. Saintloup, R. Chaux, J. Santos, and H. Berger, "Rotationally Inelastic Rates for N2-N2 System from a Scaling Theoretical-Analysis of the Stimulated Raman-Q Branch," J Chem Phys **89**, 5568-5577 (1988).

62. B. Lavorel, G. Millot, R. Saint-Loup, C. Wenger, H. Berger, J. Sala, J. Bonamy, and D. Robert, "Rotational collisional line broadening at high temperatures in the N2 fundamental Q-branch studied with stimulated Raman spectroscopy," Journal de Physique **47**, 417-425 (1986).

63. G. Knopp, P. Beaud, P. Radi, M. Tulej, B. Bougie, D. Cannavo, and T. Gerber, "Pressure-dependent N2 Q-branch fs-CARS measurements," J Raman Spectrosc **33**, 861-865 (2002).

64. G. Knopp, P. Radi, M. Tulej, T. Gerber, and P. Beaud, "Collision induced rotational energy transfer probed by time-resolved coherent anti-Stokes Raman scattering," The Journal of Chemical Physics **118**, 8223-8233 (2003).

65. T. Dreier, G. Schiff, and A. A. Suvernev, "Collisional Effects in Q-Branch Coherent Anti-Stokes-Raman Spectra of N-2 and O-2 at High-Pressure and High-Temperature," J Chem Phys **100**, 6275-6289 (1994).

66. F. Vestin, M. Afzelius, H. Berger, F. Chaussard, R. Saint-Loup, and P. E. Bengtsson, "Rotational CARS thermometry at high temperature (1800 K) and high pressure (0.1–1.55 MPa)," J Raman Spectrosc **38**, 963-968 (2007).

67. M. Ridder, A. A. Suvernev, and T. Dreier, "Collision effects in nitrogen and methane coherent anti-Stokes Raman isotropic Q-branch spectra at high densities," The Journal of Chemical Physics **105**, 3376-3386 (1996).

68. P. Joubert, J. Bonamy, L. Gomez, and D. Bermejo, "N2□H2 isotropic Raman Q-branch linewidths: an Energy-Corrected Sudden scaling law," J Raman Spectrosc **39**, 707-710 (2008).

69. H. Skenderovi, T. Buckup, W. Wohlleben, and M. Motzkus, "Determination of collisional line broadening coefficients with femtosecond time-resolved CARS," J Raman Spectrosc **33**, 866-871 (2002).

70. J. Hussong, R. Lückerath, W. Stricker, X. Bruet, P. Joubert, J. Bonamy, and D. Robert, "Hydrogen CARS thermometry in a high-pressure H2–air flame. Test of H2 temperature accuracy and influence of line width by comparison with N2 CARS as reference," Applied Physics B **73**, 165-172 (2001).

71. J. Bonamy, L. Bonamy, D. Robert, M. L. Gonze, G. Millot, B. Lavorel, and H. Berger, "Rotational relaxation of nitrogen in ternary mixtures N2–CO2–H2O: Consequences in coherent anti-Stokes Raman spectroscopy thermometry," The Journal of Chemical Physics **94**, 6584-6589 (1991).

72. J. Buldyreva, J. Bonamy, M. C. Weikl, F. Beyrau, T. Seeger, A. Leipertz, F. Vestin, M. Afzelius, J. Bood, and P.-E. Bengtsson, "Linewidth modelling of C2H2□N2 mixtures tested by rotational CARS measurements," J Raman Spectrosc **37**, 647-654 (2006).

73. P. S. Hsu, H. U. Stauffer, N. Jiang, J. R. Gord, and S. Roy, "Direct measurements of collisional Raman line broadening in the S-branch transitions of CO perturbed by CO, N2, and CO2," Appl Optics **58**, C1-C6 (2019).

74. N. Jiang, S. Roy, P. S. Hsu, and J. R. Gord, "Direct measurement of CO2S-branch Raman linewidths broadened by O2, Ar, and C2H4," Appl Optics **58**, C55-C60 (2019).

75. E. T. Nibbering, D. A. Wiersma, and K. Duppen, "Ultrafast nonlinear spectroscopy with chirped optical pulses," Phys Rev Lett **68**, 514 (1992).

76. K. P. Knutsen, J. C. Johnson, A. E. Miller, P. B. Petersen, and R. J. Saykally, "High spectral resolution multiplex CARS spectroscopy using chirped pulses," Chem Phys Lett **387**, 436-441 (2004).

77. R. M. Onorato, N. Muraki, K. P. Knutsen, and R. J. Saykally, "Chirped coherent anti-Stokes Raman scattering as a high-spectral-and spatial-resolution microscopy," Opt Lett **32**, 2858-2860 (2007).

78. I. Rocha-Mendoza, W. Langbein, and P. Borri, "Coherent anti-Stokes Raman microspectroscopy using spectral focusing with glass dispersion," Appl Phys Lett **93** (2008).

79. S. P. Kearney, "Bandwidth optimization of femtosecond pure-rotational coherent anti-Stokes Raman scattering by pump/Stokes spectral focusing," Appl Optics **53**, 6579-6585 (2014).

80. K. P. Knutsen, B. M. Messer, R. M. Onorato, and R. J. Saykally, "Chirped coherent anti-Stokes Raman scattering for high spectral resolution spectroscopy and chemically selective imaging," J Phys Chem B **110**, 5854-5864 (2006).

81. D. Oron, N. Dudovich, D. Yelin, and Y. Silberberg, "Quantum control of coherent anti-Stokes Raman processes," Physical Review A **65** (2002).

82. J. Su, R. X. Xie, C. K. Johnson, and R. Q. Hui, "Single-fiber-laser-based wavelength tunable excitation for coherent Raman spectroscopy," J Opt Soc Am B **30**, 1671-1682 (2013).

83. P. J. Wrzesinski, S. Roy, and J. R. Gord, "Interference-free coherence dynamics of gas-phase molecules using spectral focusing," Opt Express **20**, 23390-23397 (2012).

84. M. Marrocco, "Simple model of coherent anti-Stokes Raman scattering signals generated by means of linearly chirped ultrashort Gaussian laser pulses," J Raman Spectrosc **49**, 1109-1115 (2018).

85. R. W. Hellwarth, D. M. Pennington, and M. A. Henesian, "Indices governing optical self-focusing and self-induced changes in the state of polarization in N2, O2, H2, and Ar gases," Physical Review A **41**, 2766-2777 (1990).

86. V. Loriot, E. Hertz, O. Faucher, and B. Lavorel, "Measurement of high order Kerr refractive index of major air components," Opt Express **17**, 13429-13434 (2009).

87. E. W. Rosenthal, J. P. Palastro, N. Jhajj, S. Zahedpour, J. K. Wahlstrand, and H. M. Milchberg, "Sensitivity of propagation and energy deposition in femtosecond filamentation to the nonlinear refractive index," Journal of Physics B: Atomic, Molecular and Optical Physics **48**, 094011 (2015).

88. E. T. J. Nibbering, G. Grillon, M. A. Franco, B. S. Prade, and A. Mysyrowicz, "Determination of the inertial contribution to the nonlinear refractive index of air, N2, and O2 by use of unfocused high-intensity femtosecond laser pulses," Journal of the Optical Society of America B **14**, 650-660 (1997).

89. D. Langevin, J. M. Brown, M. B. Gaarde, and A. Couairon, "Determination of molecular contributions to the nonlinear refractive index of air for mid-infrared femtosecond laser-pulse excitation," Physical Review A **99**, 063418 (2019).

90. J. K. Wahlstrand, Y. H. Cheng, and H. M. Milchberg, "Absolute measurement of the transient optical nonlinearity in N2, O2, N2O, and Ar," Physical Review A **85**, 043820 (2012).

91. P. Sprangle, J. R. Peñano, and B. Hafizi, "Propagation of intense short laser pulses in the atmosphere," Physical Review E **66**, 046418 (2002).

92. M. J. Shaw, C. J. Hooker, and D. C. Wilson, "Measurement of the nonlinear refractive index of air and other gases at 248 nm," Opt Commun **103**, 153-160 (1993).

93. D. K. Veirs, and G. M. Rosenblatt, "Raman line positions in molecular hydrogen: H2, HD, HT, D2, DT, and T2," J Mol Spectrosc **121**, 401-419 (1987).

94. R. J. Hall, and J. H. Stufflebeam, "Quantitative CARS spectroscopy of CO2 and N2O," Appl Optics **23**, 4319-4327 (1984).

95. I. Suzuki, "General anharmonic force constants of carbon dioxide," J Mol Spectrosc **25**, 479-500 (1968).

96. L. S. Rothman, R. L. Hawkins, R. B. Wattson, and R. R. Gamache, "Energy levels, intensities, and linewidths of atmospheric carbon dioxide bands," Journal of Quantitative Spectroscopy and Radiative Transfer **48**, 537-566 (1992).

97. B. Lavorel, G. Millot, R. Saint-Loup, H. Berger, L. Bonamy, J. Bonamy, and D. Robert, "Study of collisional effects on band shapes of the ν1/2ν2 Fermi dyad in CO2 gas with stimulated Raman spectroscopy. I. Rotational and vibrational relaxation in the 2ν2 band," The Journal of Chemical Physics **93**, 2176-2184 (1990).

98. R. G. Gordon, "On the Rotational Diffusion of Molecules," The Journal of Chemical Physics **44**, 1830-1836 (1966).

99. R. Lemus, M. Sánchez-Castellanos, F. Pérez-Bernal, J. M. Fernández, and M. Carvajal, "Simulation of the Raman spectra of CO2: Bridging the gap between algebraic models and experimental spectra," The Journal of Chemical Physics **141**, 054306 (2014).

100. C. M. Penney, L. M. Goldman, and M. Lapp, "Raman Scattering Cross Sections," Nature Physical Science **235**, 110 (1972).

101. G. Tejeda, B. Maté, and S. Montero, "Overtone Raman spectrum and molecular polarizability surface of CO2," The Journal of Chemical Physics **103**, 568-576 (1995).

102. M. Sánchez-Castellanos, R. Lemus, M. Carvajal, F. Pérez-Bernal, and J. M. Fernández, "A study of the Raman spectrum of CO2 using an algebraic approach," Chem Phys Lett **554**, 208-213 (2012).

103. G. Maroulis, "Electric (hyper)polarizability derivatives for the symmetric stretching of carbon dioxide," Chem Phys **291**, 81-95 (2003).

104. J. M. Fernández, A. Punge, G. Tejeda, and S. Montero, "Quantitative diagnostics of a methane/air mini-flame by Raman spectroscopy," J Raman Spectrosc **37**, 175-182 (2006).

105. S. Roy, T. R. Meyer, R. P. Lucht, V. M. Belovich, E. Corporan, and J. R. Gord, "Temperature and CO2 concentration measurements in the exhaust stream of a liquid-fueled combustor using dual-pump coherent anti-Stokes Raman scattering (CARS) spectroscopy," Combustion and Flame **138**, 273-284 (2004).

106. T. R. Meyer, S. Roy, R. P. Lucht, and J. R. Gord, "Dual-pump dual-broadband CARS for exhaust-gas temperature and CO2–O2–N2 mole-fraction measurements in model gas-turbine combustors," Combustion and Flame **142**, 52-61 (2005).

107. S. Roy, P. J. Wrzesinski, D. Pestov, M. Dantus, and J. R. Gord, "Single-beam coherent anti-Stokes Raman scattering (CARS) spectroscopy of gas-phase CO2 via phase and polarization shaping of a broadband continuum," J Raman Spectrosc **41**, 1194-1199 (2010).

108. M. Kerstan, I. Makos, S. Nolte, A. Tünnermann, and R. Ackermann, "Two-beam femtosecond coherent anti-Stokes Raman scattering for thermometry on CO2," Appl Phys Lett **110**, 021116 (2017).

109. W. D. Kulatilaka, J. R. Gord, and S. Roy, "Effects of O2–CO2 polarization beating on femtosecond coherent anti-Stokes Raman scattering (fs-CARS) spectroscopy of O2," Applied Physics B **102**, 141-147 (2011).

110. T. Seeger, J. Kiefer, Y. Gao, B. D. Patterson, C. J. Kliewer, and T. B. Settersten, "Suppression of Raman-resonant interferences in rotational coherent anti-Stokes Raman spectroscopy using time-delayed picosecond probe pulses," Opt Lett **35**, 2040-2042 (2010).

111. M. Bitter, and V. Milner, "Coherent anti-Stokes Raman spectroscopy in the presence of strong resonant signal from background molecules," Opt Lett **38**, 2050-2052 (2013).

112. P. J. Wrzesinski, H. U. Stauffer, W. D. Kulatilaka, J. R. Gord, and S. Roy, "Time-resolved femtosecond CARS from 10 to 50 Bar: collisional sensitivity," J Raman Spectrosc **44**, 1344-1348 (2013).

113. T. L. Courtney, N. T. Mecker, B. D. Patterson, M. Linne, and C. J. Kliewer, "Hybrid femtosecond/picosecond pure rotational anti-Stokes Raman spectroscopy of nitrogen at high pressures (1–70 atm) and temperatures (300–1000 K)," Appl Phys Lett **114**, 101107 (2019).

114. N. Torge Mecker, T. L. Courtney, B. D. Patterson, D. Escofet-Martin, B. Peterson, C. J. Kliewer, and M. Linne, "Optimizing hybrid rotational femtosecond/picosecond coherent anti-

Stokes Raman spectroscopy in nitrogen at high pressures and temperatures," Journal of the Optical Society of America B **37**, 1035-1046 (2020).

115. H. U. Stauffer, K. A. Rahman, M. N. Slipchenko, S. Roy, J. R. Gord, and T. R. Meyer, "Interference-free hybrid fs/ps vibrational CARS thermometry in high-pressure flames," Opt Lett **43**, 4911-4914 (2018).

116. F. Grisch, P. Bouchardy, and W. Clauss, "CARS thermometry in high pressure rocket combustors," Aerospace Science and Technology **7**, 317-330 (2003).

117. E. Jourdanneau, T. Gabard, F. Chaussard, R. Saint-Loup, H. Berger, E. Bertseva, and F. Grisch, "CARS methane spectra: Experiments and simulations for temperature diagnostic purposes," J Mol Spectrosc **246**, 167-179 (2007).

118. K. A. Vereschagin, V. V. Smirnov, O. M. Stel'makh, V. I. Fabelinsky, W. Clauss, and M. Oschwald, "Single-shot CARS thermometry of high-pressure hydrocarbon flames using simultaneous intensity and linewidth measurements," J Raman Spectrosc **41**, 902-906 (2010).

119. K. A. Vereshchagin, V. V. Smirnov, O. M. Stel'makh, and V. I. Fabelinskii, "CARS diagnostics of the burning of H2— O2and CH4— O2mixtures at high temperatures and pressures," Quantum Electronics **42**, 44-50 (2012).

120. A. C. Eckbreth, *Laser diagnostics for combustion temperature and species* (Abacus Press, 1988).

121. W. M. Tolles, J. W. Nibler, J. R. McDonald, and A. B. Harvey, "A Review of the Theory and Application of Coherent Anti-Stokes Raman Spectroscopy (CARS)," Appl. Spectrosc. **31**, 253-271 (1977).

122. S. Roy, J. R. Gord, and A. K. Patnaik, "Recent advances in coherent anti-Stokes Raman scattering spectroscopy: Fundamental developments and applications in reacting flows," Progress in Energy and Combustion Science **36**, 280-306 (2010).

123. G. Herzberg, *Molecular spectra and molecular structure* (R.E. Krieger Pub. Co., 1989).

124. C. M. Penney, R. L. St. Peters, and M. Lapp, "Absolute rotational Raman cross sections for N2, O2, and CO2," J. Opt. Soc. Am. **64**, 712-716 (1974).

125. R. H. Tipping, and J. P. Bouanich, "On the use of Herman–Wallis factors for diatomic molecules," Journal of Quantitative Spectroscopy and Radiative Transfer **71**, 99-103 (2001).

126. M. Marrocco, "Herman–Wallis correction in vibrational CARS of oxygen," J Raman Spectrosc **42**, 1836-1842 (2011).

127. R. P. Lucht, P. J. Kinnius, S. Roy, and J. R. Gord, "Theory of femtosecond coherent anti-Stokes Raman scattering spectroscopy of gas-phase transitions," J Chem Phys **127** (2007).

128. L. Babel, H. Kellerer, and V. Kotov, "Thek-partitioning problem," Mathematical Methods of Operations Research **47**, 59-82 (1998).

129. A. M. Weiner, "Ultrafast optical pulse shaping: A tutorial review," Opt Commun **284**, 3669-3692 (2011).

130. B. Xu, J. M. Gunn, J. M. D. Cruz, V. V. Lozovoy, and M. Dantus, "Quantitative investigation of the multiphoton intrapulse interference phase scan method for simultaneous phase measurement and compensation of femtosecond laser pulses," Journal of the Optical Society of America B **23**, 750-759 (2006).

131. C. N. Dennis, C. D. Slabaugh, I. G. Boxx, W. G. Meier, and R. P. Lucht, "Chirped probe pulse femtosecond coherent anti-Stokes Raman scattering thermometry at 5 kHz in a Gas Turbine Model Combustor," P Combust Inst **35**, 3731-3738 (2015).

132. A. V. Sepman, V. V. Toro, A. V. Mokhov, and H. B. Levinsky, "Determination of temperature and concentrations of main components in flames by fitting measured Raman spectra," Applied Physics B **112**, 35-47 (2013).

133. J. Liu, and J. Lampinen, "A Fuzzy Adaptive Differential Evolution Algorithm," Soft Computing **9**, 448-462 (2005).

134. D. Oron, N. Dudovich, and Y. Silberberg, "Femtosecond phase-and-polarization control for background-free coherent anti-Stokes Raman spectroscopy," Phys Rev Lett **90** (2003).

135. L. M. Thomas, A. Lowe, A. Satija, A. R. Masri, and R. P. Lucht, "Five kHz thermometry in turbulent spray flames using chirped-probe pulse femtosecond CARS, part I: Processing and interference analysis," Combustion and Flame (2018).

136. Á. Börzsönyi, Z. Heiner, A. P. Kovács, M. P. Kalashnikov, and K. Osvay, "Measurement of pressure dependent nonlinear refractive index of inert gases," Opt Express **18**, 25847-25854 (2010).

137. J. C. Owens, "Optical Refractive Index of Air: Dependence on Pressure, Temperature and Composition," Appl Optics **6**, 51-59 (1967).

138. D. Han, A. Satija, J. Kim, Y. Weng, J. P. Gore, and R. P. Lucht, "Dual-pump vibrational CARS measurements of temperature and species concentrations in turbulent premixed flames with CO2 addition," Combustion and Flame **181**, 239-250 (2017).

139. Y. He, J. Zhu, B. Li, Z. Wang, Z. Li, M. Aldén, and K. Cen, "In-situ Measurement of Sodium and Potassium Release during Oxy-Fuel Combustion of Lignite using Laser-Induced Breakdown Spectroscopy: Effects of O2 and CO2 Concentration," Energy & Fuels **27**, 1123-1130 (2013).

140. T. Le Cong, and P. Dagaut, "Oxidation of H2/CO2 mixtures and effect of hydrogen initial concentration on the combustion of CH4 and CH4/CO2 mixtures: Experiments and modeling," P Combust Inst **32**, 427-435 (2009).

141. V. Ratna Kishore, M. R. Ravi, and A. Ray, "Adiabatic burning velocity and cellular flame characteristics of H2–CO–CO2–air mixtures," Combustion and Flame **158**, 2149-2164 (2011).

142. Y. Ran, M. Junghanns, A. Boden, S. Nolte, A. Tünnermann, and R. Ackermann, "Temperature and gas concentration measurements with vibrational ultra-broadband two-beam femtosecond/picosecond coherent anti-Stokes Raman scattering and spontaneous Raman scattering," J Raman Spectrosc **50**, 1268-1275 (2019).

143. A. Lowe, L. M. Thomas, A. Satija, R. P. Lucht, and A. R. Masri, "Chirped-probe-pulse femtosecond CARS thermometry in turbulent spray flames," P Combust Inst **37**, 1383-1391 (2019).

144. T. C. James, and W. Klemperer, "Line Intensities in the Raman Effect of 1Σ Diatomic Molecules," The Journal of Chemical Physics **31**, 130-134 (1959).

145. M. Marrocco, "Comparative analysis of Herman-Wallis factors for uses in coherent anti-Stokes Raman spectra of light molecules," J Raman Spectrosc **40**, 741-747 (2009).

146. J. C. Luthe, E. J. Beiting, and F. Y. Yueh, "Algorithms for calculating coherent anti-stokes Raman spectra: Application to several small molecules," Computer Physics Communications **42**, 73-92 (1986).

147. J. E. Retter, D. R. Richardson, and S. P. Kearney, "Rotational hydrogen thermometry by hybrid fs/ps coherent anti-Stokes Raman scattering in the plume of a burning metalized propellant," Applied Physics B: Lasers and Optics **126**, 83 (2020).

148. L. A. Rahn, R. L. Farrow, and G. J. Rosasco, "Measurement of the self-broadening of the ${\mathrm{H}}_{2}$ Q(0--5) Raman transitions from 295 to 1000 K," Physical Review A **43**, 6075-6088 (1991).

149. B. Lavorel, G. Millot, R. Saint-Loup, H. Berger, L. Bonamy, J. Bonamy, and D. Robert, "Study of collisional effects on band shapes of the ν1/2ν2 Fermi dyad in CO2 gas with stimulated Raman spectroscopy. II. Simultaneous line mixing and Dicke narrowing in the ν1 band," The Journal of Chemical Physics **93**, 2185-2191 (1990).

150. G. Millot, R. Saint-Loup, J. Santos, R. Chaux, H. Berger, and J. Bonamy, "Collisional effects in the stimulated Raman Q branch of O2 and O2–N2," The Journal of Chemical Physics **96**, 961-971 (1992).

151. T. Dreier, G. Schiff, and A. A. Suvernev, "Collisional effects in Q branch coherent anti-Stokes Raman spectra of N2 and O2 at high pressure and high temperature," The Journal of Chemical Physics **100**, 6275-6289 (1994).

VITA

MINGMING GU

EDUCATION

Purdue University, West Lafayette, IN

Ph.D., Mechanical Engineering, Dec. 2020 (expected)

Dissertation: "Development of Ultrafast Coherent Anti-Stokes Raman Scattering (CARS) Spectroscopy for High Pressure Systems"

Chair: Robert P. Lucht, Professor of Mechanical Engineering

Zhejiang University, Hangzhou, China

BS, New Energy Science and Engineering, June 2015

Thesis: "Simulation of CH_4 micro scale combustion in a Swiss roll combustor"

Chair: Weijuan Yang, Professor of Energy Engineering

CURRENT PUBLICATIONS

- **Mingming Gu**, Aman Satija, and Robert P. Lucht, "CO_2 Chirped-Probe-Pulse femtosecond CARS for thermometry measurement", Proceeding of the Combustion Institute, Vol. 37 (in press)
- Ryan J. Tanchin, Ziqiao Chang, **Mingming Gu**, Vishnu Radhakrishna, R. P. Lucht, C. S. Goldenstein, "Ultrafast-laser-absorption spectroscopy for single-shot, mid-infrared measurements of temperature, CO, and CH_4 in flames", Optics Letters, Vol. 45 (2), 583-586 (2020)
- **Mingming Gu**, Aman Satija, and Robert P. Lucht, "Effects of self-phase modulation (SPM) on femtosecond coherent anti-Stokes Raman scattering spectroscopy", Optics Express, Vol. 27 (23), 33954-33966 (2019)
- **Mingming Gu**, Aman Satija, and Robert P. Lucht, "Impact of moderate pump-Stokes chirp on femtosecond coherent anti-Stokes Raman scattering spectra", Journal of Raman Spectroscopy, Vol. 51 (1), 115-124 (2019)

CONFERENCES AND PRESENTATIONS

- "Development of chirped-probe-pulse femtosecond CARS technique for CO_2", AIAA SciTech 2020 Forum

- "Investigation of the chirped-probe-pulse femtosecond coherent anti-Stokes Raman scattering at high pressure", AIAA SciTech 2019 Forum
- "Implication of self-phase modulation (SPM) for N_2 femtosecond coherent anti-Stokes Raman scattering spectroscopy at elevated pressure", 74th International Symposium on Molecular Spectroscopy, 2019
- "Effects of moderate pump and Stokes chirp on chirped-probe pulse femtosecond coherent anti-Stokes Raman scattering thermometry", AIAA SciTech 2018 Forum

RESEARCH EXPERIENCE

Purdue University West Lafayette, IN

Graduate Research Assistant with Dr. Robert P. Lucht 2016-2020

- Conducted femtosecond (fs) CARS measurements in a high pressure high temperature gas cell. Gained 2k hours of hands on experiences on laser operation and optical alignment.
- Reduced the computational time for CARS density matrix calculation by a magnitude through using parallel programming and computation.
- Developed theoretical models that explained the frequency chirp and self-phase modulation effects in high pressure fs CARS measurement.
- Developed a phenomenological model for carbon dioxide fs CARS, proposed and validated its application for temperature and concentration measurement.
- Helped in performing fs absorption measurements for combustion gases. Responsible for designing the optical system and charactering the ultrafast pulse propagation in fiber optics.

TEACHING EXPERIENCE

Purdue University West Lafayette, IN

Teaching Assistant 2017-2020

Courses: Thermodynamics, Statistical Thermodynamics

- Offered regular tutoring sections (10 hours weekly) to graduate and undergraduate students.
- Designed and offered EES software workshops.
- Graded homework and exams and helped develop exam problems.

PROFESSIONAL MEMBERSHIPS

Member of the Combustion Institute

Member of the American Institute of Aeronautics and Astronautics

Member of the Optical Society of America

SKILLS

- Equipment: Laser amplifier (Legend, Coherent), Oscillator (Mantis, Coherent), OPA (Light Conversion), SHBC (Light Conversion), Pulse shaper (femtoJock, Biophotonics), Most grating based spectrometers.
- Programming: Proficient at Python, Fortran, EES; Familiar with Matlab, Octave; Have experience with OpenMP, mpi4py.
- Software: Familiar with Cantera, Chemkin, SolidWorks, AutoCAD.